2022-12-23

Analysis and Design of a mm-Wave Wideband LTCC Patch Antenna for 5G Application

Sadeghi, Maryam

UNIVERSITY OF CALGARY

Analysis and Design of a mm-Wave Wideband LTCC Patch Antenna for 5G Applications

by

Maryam Sadeghi

A THESIS

SUBMITTED TO THE FACULTY OF GRADUATE STUDIES

IN PARTIAL FULFILMENT OF THE REQUIREMENTS FOR THE

DEGREE OF MASTER OF SCIENCE

GRADUATE PROGRAM IN ELECTRICAL ENGINEERING

CALGARY, ALBERTA

DECEMBER, 2022

Abstract

Fifth-generation mobile network (5G) has been planned to meet society's strong data accessibility. Since the current Long-Term Evolution (LTE) spectrum, i.e., 4G, is crowded and fragmented under 6 GHz, millimeter-wave frequency bands have attracted more interest in deploying 5G networks. The vast amount of unused spectrum in the mm-wave region can support higher data rates required in future mobile broadband access networks. For such significant data rates, wideband systems are required. An appropriate choice is an aperture-coupled patch antenna offering large bandwidth, good cross-polarization, and higher efficiency than conventional microstrip antennas.

In mm-wave bands, the losses caused by materials, fabrication tolerances, measurement methodologies, and interconnections between feed lines and the antenna impact the overall performance of the antenna. Accordingly, the interest in fabricating mm-wave antennas using Low-Temperature Co-fired Ceramic (LTCC) is increasing. The LTCC fabrication process, in addition to lower substrate loss and higher fabrication tolerance, enjoys flexibility in realizing an arbitrary number of layers and ease of integration with other circuit components.

In this work, a new aperture-coupled patch antenna with wide bandwidth at Ka-band and stable radiation patterns at 28 GHz for 5G applications has been designed, implemented, and tested with Dupont 9K7 LTCC technology.

A parasitic patch, embedded air cavity, and large-size aperture improved the bandwidth. Moreover, the embedded air cavity enhanced the gain and reduced losses caused by the surface wave in the mm-wave band.

A stripline feed was designed and used, allowing the antenna to be more easily integrated with a beamformer IC in the active array configuration. The impedance bandwidth achieved by the designed antenna is 32%, with a maximum gain of 9 dB at 28 GHz.

A broadband Sub-Miniature-Push on Micro (SMPM) coaxial to stripline transition is also developed to feed the proposed antenna. A back-to-back configuration of the transition was fabricated and measured to validate the design. Experimental results showed a good agreement with the simulation results, with a return loss of better than 10 dB and an insertion loss of around 1 dB between 9 to 31 GHz.

Acknowledgements

In starting, all my thanks and praise are given to Allah, whom, by his will, I reached my objectives today

I want to express my gratitude to my supervisor, Prof. Ghannouchi, for his continuous support and guidance and for providing me with this wonderful chance to work at the University of Calgary in the iRadio lab with his outstanding teams. Working under the supervision of such a renowned professor and outstanding mentor has been a true honor.

My gratitude goes to Prof. Mohammad Sharawi, my co-supervisor, for his excellent advice, support, and time. I want to express my appreciation to him for providing me with endless inspiration, generosity, and availability despite his busy schedule and for giving up so much of his valuable time to guide me through my research.

My sincere thanks to Prof. Mohamed Helaoui, a member of my committee and all-time adviser, for his sage advice, recommendations, and remarks throughout the years. I want to thank him, particularly for the valuable System Design Wireless Transceivers course I took with him, which augmented my knowledge about communication systems.

I want to extend my appreciation to the committee member, Prof. Michal Okoniewski, for agreeing to examine and evaluate my thesis work and provide valuable suggestions. I want to express my gratitude to him, in particular, for having taught me so much about many practical points about various antenna types throughout the course I took with him.

With all the members of the iRadio Lab, my time there has been a full-time challenge and a fulfilling experience. I have the most profound admiration for all my colleagues and staff at the University of Calgary, who have worked hard to make my research life fruitful and supportive.

I want to give special thanks to my parents. Words cannot describe my gratitude to my parents, Morteza, and Zahra Sadeghi, for their love, support, and encouragement over the many years I spent studying.

A special thanks to all my family members especially my sister, Fatemeh for supporting me from distant.

Last but not least, I want to express my sincere gratitude to my beloved husband, Dawood Shekari, who spent sleepless nights with me and supported me no matter what with his unending love and care. I sincerely appreciate his dedicated support and guidance throughout the challenging times in my life

Dedicated to

*my dear parents, **Morteza,** and **Zahra***

*my beloved husband, **Dawood***

Table of Contents

Abstract ... ii
Acknowledgements ... iv
List of Tables ... ix
List of Figures and Illustrations ... x
List of Symbols, Abbreviations and Nomenclature ... xiv

CHAPTER ONE: INTRODUCTION ... 1
1.1 Introduction ... 1
1.2 Characteristics of mm-wave communications ... 2
1.2.1 Channel Measurements ... 2
1.2.2 Directivity ... 4
1.2.3 Sensitivity to blockage ... 5
1.3 Phased array antenna ... 5
1.4 LTCC Technology ... 6
1.5 Motivation ... 8
1.6 Objective ... 9
1.7 Dissertation Overview ... 9

CHAPTER TWO: BACKGROUND ... 11
2.1 Introduction ... 11
2.2 Radiation Pattern ... 12
2.3 Directivity ... 12
2.4 Gain ... 13
2.5 Realized Gain ... 13
2.6 Radiation Efficiency ... 14
2.7 Total efficiency ... 15
2.8 Bandwidth ... 15
2.9 Principle of Pattern Multiplication ... 15
2.10 Planar Array ... 16
2.11 Surface Wave ... 17
2.11.1 Surface Wave in Microstrip Patch Antenna ... 19
2.11.2 Surface Waves Effects on Microstrip Patch Antenna ... 20
2.11.3 Suppressing Surface Wave in Microstrip Patch Antenna ... 21
2.12 Conclusion ... 23

CHAPTER THREE: LITERATURE REVIEW ON BROADBAND CAVITY-BACKED LTCC PATCH ANTENNA ... 24
3.1 Introduction ... 24
3.2 Characteristics of Microstrip Patch antenna ... 24
3.2.1 Advantage and Disadvantage Trade-offs ... 26
3.2.2 Analysis and Design ... 27
3.2.2.1 Transmission-Line Model ... 27
3.2.2.2 Multimode Cavity Model ... 28
3.2.3 Design Methodology ... 31
3.2.3.1 Patch Element Design ... 32

3.2.4 Feed/Excitation Methods....34
3.2.4.1 Coaxial Probe Feed....34
3.2.4.2 Coaxial Probe with Capacitive Feed....34
3.2.4.3 Microstrip-Line Feed....35
3.2.4.4 Proximity-Coupled Microstrip Line Feed....36
3.2.4.5 Aperture-Coupled Feed....36
3.2.5 Broadband Techniques in Microstrip Antenna....40
3.2.6 Cavity Backed Patch Antenna....51
3.2.7 LTCC Patch Antennas....55
3.3 Transition in LTCC System....58
3.4 Conclusion....61

CHAPTER FOUR: SMPM COAXIAL CONNECTOR TO LTCC STRIPLINE TRANSITION....62
4.1 Introduction....62
4.2 Design of The Transition....63
4.3 Simulation Results....67
4.4 Conclusions....70

CHAPTER FIVE: DESIGN OF KA BAND PATCH ANTENNA IN LTCC TECHNOLOGY....71
5.1 Introduction....71
5.2 Proposed Antenna Geometry....72
5.2.1 Single Element....72
5.2.2 Single Element antenna with SMPM connector....78
5.3 Conclusion....85

CHAPTER SIX: FABRICATION AND MEASUREMENT RESULTS....86
6.1 Introduction....86
6.2 Assembling of SMPM connectors on the antenna board....86
6.3 Measurement Results....88
6.3.1 SMPM coaxial connector to LTCC stripline transition....88
6.3.2 Wideband LTCC aperture coupled Patch antenna....91
6.3.3 Radiation Pattern for the Proposed single element antenna with and without connector....92
6.4 Comparison between previous works and the proposed single element antenna....95
6.5 Conclusion....96

CHAPTER SEVEN: CONCLUSIONS AND FUTURE WORKS....97
7.1 Research summary....97
7.2 Future Works....98
7.3 Publication....98

REFERENCES....100

List of Tables

Table 1-1: Mm-wave propagation characteristics [4]. 4

Table 4-1: The final optimized dimensions of the proposed coaxial to stripline transition 67

Table 5-1: The final optimized dimensions of the proposed Single antenna................................ 74

Table 5-2: The final optimized dimensions of the proposed Single antenna with an SMPM connector 80

Table 6-1: Radiation Properties of the Proposed Antenna with and without an SMPM Connector. 93

Table 6-2: Comparison between previous works and the proposed wideband LTCC patch antenna 95

List of Figures and Illustrations

Figure 1-1: Rain attenuation at microwave and mm-Wave frequencies [4]. 3

Figure 1-2: Atmospheric and molecular absorption at mm-wave frequencies [4]. 4

Figure 2-1: The distinction between incident power, accepted power (net power), and radiated power 14

Figure 2-2: The geometry of a planar array [17]. 16

Figure 2-3: Full reflection between the boundary of two media with different dielectric constants [19]. 18

Figure 2-4: (a) The sketch of a probe-fed microstrip patch antenna and (b) electromagnetic waves in a microstrip patch antenna of arbitrary shape [19]. 20

Figure 2-5: The annular patch having a central air core [19]. 21

Figure 2-6: The cavity backed microstrip patch antenna [19]. 22

Figure 2-7: The EBG structure used for improving isolation between the patch antennas [19]. 22

Figure 3-1: Configuration of microstrip patch antenna [21] 25

Figure 3-2:Microstrip patch radiation source represented by two equivalent slots [21]. 28

Figure 3-3: Equivalent circuit of a microstrip patch element [21] 28

Figure 3-4: Fundamental-mode electric-field configuration underneath a rectangular patch [21]. 29

Figure 3-5: Fringing fields for fundamental-mode TM10 and higher order mode TM02 [21]. 30

Figure 3-6: Basic E- and H-plane pattern shapes from a rectangular patch [21]. 31

Figure 3-7: Microstrip antenna development procedures [21]. 32

Figure 3-8: Two different capacitive feed methods for relatively thick substrates [21] 35

Figure 3-9: Tear-drop and cylindrical-shaped feed probes for relatively thick substrates [21]. 35

Figure 3-10: Non-contact proximity feed from underneath the patch [21]. 36

Figure 3-11: Patch fed by aperture-coupling slot [116]. 38

Figure 3-12: Bandwidths of rectangular microstrip patches with various substrate thicknesses and two dielectric constants [21]. 41

Figure 3-13: Primary fringing fields of a rectangular patch [21].. 41

Figure 3-14: Geometry of coaxially fed rectangular patch with a U-shaped slot [22] 44

Figure 3-15: Configuration of the proposed antenna. (a) Expanded view. (b) Metal layer details [11] 46

Figure 3-16: (a) U-slot patch with ∏-shaped feed structure. (b) U-slot patch with doubled ∏-shaped feed structure. (c) substrate layout for antennas with single and doubled ∏ feeds (d) U-slot patch dimensions (e) doubled ∏-shaped feed dimensions [33]. 47

Figure 3-17: geometry of multilayered ASP antenna [34].. 48

Figure 3-18: Two substrate layer patch antenna (top view and longitudinal section) [12] 49

Figure 3-19: Two substrate layer patch antenna with improved microstrip transition [12]. 50

Figure 3-20: Layout of the designed antenna. (a) Patch, (b) inverted feeding line. (c) crossed slot, (d) normal feeding line [35]. 51

Figure 3-21: Side view of the designed antenna [35]. 51

Figure 3-22: (a): Top view of a single LTCC stacked patch antenna showing an embedded air cavity. (b): Side view of a single LTCC stacked patch antenna showing an embedded air cavity [37] 53

Figure 3-23: ACMP antenna with cavity [38]. 54

Figure 3-24: Aperture coupled microstrip with an embedded air cavity [40]. 54

Figure 3-25: (a) Geometry of the proposed LTCC multi-layer antenna. (b) Geometry of the proposed Rogers multi-layer antenna [41]... 56

Figure 3-26: Meshed stacked LTCC antenna configuration [42] 57

Figure 3-27: Cross section of transition from coaxial connector to stripline [45]....................... 59

Figure 3-28: The geometry of transition from microstrip to stripline [44].................................. 59

Figure 3-29: Configuration of a GCPW to Stripline vertical transition [46]............................... 60

Figure 3-30:Configuration of a CPW to stripline vertical transition [47]. 60

Figure 3-31: DSL-to-DGCPW transition [48]. 61

Figure 4-1: Transition structure (a) SMPM coaxial connector to LTCC stripline transition. (b) SMPM connector bottom view. 64

Figure 4-2: (a) Expanded view of the proposed coaxial-to-stripline transition (b) Metal layers details of the proposed transition. ... 66

Figure 4-3: The S parameters of the transition between coaxial and strip line. ... 67

Figure 4-4: The geometry of the back-to-back configuration ... 68

Figure 4-5: The geometry of a simple stripline ... 69

Figure 4-6: Simulated results of the back-to-back configuration (a) Return loss (b) Insertion loss ... 69

Figure 5-1: Simulated single element antenna ... 74

Figure 5-2: Configuration of the single element antenna. (a) Expanded view. (b) Metal layer details ... 75

Figure 5-3: Simulated return loss of the proposed single element antenna. ... 76

Figure 5-4: 3D realized gain pattern for the proposed single element antenna @ 28GHz ... 76

Figure 5-5: Single element realized gain radiation pattern for 25-32GHz (a): cut φ=0° (b): cut φ=90° element antenna ... 77

Figure 5-6: The realized gain of the proposed single-element antenna as a function of frequency. ... 78

Figure 5-7: The geometry of the proposed single element antenna connecting to SMPM Rosenberger connector. (a): Top view (b): bottom view ... 80

Figure 5-8: Expanded view of the single element antenna with an SMPM connector. ... 81

Figure 5-9: Metal layer details of the single element antenna with an SMPM connector. ... 82

Figure 5-10: Simulated return loss of a single element antenna with a SMP connector ... 83

Figure 5-11: 3D realized gain pattern for the proposed single element antenna with a SMPM connector. ... 83

Figure 5-12: realized gain radiation pattern of single element Antenna connecting to SMPM connector for 25-32GHz (a): cut φ=0° (b): cut φ=90°. ... 84

Figure 5-13: The realized gain of the proposed single-element antenna attached to SMPM connector. ... 85

Figure 6-1: (a): the footprint of the connector on the board (b): The bottom side of the connector ... 86

Figure 6-2: The failure pattern for: (a): the leaded paste (b): the unleaded paste ... 87

Figure 6-3: (a) Top view of the proposed single element antenna (b)Bottom View of the proposed single element antenna (c) Fabricated coaxial SMPM-to-LTCC Stripline transition 88

Figure 6-4: Measurement setup block diagram for the proposed antenna and transition. 89

Figure 6-5: Measured and simulated results of the back-to-back configuration (a) Return loss (b) insertion loss. 90

Figure 6-6: Measured and simulated return loss of proposed single element antenna. 91

Figure 6-7:Boresight radiation pattern for the proposed antenna with and without an SMPM connector (a) cut φ=0° (b) cut φ=90°. 93

Figure 6-8: (a) The proposed single-element antenna with and without SMPM connector and the same size 94

Figure 6-9: Realized gain radiation pattern for the single element antennas with and without considering the connector and same sizes 94

List of Symbols, Abbreviations and Nomenclature

Symbol	Definition
LTCC	Low Temperature Co-Fired Ceramic
HTCC	High Temperature Co-Fired Ceramic
SMPM	Sub-Miniature-Push on Micro
HFSS	High-Frequency Structure Simulator
ACMPA	Aperture Coupled Microstrip Antenna
LTE	Long-Term Evolution
5G	Fifth generation mobile network
BW	Bandwidth
Rx	Receiver
Tx	Transmitter
EM	Electromagnetic
IC	Integrated Circuit
IoT	Internet of Things
MCM	Multilayer/3D microstrip module
SiP/SoP	System -in/on-package
TE	Transverse Electric
TM	Transfer Magnetic
EMC	Electromagnetic Compatibility
FR4	Flame Resistant 4
IEEE	Institute of Electrical and Electronics Engineers
GPS	Global positioning system
DBS	Direct Broadcast Satellite
ε_r	dielectric constant
RCS	Radar Cross Section
FDTD	Finite-Difference Time-Domain
Q	Quality factor
ASP	Aperture-Stacked Patch
SPSs	Stacked Parasitic Strips
DSL	Differential Stripline
SMD	Surface-Mount Device
AiP	Antenna-in-Packaging
LOS	line-of-sight
NLOS	Non-Line-of-Sight
EBG	Electromagnetic Band Gap
PBG	Photonic-Band Gap
SLL	Sidelobe Level
BLL	Back Lobe Level
X-pole	Cross-Polarization
MAC	Medium Access Control
FR2	Frequency Range 2

Chapter One: Introduction

1.1 Introduction

With the exponential growth of mobile data demand, the fifth generation (5G) mobile network has emerged in recent years. By using a large unlicensed frequency band, 5G has enhanced communication capacity. Indeed, millimeter waves (mm-waves) provide incredible bandwidth from 30 GHz to 300 GHz for multi-gigabit communication services, which are claimed to be leading applications of 5G like high-definition television (HDTV) and ultra-high-definition video (UHDV). Most of the current research in 5G applications is focused on 28, 38, 60, 71-76, and 81-86 GHz. Several existing standards defined for indoor wireless personal area networks (WLAN), such as ECMA-387, IEEE 802.15.3c, and IEEE 802.11ad, illustrate growing interest in cellular systems or outdoor mesh networks in the mm-wave band.

There are fundamental differences between mm-wave communication and other communication systems in the microwave band (e.g., 2.4 and 5 GHz). There are many challenges in the physical (PHY), medium access control (MAC), and routing layers in mm-wave communications. Challenges like the high propagation loss, directivity, sensitivity to blockage, and the channel's dynamics due to the mobility of end-users should be considered in architectures and protocols. Mm-wave communications have enormous propagation loss owing to the high carrier frequency, and beamforming (BF) has been approved as an essential technique, for mm-wave communications. Moreover, because of weak diffraction ability, mm-wave communication is sensitive to blockage by obstacles like humans and furniture [1].

The 5G standard deployment at mm-wave bands (FR2) is coming up as a response to growing demand for much greater throughput (1G b/s or higher), much lower latency (less than 1 ms), and ultra-high reliability. Since the current Long-Term Evolution (LTE) spectrum under 6 GHz is crowded and fragmented, mm-wave frequency band has attracted more interest in 5G. The vast amount of unused spectrum in the mm-wave band can support the higher data rates required in future mobile broadband access networks. Furthermore, because of the relatively small mm-wave wavelength, building massive antenna arrays (e.g., with 32 or more elements) is feasible in this frequency band, which provides further gains from spatial isolation and multiplexing. However, the high carrier frequency makes the propagation conditions more challenging. For instance, blockages become very important because mm-wave signals do not penetrate most solid materials like brick buildings. Another feature of 5G is using many more base stations deployed according to the heterogeneous network (HetNet) paradigm. As more base stations become distributed in the urban area, less cost per base station is required.

1.2 Characteristics of mm-wave communications

To fully utilize mm-wave communications, distinct channel characteristics should be considered in the network architecture design. In what follows, some challenges are described.

1.2.1 Channel Measurements

The mm-wave bands have more propagation loss than conventional systems using lower carrier frequencies. The rain attenuation, atmospheric (such as air density) and molecular (such as dust) absorption characteristics of mm-wave propagation limit the range of mm-wave communications, as shown in Figure 1.1 and Figure 1.2. However, according to Figure 1.1 and Figure 1.2, the propagation loss of the cells, in which the distance between a receiver and a transmitter is less than 200 m, does not create significant additional path loss. Particularly at 28 GHz and 38 GHz. For heavy rainfall rates of 1 inch/h, only 7dB/km of attenuation is expected at

28 GHz, which means just 1.4dB of attenuation over a 200m distance. Accordingly, small cell access, backhaul, and indoor applications can be supported by mm-wave communications [2].

The line-of-sight (LOS) channel attenuates less than the non-line-of-sight (NLOS). Urban propagation at 28GHz was tested in NY. The receiver (Rx)-transmitter (Tx) distance varied between 75 and 125 meters. The average path loss for LOS and NLOS were 2.55 dB and 5.76 dB, respectively. Therefore, to avoid severe propagation loss, directional antennas are used at the transmitter and the receiver to achieve a high antenna gain. At 28 GHz, penetration and reflection losses were measured on indoor obstacles (such as drywall and clear non-tinted glass) and outdoor ones (such as brick pillars and tinted glass). The test results showed that outdoor materials' reflection coefficients were more significant than indoor materials [3].

The features of mm-wave communications in different bands are illustrated in Table 1-1. At 200 m, oxygen absorption and rain attenuation are low for 28 and 38 GHz, although 60 GHz and 73GHz are higher values [3].

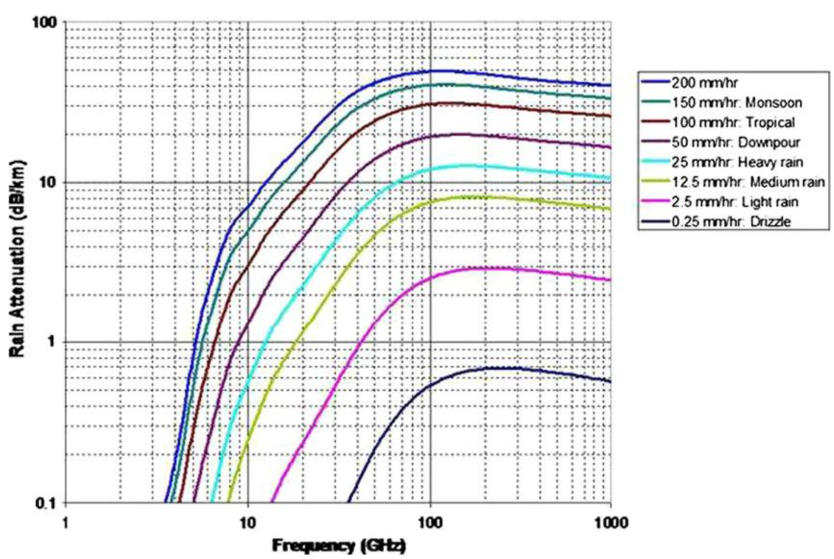

Figure 1-1: Rain attenuation at microwave and mm-Wave frequencies [4].

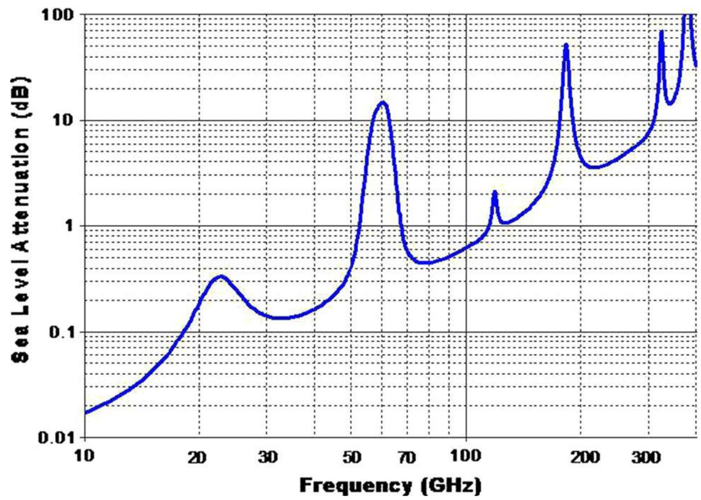

Figure 1-2: Atmospheric and molecular absorption at mm-wave frequencies [4].

Table 1-1: Mm-wave propagation characteristics [4].

Frequency Band		28 GHz	35 GHz	60 GHz	73 GHz
Path loss exponent	LOS scenario	1.8 ~ 1.9	1.9~2.0	2.23	2
	NLOS scenario	4.5~4.6	2.7~3.8	4.19	2.45~2.69
Rain attenuation at 200 m	5 mm/h	0.18 dB	0.26 dB	0.44 dB	0.6 dB
	25 mm/h	0.9 dB	1.4 dB	2 dB	2.4 dB
Oxygen absorption at 200m		0.04 dB	0.03 dB	3.2 dB	0.09 dB

1.2.2 Directivity

In the mm-wave band, the increased carrier frequency makes the propagation conditions more demanding. For instance, as mm-wave signals do not penetrate most solid materials, blockage is an important issue. In order to obtain a sufficient link budget in wide area networks, a highly directional antenna will be needed at both the base station and the mobile terminal to combat the substantial isotropic propagation loss at these frequencies [1]. Therefore, by controlling the phase of the transmitted signal by each antenna element, the antenna array is able to steer its beam toward any desirable direction. Hence, this phase distribution at antenna elements leads to achieving a high gain in the desired direction and a low gain in all other directions. In actual situations, beamforming should be considered; the procedure of beam training is required to make the transmitter and receiver direct their beam toward each other [5], and various beam training algorithms have been proposed in this regard [6], [7], [8].

1.2.3 Sensitivity to blockage

The diffraction phenomenon is the result of interference and is most significant where the wavelength of the radiation is comparable to the linear dimension of the obstacle. Accordingly, in mm-wave bands, owing to small wavelengths, electromagnetic waves have a weak ability to diffract around the obstacle. For instance, at 60 GHz, a human's loss of blockage was found to be between 20 and 30 dB. Maintaining a reliable connection for delay-sensitive applications is a considerable challenge for mm-wave communications.

1.3 Phased array antenna

Mm-wave technology is a promising candidate for growing data traffic in 5G wireless communications and beyond. However, in order to take advantage of the promised bandwidth available in the mm-wave regime, challenges related to free-space propagation loss, atmospheric absorption, scattering, and non-line-of-sight propagation must be addressed. Phased array technology is thought to be required in this area to provide the market with high-speed and seamless wireless solutions. It can be defined as a multiple-antenna system that electronically controls the radiated electromagnetic (EM) beam.

The first electronically scanned phased array radar was designed by Luis Walter Alvarez in the early 1940s. Phased arrays have received growing interest from the industry because of their ability to shape or steer a radiated beam and the possibility of integrating such a versatile solution at mm-wave radio link. Although phased arrays have been considered for many years for large radar applications and communication links, their high cost limited their use for commercial applications. However, the growth of new architectures, packaging, as well as semiconductor technologies has incredibly lessened the cost and complexity of phased arrays. It has made them available to commercial markets for 5G wireless and satellite applications. Antennas with high gains are needed to overcome path losses and ease restrictions at the integrated circuit (IC) levels. Phased array antenna can be low profile and high beam control.

In a phased array antenna, the amplitude and phase profile can be adjusted finely, resulting in a radiation pattern using the multiple (N) RF accesses. The amplitude control mainly adjusts the sidelobe level and the half-power beamwidth at the expense of lower efficiency because the power amplifiers (PAs) are not contributing at maximum to the overall output power. Phase control not only drives the beam directions but also can be used to reduce or cancel out the radiation in specific directions. It also helps improve the signal-to-noise ratio [9].

1.4 LTCC Technology

The mm-wave technology, due to its merits like high speed, bandwidth, and resolution, has attracted a growing interest in commercial and military applications, including broadband wireless (together with 5G and beyond), the Internet of Things (IoT), multimedia, space and defense, automotive radar, imaging sensors, and biomedical devices. For these applications, the critical challenge to industries is the integration and packaging of mm-wave modules in a compact size with a low cost while maintaining high reliability and repeatability. The multilayer/3D microstrip module (MCM) or system-in/on-package (SiP/SoP) with the antenna-in-package technology, along with high quality (high-Q) off-chip passive components and interconnects, are presented as solutions for these advanced requirements.

Recently, many research activities have been underway to realize mm-wave modules. In between, thick-film (TF)-like processes such as organic, laminate, and ceramic based [including low-temperature co-fired ceramics (LTCCs)] MCMs are popular because of their lower-cost, straightforward fabrication process [10].

Accordingly, LTCC technology owing to its high compactness and mature multilayer fabrication capability, has emerged as an interesting solution for millimeter-wave radars and high data-rate wireless communication systems which require compact, high-performance, and low lost antenna. However, because of the high dielectric constant of LTCC materials, microstrip antennas fabricated on LTCC materials suffer from narrow bandwidth and low gain. This problem can be solved to a large extent by using several methods, including the thick substrate, embedded air cavities to lower the effect of dielectric constant, different shapes patches and probes, and to cut slots and stacked patches [11].

This ceramic structure is created from stacked layers of thin, soft, and flexible ceramic so they can be easily cut into various shapes. Conductive, dielectric, and/or resistive pasts can be applied on these sheets, and also Inter-layer connections are possible by using filled vias. The single tapes have to be laminated all together and then fired at once, which leads to saving time and money and reducing circuit dimensions. Additionally, it is possible to employ low-resistive materials like silver and gold instead of molybdenum and tungsten, which must be used in conjunction with the HTCC (High Temperature Co-fired Ceramic) due to the firing temperature's low level of roughly

850°C. Layers are hardened and combined for good after a co-firing process which provides robust construction with high resistance to different environmental conditions [12].

In what follows, the advantages of LTCC structures compared to an ordinary multi-layer laminate structure, such as FR4, are summarized [13].

- Lower loss dielectric
- Applicable to produce modules in low-cost SMT packages (BGA, QEP, PLCC, etc.) and also bare dies.
- The capability to use cavities and integral heat sinks
- Capability to use embedded passive components such as resistors, inductors, and capacitors
- Better-controlled dielectric properties

1.5 Motivation

The interest in millimeter-wave radars and high data-rate wireless communication systems has increased the requirements for compact, high-performance, and low-loss antennas. Accordingly, LTCC technology, owing to its high compactness and mature multilayer fabrication capability, has emerged as a solution for these requirements.

On the other hand, a wide bandwidth system is needed for such a large data rate. Aperture-coupled antennas show large bandwidth, perfect cross-polarization, and efficiency compared to conventional microstrip antennas. They are low profile, easy to integrate, and low cost. Because the conductor layers in LTCC materials are screen-printed, aperture-coupled microstrip antennas are an appropriate option to reduce back radiation which is undesirable in mobile communications

[14]. Additionally, its structure is compatible with LTCC technology, which is made of thin layers. This work provided a mm-wave wideband LTCC antenna for 5G applications taking into account all of these issues. Furthermore, to feed and test the proposed antenna, a Sub-Miniature-Push on Micro (SMPM) coaxial connector to LTCC stripline transition is designed and implemented for the k and ka bands.

1.6 Objective

This work investigates a wideband LTCC aperture-coupled microstrip patch antenna (ACMPA). The purpose is to design an antenna element for an active antenna array for 5G applications. Detailed design procedures, simulation, and experimental results are presented. The thesis contributions can be listed as follows:

1. To design a single element mm-wave wideband LTCC antenna fed by stripline.
2. Design and fabrication of an SMPM coaxial connector to LTCC stripline transition.
3. Design and fabrication of a single element mm-wave wideband LTCC antenna fed by SMPM coaxial connector.

The targeted design of the single ACMPA is intended to be used as the building block for a mm-wave phased array antenna system that would offer high gain and beam steering capability suitable for 5G applications. This latter is out of the scope of my Master project.

1.7 Dissertation Overview

The dissertation is organized into seven chapters. The motivation and overview of the dissertation are presented in chapter 1. Chapter 2 gives relevant background information on the patch antenna and describes different stages in the LTCC fabrication process. A literature review on broadband patch antenna and different stripline-to-coaxial transitions in LTCC is presented in chapter 3. Chapter 4 presents the design and simulation results of the proposed SMA coaxial connector to LTCC stripline transition. Chapter 5 provides a detailed analysis and simulation results of the proposed LTCC mm-wave broadband antenna. The investigation was carried out using computer simulation performed by the HFSS commercial EM software package. Chapter 6 presents measurements for the proposed antenna and transition. Conclusions are then presented in chapter 7.

Chapter Two:BACKGROUND

2.1 Introduction

According to IEEE, an antenna is a part of a transmitting or receiving system, which radiates or receives electromagnetic waves. In other words, an antenna as a transducer converts a guided wave on a transmission line to a free-space electromagnetic wave or vice versa [15]. There are different antennas, including wire antennas, aperture antennas, microstrip antennas, reflector antennas, lens antennas, and so on. However, microstrip antennas are of high interest because of their numerous advantages.

The concept of the microstrip radiator was proposed in 1953 by Deschamps, and its development was accelerated by the availability of suitable substrates with low loss-tangents and attractive thermal and mechanical properties during the 1970s. Numerous merits of this type of antenna, such as low volume, lightweight, low cost, conformal configuration, compatibility with integrated circuits, and so forth, have led to diversified applications.

In the most straightforward configuration, a microstrip antenna consists of a radiating patch on one side and a ground plane on the other side of a dielectric substrate. The conductors used for patch antennas are usually copper or gold, and the patch shape can assume virtually any form. However, regular forms are favoured for straightforward analysis and performance prediction [16].

This chapter discusses the basic parameters that characterize the behavior of any antenna, especially patch antennas.

2.2 Radiation Pattern

An antenna radiation pattern is defined as “a mathematical function of graphical representation of the radiation properties of the antenna,” and it is a function of space coordinates and is mainly determined in the far field region. In brief, a radiation pattern is an angular variation of radiation level around an antenna.

A graph of the received electric (magnetic) field along a constant radius is called the amplitude field pattern. A trace of the spatial variation of the power density at a constant radius is called the amplitude power pattern [15].

2.3 Directivity

Directivity identifies how much an antenna concentrates energy in one direction to radiation in other directions. It is defined as the ratio of the radiation intensity in a given direction from the antenna (U) to the radiation intensity averaged over all directions (U_0). The average radiation intensity is equal to the total power radiated by the antenna divided by 4π [15].

In other words, the directivity of an antenna is equal to the ratio of its radiation intensity in a given direction with respect to an isotropic antenna.

$$D = \frac{U}{U_0} = \frac{4\pi U}{P_{rad}} \qquad (2.1)$$

D : *Directivity*
U : *The radiation intensity in a given direction*
U_0 : *The average radiation intensity*
P_{rad} : *The total power radiated by the antenna*

The directivity of an antenna is equal to its gain if the antenna is 100% efficient.

2.4 Gain

Directivity can be determined only by the radiation pattern of an antenna. However, when an antenna is used in a system, for example, as a transmitting antenna, how efficiently the antenna transforms available power at its input terminals into radiated power becomes more important. Hence, the gain is 4π times the ratio of the maximum radiation intensity to the net power accepted ($P_{accepted}$ or P_{in}) by the antenna from the connected transmitter.

$$G = \frac{4\pi U_m}{P_{in}} \tag{2.2}$$

$G : Gain$
$U : The\ radiation\ intensity\ in\ a\ given\ direction$
$U_m : The\ maximum\ radiation\ intensity$
$P_{in} : The\ net\ power\ accepted\ by\ the\ antenna$

The gain definition does not include losses due to mismatches of impedance or polarization [17].

2.5 Realized Gain

An antenna's realized gain is 4π times the ratio of the maximum radiation intensity to the incident power. The incident power ($P_{incident}$) is the power towards the ports (as defined in the edit source in HFSS)

$$\mathrm{Re}\, alizedGain = \frac{4\pi U_m}{P_{incident}} \tag{2.3}$$

$U_m : The\ maximum\ radiation\ intensity$
$P_{incident} : The\ net\ power\ accepted\ by\ the\ antenna$

Losses resulting from reflection at the input terminals and losses inside the antenna's construction are taken into account when calculating the antenna's overall efficiency. Figure 2-1 casts light on the difference between radiated power, accepted power (net power), and incident power.

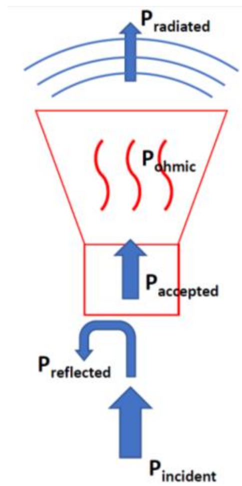

Figure 2-1: The distinction between incident power, accepted power (net power), and radiated power

2.6 Radiation Efficiency

Comparing formulas 2.1 and 2.2, we see that the only difference between gain and directivity is the power value used. If all input power (accepted power) appeared as radiated power ($P_{in} = P_{rad}$), the directivity would equal the gain. In other words, the gain definition considers ohmic loss on the antenna [17].

Radiation efficiency (e_r) is defined as the ratio of radiated power to the input power:

$$e_r = \frac{P_{rad}}{P_{in}} \tag{2.4}$$

Radiation efficiency is bounded as

$$0 \le e_r \le 1 \tag{2.5}$$

Considering $P_{rad} = e_r P_{in}$ and equations 2.1 and 2.2:

$$G = e_r D \tag{2.6}$$

2.7 Total efficiency

The total efficiency is the radiated power over the incident power.

2.8 Bandwidth

An antenna's bandwidth is the range of frequencies within which its performance fulfills particular requirements. In practice, the bandwidth is determined by the -10 dB points of the reflection coefficient. For a narrowband antenna, the bandwidth is defined as the percentage of the difference of upper frequency and lower frequency over the center frequency of the bandwidth. For broadband antennas, the bandwidth is usually defined as the ratio of the upper-to-lower frequencies of an acceptable operation [15].

2.9 Principle of Pattern Multiplication

The pattern multiplication principle states that the radiation patterns of an array consisting of identical elements are the product of the element pattern and the array pattern. An array Pattern is defined as an array of isotropic point sources with the same locations, relative amplitudes, and phases as the original array [17].

$$F(\theta,\varphi) = g_a(\theta,\varphi) f(\theta,\varphi) \tag{2.7}$$

Where $g_a(\theta,\varphi)$: the normalized pattern of a single element of the array (element pattern)

$f(\theta,\varphi)$: the normalized array factor.

If mutual coupling effects are included:

$$F(\theta,\varphi) = g_{ae}(\theta,\varphi) f(\theta,\varphi) \tag{2.8}$$

Where:

$g_{ae}(\theta,\varphi)$: the average active element pattern, which is the normalized pattern for a typical center element in the array.

$f(\theta,\varphi)$: the normalized array factor

$F(\theta,\varphi)$: the normalized array pattern

2.10 Planar Array

Linear arrays can be phased-scanned in only one plane containing the line of the element centers, and the beamwidth in a plane perpendicular to the mentioned plane is determined by the radiating element beam in that plane. This limits the gain and avoids forming radiation patterns like pencil beams. As a result, for applications requiring a high gain, pencil beams, or beam scanning capability in any direction, multidimensional arrays are used.

The perimeter of planar arrays is usually circular, rectangular, or square in shape. Figure 2-2 shows a planar array with a rectangular perimeter, and dx and dy are element spacings in the principal planes.

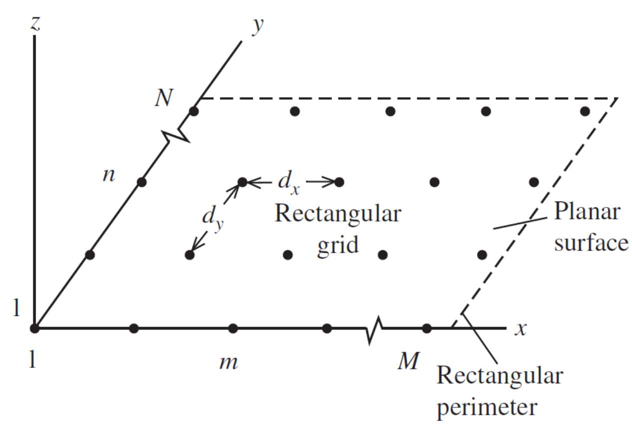

Figure 2-2: The geometry of a planar array [17].

As long as the elements in an array are identical, the array multiplication principles developed in the previous part could be applied to arrays of any geometry. Consequently, it allows us to focus on only array factor when studying multidimensional arrays.

The array factor for an arbitrary array is calculated as follows. The position of a given *mn*th element in an arbitrary three-dimensional array is usually defined with its respective position vector from the origin to the *mn*th element.

$$r'_{mn} = x'_{mn}\hat{x} + y'_{mn}\hat{y} + z'_{mn}\hat{z} \tag{2.9}$$

The array factor is:

$$AF = \sum_{n=1}^{N}\sum_{m=1}^{M} I_{mn} \exp(j(\beta\hat{r}.r'_{mn} + \alpha_{mn})) \tag{2.10}$$

Where:

$$\begin{aligned}
&\zeta_{mn} = \beta\hat{r}.\hat{r}'_{mn} = \beta(\hat{x}\sin\theta\cos\varphi + \hat{y}\sin\theta\sin\varphi + \hat{z}\cos\theta).(x'_{mn}\hat{x} + y'_{mn}\hat{y}) \\
&= \beta[x'_{mn}\sin\theta\cos\varphi + y'_{mn}\sin\theta\sin\varphi] \\
&\alpha_{mn} = -\beta(x'_{mn}\sin\theta_0\cos\varphi_0 + y'_{mn}\sin\theta_0\sin\varphi_0) \\
&\theta_0, \varphi_0 : \text{main beam pointing direction}
\end{aligned} \tag{2.11}$$

Note that the Z-axis is normal to the plane of the array.

2.11 Surface Wave

Although many people associate transmission lines with either coaxial and twin lead lines or metal pipes (usually referred to as waveguides), with parts of their structure being metal, dielectric slabs and rods with or without any associated metal can serve as transmission lines as well. Usually, these structures are referred to as dielectric waveguides supporting the field modes, which are known as surface wave modes. In a dielectric slab waveguide, like any type of waveguide, the objective is to contain and direct the energy within the structure and toward a given direction. For a dielectric slab waveguide, this is carried out by having the wave bounce back and forth between its upper and lower interfaces at an incident angle greater than the critical angle of $\theta_c = \sin^{-1}\sqrt{\frac{\varepsilon_2}{\varepsilon_1}}$ (In Figure 2-3 $\varepsilon_2 = \varepsilon_0$ So $\theta_c = \sin^{-1}\sqrt{\frac{1}{\varepsilon_{r1}}}$) [18].

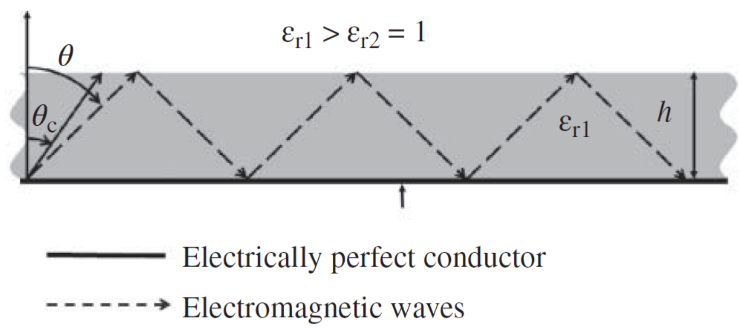

Figure 2-3: Full reflection between the boundary of two media with different dielectric constants [19].

The surface wave at both transverse electric (TE) and transverse magnetic (TM) modes can be excited in the grounded dielectric layer [19].

The cutoff frequency of the modes is given by

$$f_c = \frac{nc}{4h\sqrt{\varepsilon_{r1} - 1}}$$

where:

c: the speed of light in free space.

n=0,1,2, ... for TM_n and TE_{2n+1} surface modes.

h: dielectric slab thickness

The dominant mode is the TM0, an odd mode with its cutoff frequency is zero, which means that regardless of operating frequency, the TM0 mode will always propagate un-attenuated. Other higher modes can be suppressed by selecting a frequency of operation lower than their cutoff frequencies [18]. Thus, the surface waves are trapped by the dielectric layer grounded by a PEC surface, and in a dielectric slab with a higher dielectric constant, more energy becomes trapped. Moreover, an electrically thick dielectric layer with either higher operating frequencies or physically larger thickness traps more energy with more TM and TE surface modes.

The trapped surface wave energy propagates along the surface and can be reflected by the discontinuity of the medium and/or can disappear owing to the dissipative medium or leaky waves [19].

2.11.1 Surface Wave in Microstrip Patch Antenna

It is possible to ignore the surface wave produced in microstrip architectures with an electrically thin-grounded dielectric substrate. For instance, in a microstrip patch with a substrate thickness of about h=0.01λ_0 (λ_0 is the operating wavelength in free space), a typical value of $0.813 \sim 1.626\,mm$, and a relative dielectric constant lower than 5 (such as FR4) at a lower microwave band (such as operating frequencies lower than 10 GHz) surface waves can be ignored. However, at mm-wave bands of 30-300 GHz, the operating wavelengths are much smaller, which causes the grounded dielectric with a typical thickness of $32 \sim 64\,mil$ electrically thicker. Therefore, when the electromagnetic waves are excited in the PCB, such a described dielectric layer very likely generates surface waves. As a result, at mm-wave bands, the effects of surface waves on the performance of the microstrip patch antenna are not negligible and should be considered in the design. Unlike the ohmic losses produced by a lossy dielectric and imperfect conductors, wherein the energy is converted to heat, the loss from the surface wave involved in the radiation usually distorts the radiation from the radiator and decreases the gain of the antenna.

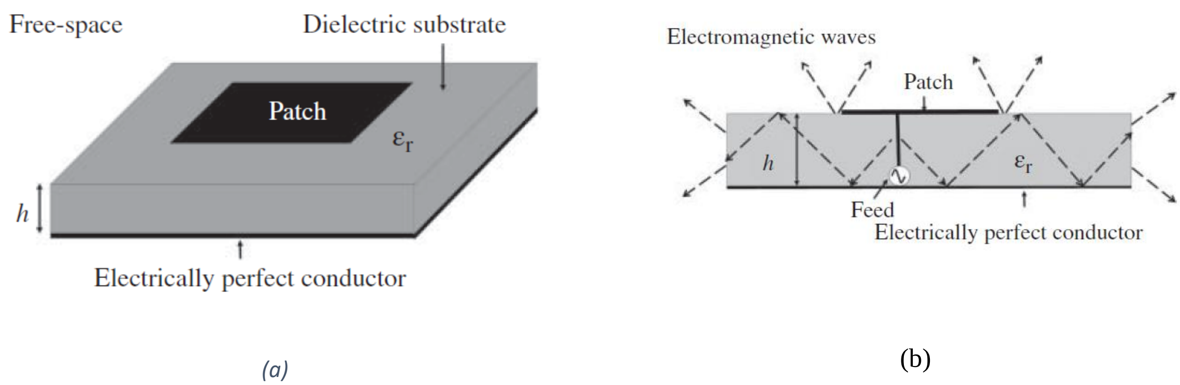

Figure 2-4: (a) The sketch of a probe-fed microstrip patch antenna and (b) electromagnetic waves in a microstrip patch antenna of arbitrary shape [19].

2.11.2 Surface Waves Effects on Microstrip Patch Antenna

Surface waves affect antenna performance by reducing the radiation efficiency and distorting the radiation pattern. When the substrate of the patch antenna is infinitely sized, the energy distributed by the surface wave is trapped in the substrate. Although surface waves do not contribute to the radiation of the antenna, the existence of the surface wave lessens the radiation efficiently because part of the feeding energy is trapped instead and not being radiated. In the case of a patch antenna printed on a finite-size substrate, the effect of the surface wave becomes more severe. In fact, when the surface waves reach the edge of the dielectric substrate, they radiate into space and may cause higher side lobe levels, higher cross-polarization levels, and/or pattern distortion with ripples. Furthermore, the diffracted surface modes may be coupled into the other circuits on the dielectric substrate and/or behind the ground layer. This results in more losses and even electromagnetic compatibility (EMC) issues.

2.11.3 Suppressing Surface Wave in Microstrip Patch Antenna

The suppression of the undesired surface wave in the microstrip patch antenna, especially at the mm-wave band with an electrically thick dielectric substrate (large thickness and/or high permittivity), is critical in the design. In what follows, I will explore some methods to suppress surface waves [19].

1. A suspended patch antenna suppresses surface waves and broadens the impedance bandwidth. As demonstrated in Figure 2-5 it is carried out by substituting the patch antenna's substrate with a dielectric with a significantly lower permittivity, such as air. In this case, the patch is mounted on spacing material like Styrofoam ($\varepsilon_r = 1.07$) or plastic posts. It should be considered that this type of suspended patch antenna has a larger physical size and is not appropriate for configuring large-scale antenna arrays.

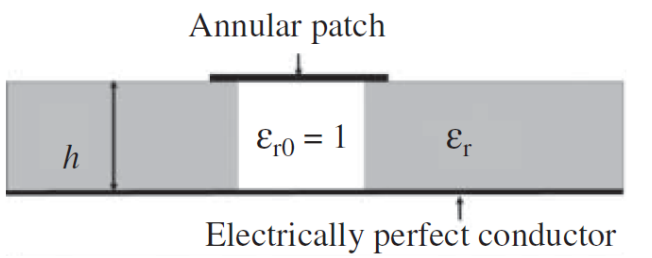

Figure 2-5: The annular patch having a central air core [19].

2. To perforate the substrate, i.e., drill holes in the substrate to have a lower dielectric constant substrate.
3. To synthesize a lower dielectric constant by partially removing the substrate surrounding the patch, which is more practical compared to the previous solution.
4. A cavity under the microstrip patch is also used to suppress the generation of surface waves, as shown in Figure 2-6.

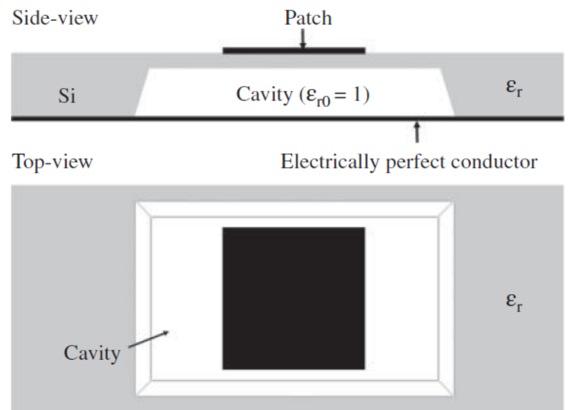

Figure 2-6: The cavity backed microstrip patch antenna [19].

5. Photonic-bandgap (PBG) or electromagnetic bandgap (EBG) structures can suppress surface waves, mainly operating at TM0 modes. The EBG structure can be created by drilling thin holes in the dielectric substrate or arraying narrow dielectric cylinders surrounding the patch.
6. As shown in Figure 2-7, two-dimensional periodic patch structures can block the surface wave from propagating at a specific frequency band.

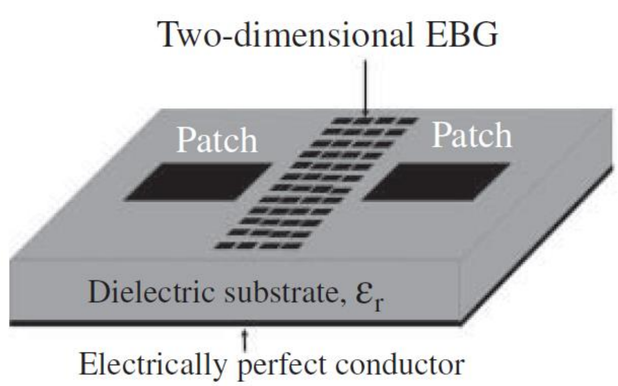

Figure 2-7: The EBG structure used for improving isolation between the patch antennas [19].

2.12 Conclusion

This chapter discusses the theoretical background of different parameters of antennas, such as gain, directivity, efficiency, and planar array. In addition, surface wave and their effects on microstrip antenna performance and different methods to suppress the surface wave in microstrip patch antennas are discussed briefly.

Chapter Three: LITERATURE REVIEW ON BROADBAND CAVITY-BACKED LTCC PATCH ANTENNA

3.1 Introduction

Recent years have seen a huge increase in the importance of microstrip antennas due to their low profile, low cost, simple integration into arrays or with microwave-integrated circuits, as well as their polarization variety [20]. These characteristics allow them to be used in both commercial and civil applications, such as mobile satellite communications, the direct broadcast satellite (DBS) system, terrestrial cellular communications, the global positioning system (GPS), and remote sensing, in addition to military applications, such as aircraft, missiles, rockets, and spacecraft.

Microstrip antennas suffer from low efficiency, low power, high Q, poor polarization purity, spurious feed radiation, poor scan performance, and narrow bandwidth. Although a narrow bandwidth is desirable in some applications like government security systems, many techniques to improve the bandwidth from a few percent to tens of percent have been presented in recent years.

This chapter will cover the literature review for microstrip patch antenna’s technical features, advantages, and disadvantages, excitation techniques, techniques to broaden the bandwidth, features of the cavity-backed patch antennas, and finally, LTCC technology.

3.2 Characteristics of Microstrip Patch antenna

A microstrip antenna is initially only a metallic patch printed on a thin, grounded dielectric substrate. The most common patch forms are circular and rectangular, while there are more possibilities. In order to ensure proper spacing and mechanical support between the patch and ground layer, the substrate's thickness is generally between 0.01 to 0.05 free-space wavelength (λ_0). Substrate materials should have a low in insertion loss with a loss tangent of less than 0.005, especially for large array applications. According to their relative dielectric constant (ε_r), substrate materials are often categorized into three groups:

1. Substrate materials that have ε_r in the range of 1.0-2.0, such as air, polystyrene foam, or dielectric honeycomb
2. Substrate materials with ε_r between 2.0 and 4.0 mainly consist of fiberglass-reinforced Teflon.
3. Substrate materials with ε_r in the range of 4.0-10. This material can consist of ceramic, quartz, alumina, or LTCC.

Although there are substrate materials with ε_r greater than 10, employing these materials should be done with caution as they lower the antenna's radiation efficiency. The intended patch size, bandwidth, thermal stability, insertion loss, cost, and other factors all play roles in choosing the right substrate materials.

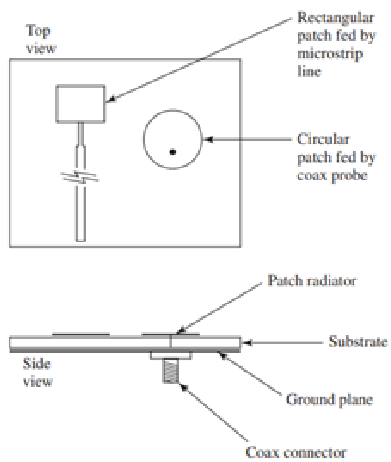

Figure 3-1: Configuration of microstrip patch antenna [21]

3.2.1 Advantage and Disadvantage Trade-offs

The advantages of microstrip antenna compared to other conventional antennas are the following.

1. Microstrip antennas have a low profile, are lightweight, take up little room, can adapt to both flat and curved surfaces, and are simple to integrate with integrated microwave circuits [22].
2. A straightforward etching procedure can create large numbers of patch elements or arrays of patch elements at a much lower cost.
3. By using techniques such as stack patches, patches with a loaded pin, or a stub, multiple-frequency operation is feasible.
4. Microstrip antennas have low radar cross section (RCS), which is very important in miscellaneous applications. They can be combined with reflector array technology to achieve large apertures without using an RF loss beamformer.

The disadvantages of microstrip antenna are the following [21].

1. A single patch microstrip antenna generally has a narrow bandwidth (less than 5%). However, by using some techniques like stacked patches, a thicker substrate with aperture slot coupling, external matching circuits, U-slot feed, an L-shaped probe feed, and so on, a bandwidth of up to 50% is achievable.
2. Because there is a small space between its ground plane and radiating patch, the microstrip antenna can withstand lower RF power (a few tens of watts or less). However, it may be enhanced in accordance with the substrate thickness, the frequency of use, and the metal edge sharpness.

3. Compared to other arrays with comparable aperture sizes, the microstrip array has a higher ohmic insertion loss. The metal conductor and dielectric substrate of the power divider circuit's microstrip line are where the ohmic loss often occurs. It should be considered that relatively small loss occurs in a single patch element, which is around one-half wavelength long. By utilizing various techniques, such as waveguide and microstrip combined power divider, series feed power divider line, and so forth, the loss in the power dividing circuit may be decreased.

3.2.2 Analysis and Design

The microstrip antenna may be analyzed using a variety of techniques. These techniques assist the designer without tedious experimental iteration and in learning the physical principles behind the operation of the microstrip antenna. The transmission-line circuit model, multimode cavity model, moment approach, finite-difference time-domain (FDTD) method, and finite-element method are the most widely used techniques for microstrip antenna analysis. This chapter will briefly discuss the transmission line and cavity model only.

3.2.2.1 Transmission-Line Model

A microstrip patch operating at its fundamental modes has one-half wavelength long and can be represented by an equivalent circuit network. As illustrated in Figure 3-2, the two sides of a square or rectangular patch with two equivalent slots along the resonating dimension primarily provide the patch's radiation. Hence, the microstrip patch can be characterized by two slots that are separated by a transmission line, where each slot is represented by a parallel circuit of a conductance (G) and a susceptance (B). The complete patch antenna can be modeled by the equivalent network shown in Figure 3-3.

The transmission-line model is straightforward and computationally efficient, and provides valuable physical insight while having lower accuracy and a difficulty in modeling coupling effects. For example, it cannot model the radiation from the non-radiating edges of the patch [21].

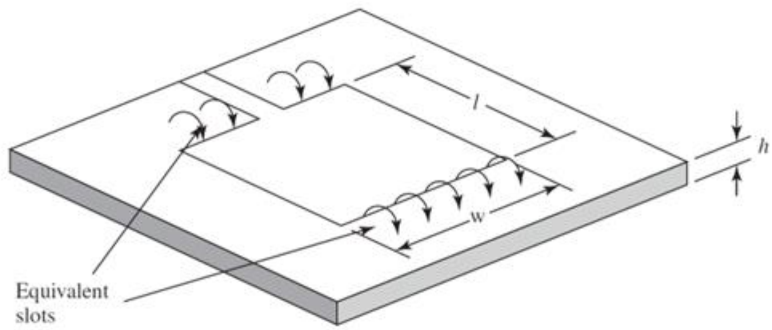

Figure 3-2:Microstrip patch radiation source represented by two equivalent slots [21].

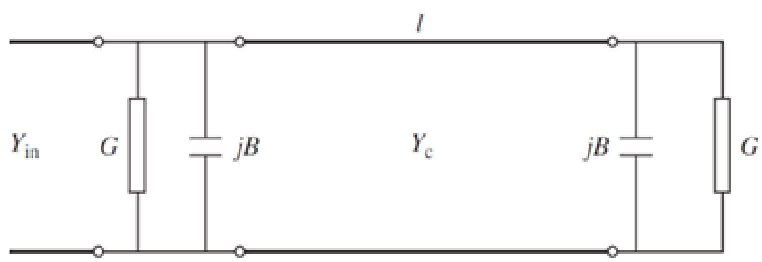

Figure 3-3: Equivalent circuit of a microstrip patch element [21].

3.2.2.2 Multimode Cavity Model

The microstrip antenna can be modeled as an open cavity surrounded by the patch, and its ground plane and the opened edges can be modeled by radiating magnetic walls. Such a cavity will support multiple discreet modes, much like a totally contained metallic cavity. For example, for a rectangular or square patch with substrate thickness h, relative dielectric constant ε_r, and patch dimensions L × W (see Figure 3-2), the total electric field in the cavity can be expressed as the sum of the fields associated with each sinusoidal mode [21]:

$$E_z(x,y) = \sum_m \sum_n C_{mn} \ . \ \cos(\frac{m\pi}{L})\ x \ . \ \cos(\frac{n\pi}{w})\ y \tag{3.1}$$

Where the feed position, L and W dimensions, and the dielectric constant all affect the constant C_{mn}. The fields are considered to be z-directed solely, with no variation in the z-direction, due to the extremely thin substrate assumption. The TM10 dominant mode, which might be attained if the dimension L is around λ_g /2 (λ_g is the effective wavelength in the dielectric), is the most interesting dominant mode. The field variation beneath the patch for this fundamental mode is shown in Figure 3-4, and the radiating fringing fields are illustrated in Figure 3-5(a). According to these figures, underneath the patch, along the central line orthogonal to the resonant direction (x-direction), there is a null field region. Because of this, it is possible to add more feed probes or shorting pins along this central line without affecting how well the patch of the original feed works. This is also the reason why dual-linear polarisation can be achieved with two feed probes that are orthogonally positioned without significant crosstalk. Due to their oscillating character, the left- and right-edge fringing fields in Figure 3-5(a) do not contribute much to the far fields and cancel one another out. The primary contributors to the far-field radiation of a patch are the top and bottom-edge fringing fields. Two equivalent slots in Figure 3-2 help to clarify this better

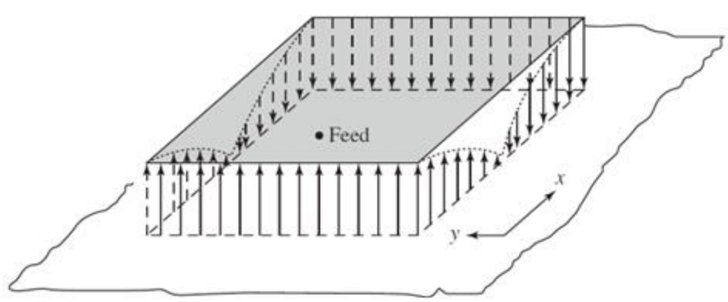

Figure 3-4: Fundamental-mode electric-field configuration underneath a rectangular patch [21].

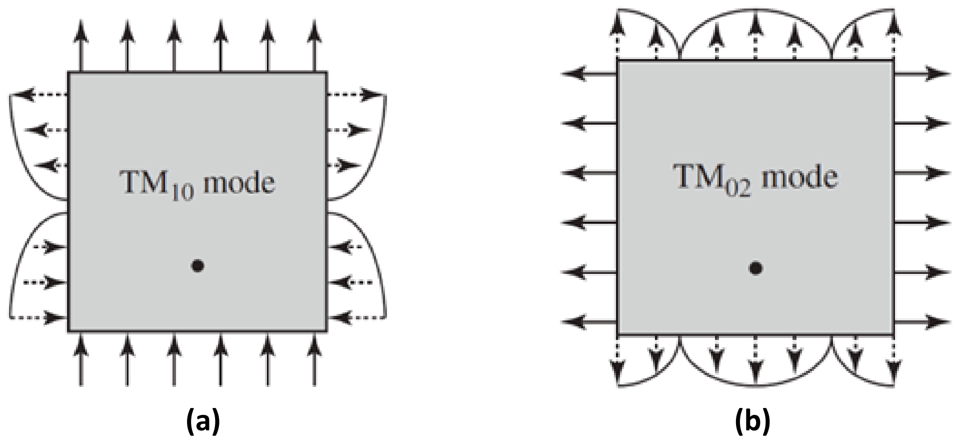

Figure 3-5: Fringing fields for fundamental-mode TM10 and higher order mode TM02 [21].

Therefore, the fundamental radiating mechanism of a patch (rectangular or circular) consists of two radiating slots separated by approximately λ/2. The TM02 mode is the secondary higher-order mode that contributes significantly to the cross-polarization radiation. This mode, illustrated in Figure 3-5(b), has the left and right edges contributing to the far-field radiation, but its magnitude is lower than the TM10 mode. One should be aware that, as shown in Figure 3-6, the left and right edge fringing fields only provide cross-polarization radiation in the H-plane pattern, whereas the top and bottom edge fringing fields contribute to co-polarization radiation in both the E and H-planes. In the E-plane, fringing fields on the left- and right-edge always cancel each other (note the arrow directions of the fringing fields). By considering the total fields at the edges of the patch from all modes, one can determine the equivalent edge magnetic currents and then integrate them to find the whole far-field radiation patterns. The input impedance can be determined by knowing the total radiated power and the input power. The cavity model technique allows the designer to determine the mode structure below the patch. Accordingly, it gives good physical insight, such as its resonating and cross-polarization behaviors. Nevertheless, because it assumes the field has no variation in the z-direction, its solution is not very accurate, especially when the patch antenna has a thick substrate. The calculation of mutual coupling between patches in an array of patch antennas is tedious and inaccurate.

3.2.3 Design Methodology

Thanks to technological advancement, nowadays, CAD tools can analyze an antenna design and provide calculated performance results for a design. However, the initial antenna design is necessary; in fact, it originated from human experience, knowledge, and innovation. Figure 3-7 shows a typical microstrip antenna development process.

The “Computer Analysis Software” block illustrates the central processing unit into which a human must enter the proper design data to initiate the design process. The block labeled “Antenna Design Techniques” represents the knowledge for introducing a set of initial input design data, which is the main subject of this section. The first step toward designing a microstrip array is element design.

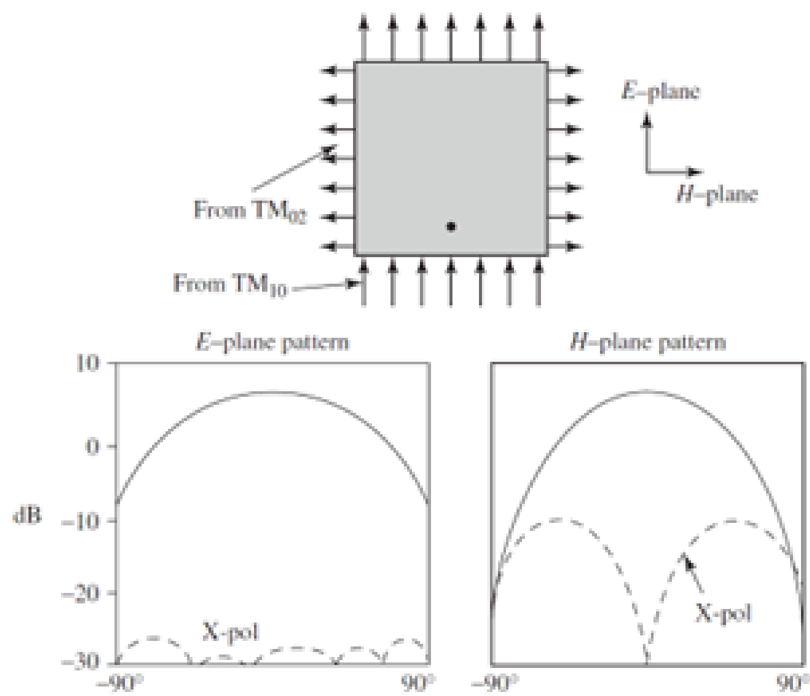

Figure 3-6: Basic E- and H-plane pattern shapes from a rectangular patch [21].

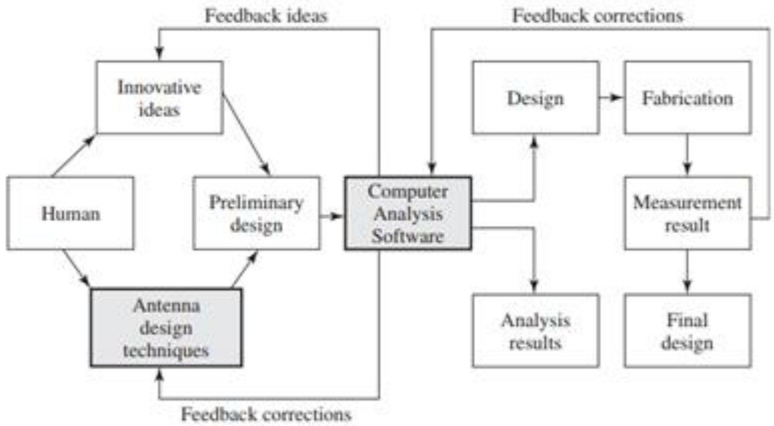

Figure 3-7: Microstrip antenna development procedures [21].

3.2.3.1 Patch Element Design

Patch elements can be a rectangular, square, circular, annular ring, triangular, pentagonal, or square or circular with perturbed truncations, among other configurations. These varied forms can often be employed to satisfy various demanding needs. For example, a rectangular patch utilized in linearly polarized applications can achieve a somewhat broader bandwidth than a square or circular patch. In order to achieve circular polarization, square and circular patches which can be excited orthogonally by two feeds are the best choices. Furthermore, the circular patch can be designed to excite higher-order modes for generating different-shaped patterns. On the other hand, square and circular patches are more vulnerable to cross-polarization excitation when used as linearly polarized elements compared to rectangular patches. Indeed, owing to their identical two orthogonal dimensions, the excitation of the orthogonal resonance (cross polarization) from the spurious coupling or feed asymmetry is easier. When simplicity and low insertion loss are required, the pentagonal patch and the square or circular patch with a small perturbation are suggested to generate circular polarization with only a single feed.

There is a simple closed-form equation to calculate patch sizes for the two most popular patch shapes, rectangular (or square) and circular [23]. These equations can generally achieve an accuracy of within 2%. For the fundamental mode rectangular patch, the simple equations are given by

$$f = \frac{c}{2(L+h)\sqrt{\varepsilon_e}} \tag{3.2}$$

Where:

$$\varepsilon_e = \frac{\varepsilon_r + 1}{2} + \frac{\varepsilon_r - 1}{2}(1 + \frac{12h}{w})^{-1/2} \tag{3.3}$$

c is the speed of the light, f is the resonance frequency, *h* is the substrate height, L is the patch resonant length, ε_r is the relative dielectric constant of the substrate, and *w* is the patch non-resonant width.

The simple design equation for the circular patch with TM_{mn} mode is given by:

$$f = \frac{\chi_{mm} c}{2\pi a_e \sqrt{\varepsilon_e}} \tag{3.4}$$

Where:

$$a_e = a\left\{1 + \frac{2h}{\pi a \varepsilon_r}\left[\ln(\frac{\pi a}{2h}) + 1.7726\right]\right\}^{1/2} \tag{3.5}$$

f, c, h, and ε_r are as defined for the rectangular patch design equation, a is the physical radius of the circular patch, χ_{mn} is the *m*th zero of the derivative of Bessel's function of order n, n is the angular mode number, and m represent the radial mode number [21].

3.2.4 Feed/Excitation Methods

Numerous methods exist for feeding a microstrip patch to radiate; a few popular ones are described and briefly explored in the following paragraphs.

3.2.4.1 Coaxial Probe Feed

A microstrip patch can be excited by a 50-ohm coaxial probe from behind the ground plane, as depicted in Figure 3-1. The outer conductor of the coaxial probe (flange) is soldered to the ground plane, and the center conductor pin penetrates through the substrate and the patch and is then soldered to the top of the patch. To achieve impedance matching, the location of the probe should be at a 50-ohm point of the patch. For various frequency ranges, there are different types of coaxial probes. UHF or low microwave frequencies type N, TNC, or BNC can be used for VHF. For microwave frequencies, SMA, 3.5 mm connector, OSM or OSSM can be used, and for the millimeter-wave frequency range k-connector (2.92mm), Mini-SMP(SMPM), 2.4 mm and 1.85mm connectors should be used.

3.2.4.2 Coaxial Probe with Capacitive Feed

A thicker substrate is typically utilized for applications requiring a broader bandwidth (5–15%). A greater inductance would be introduced if a normal coaxial probe were used, which would cause an impedance mismatch. In other words, the electrical field cannot abruptly change from the compact cylindrical space of the coaxial to the vast spacing of the patch. As a result, to cancel this inductance, capacitive reactance must be introduced. One strategy is to use a capacitive disk where the patch is not physically connected to the probe, as shown in Figure 3-8. Another strategy, as illustrated in Figure 3-9 is to use a "tear-drop" shaped or a cylindrical shaped probe [21].

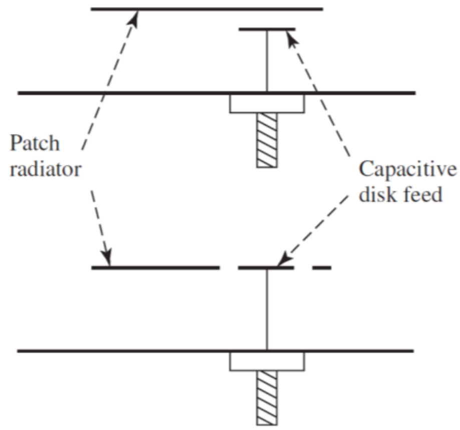

Figure 3-8: Two different capacitive feed methods for relatively thick substrates [21]

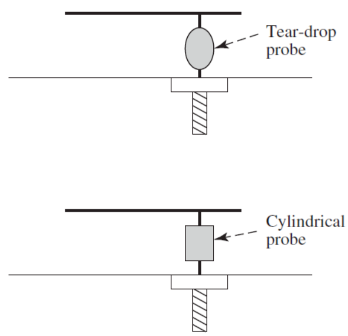

Figure 3-9: Tear-drop and cylindrical-shaped feed probes for relatively thick substrates [21].

3.2.4.3 Microstrip-Line Feed

A microstrip transmission line can be connected directly to a microstrip patch, as shown in Figure 3-1, and quarter-wavelength-long impedance transformers can be used to transform a large input impedance (at the edge of the patch) to a 50-ohm line. Because all patches and their microstrip power division lines in an array can be designed on the same substrate, fabrication cost per element can significantly decrease. However, the large leakage radiation of the transmission lines may lead to a rise in the side lobe or cross-polarization levels.

3.2.4.4 Proximity-Coupled Microstrip Line Feed

Through proximity coupling, a patch radiator can be fed via an open-ended microstrip line. As seen in Figure 3-10, the open-end of a 100-ohm line, for instance, can be positioned just beneath the patch at its 100-ohm location. In this method, a soldering connection does not need, which in some cases could achieve better mechanical reliability [21]. The proximity coupling method is easy to model and has low spurious radiation. However, its fabrication is more complicated. In order to control the matching, the length of the feeding stub and the width-to-line ratio of the patch can be used [15].

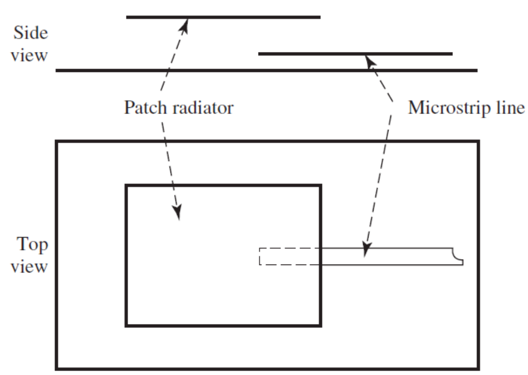

Figure 3-10: Non-contact proximity feed from underneath the patch [21].

3.2.4.5 Aperture-Coupled Feed

The aperture coupling consists of two substrates and a ground plane between them. There is a microstrip or stripline transmission line on the lower substrate's bottom side, and energy is coupled to the patch through a slot on the ground plane separating the two substrates. As shown in Figure 3-11, this technique can be used to avoid a soldering connection. In addition, this feed method allows using a high dielectric material for the bottom substrate and thick low dielectric constant material for the top substrate. The ground plane separating two substrates isolate the feed from the radiating element. Indeed, it avoids leakage radiation of the lines that interferes with the patch radiation and polarization purity, and it shields the antenna from spurious feed radiation. Generally, matching is performed by adjusting the feed line's width and the slot's length. Suppose the slot is centered under the patch. In that case, the magnetic coupling will dominate and also leads to a good polarization purity and no cross-polarized radiation in the principal planes because in this location, ideally for the dominant mode, the electrical field is zero while the magnetic field is maximum. Furthermore, a large bandwidth (more than 10%) can be achieved by this feed method. This extra bandwidth, compared to coax probe feed, results from a coupling slot, which is a resonator and a radiator. A wider bandwidth is achieved when two resonators (slot and patch) have slightly different sizes.

In fact, a slot length greater than half the patch width is necessary to attain sufficient coupling when thick antenna substrates are used for wide bandwidths. An aperture that is well below resonant size causes the limiting of the level of back radiation to about -20 dB relative to the main lob. However, it can only have about 5% bandwidth because the small coupling aperture limits the antenna substrate thickness. A bandwidth of 20 % to 25% can be achieved by making use of a thick antenna substrate with a low dielectric constant. But owing to the thick antenna substrate, a larger slot size is required to get the necessary coupling to impedance match the antenna, which results in a high level of back radiation [24].

The reduction of passive intermodulation distortion owing to other harmonic frequencies caused by non-linear devices present in the circuit is another advantage of proximity-coupled and aperture-coupled feeds.

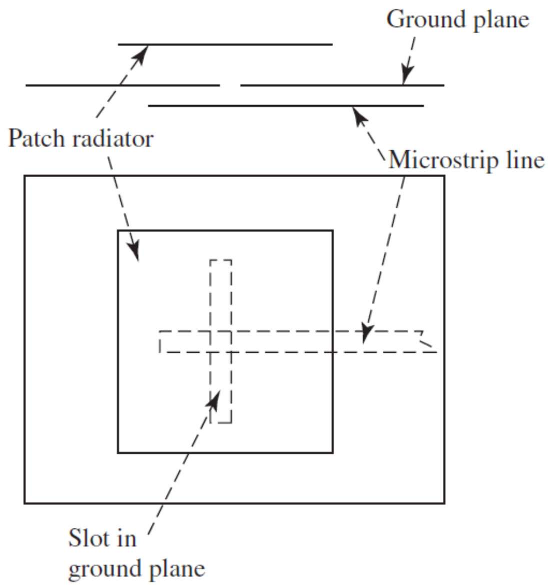

Figure 3-11: Patch fed by aperture-coupling slot [116].

The features offered by the ACMPA are especially useful for millimeter-wave phased arrays [25]. At these frequencies, classical feeding techniques such as microstrip line feed (edge feed) cause several problems because the size of the feed line can be comparable to the size of the patch. Accordingly, the antenna's performance can be significantly degraded, as well as microstrip line feed providing very little room for the feed network and associated devices. These considerations are much more critical in the wideband application, which requires a thicker substrate [26].

The aperture-coupled patch with a centered feed has no cross-polarization in the principal planes [20]. The geometry of an aperture-coupled patch antenna offers many degrees of freedom. In what follows, the basic trends when varying the different parameters are summarized [27].

- ***antenna substrate dielectric constant***: This parameter mainly affects the bandwidth and radiation efficiency of the antenna, and according to the broadband techniques described in 2.6, a lower permittivity results in a broader bandwidth and less surface wave excitation.

- ***antenna substrate thickness:*** Substrate thickness influences the coupling level in an ACMPA. A thicker substrate offers more extensive bandwidth but less coupling from a given aperture size.
- ***Microstrip patch length:*** The length of the patch affects the resonant frequency of the antenna.
- ***Microstrip patch width:*** The width of the patch determines the resonant resistance of the antenna, the wider patch, the lower resistance. If dual or circular polarization is not needed, square patches should be avoided since they may generate high cross polarization.
- ***Feed substrate dielectric constant:*** Good microstrip circuit characteristics should be considered; a substrate with a dielectric constant normally between 2 and 10 should be selected.
- ***Feed substrate thickness:*** Thinner microstrip substrates produce less spurious radiation from feed lines, but the loss is larger. Typically, a compromise between 0.01 and 0.02 l is a good one.
- ***Slot length:*** The coupling slot's length largely influences the coupling level and the back radiation level. Therefore, the slot shouldn't be any bigger than what's needed for impedance matching considerations.
- ***Slot width:*** The coupling level is influenced by slot width, although to a considerably lesser extent than slot length. Typically, the slot length-to-width ratio is 1/10.
- ***Feed line width:*** The width of the feed line impacts the coupling to the slot in addition to regulating the characteristic impedance of the feed line. Thinner feed lines, to a certain extent, couple more firmly to the slot.

- ***Feed line position relative to slot:*** The feed line should be positioned at a right angle to the slot's center for optimal coupling. Both skewing the feed line away from the slot and putting it closer to its edge can lessen the coupling.
- ***Position of the patch relative to the slot:*** The patch should be centered over the slot for best coupling. Moving the patch in the H-plane direction with respect to the slot has insignificant impact but moving it in the E-plane (resonant) direction will reduce the coupling level.
- ***Length of tuning stub:*** The tuning stub is used to tune the excess reactance of the slot coupled antenna. The stub usually is slightly shorter than $\lambda g/4$; reducing the stub will cause the impedance locus on the Smith chart to migrate in the capacitive direction.

3.2.5 Broadband Techniques in Microstrip Antenna

As we discussed, the microstrip antenna can be modeled as a resonating cavity with open side walls. Because a closed cavity with fixed dimensions behaves as a narrow band device, the microstrip antenna usually offers narrow bandwidth behavior. Figure 3-12 shows a bandwidth versus frequency plot for a typical rectangular patch with two relative dielectric constants (2.33 and 9.8) and various substrate thicknesses. According to this figure, a single patch with nominal substrate thickness has a bandwidth of 5%. However, owing to the patch's open side walls, the bandwidth of this open side cavity can be increased mainly if the thickness of this cavity is increased.

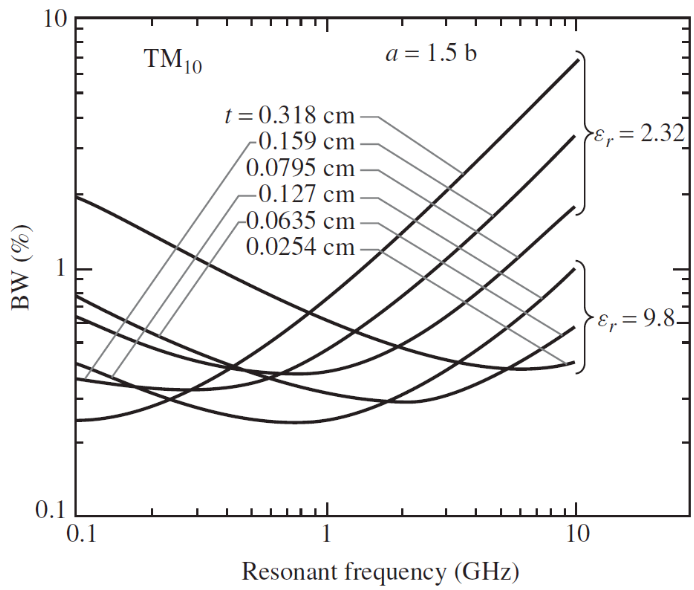

Figure 3-12: Bandwidths of rectangular microstrip patches with various substrate thicknesses and two dielectric constants [21].

To clarify further, consider a rectangular patch with x, y, and z dimensions, with x being the resonating dimension and z the cavity thickness. According to Figure 3-13, Figure 3-2, and Figure 3-4 the fringing field's height increased with increasing the cavity thickness. The L2-L1 is greater for the thicker substrate than the shallow one, and we can see from the figures that the degree of freedom for the resonance frequency to change is proportional to L2-L1.

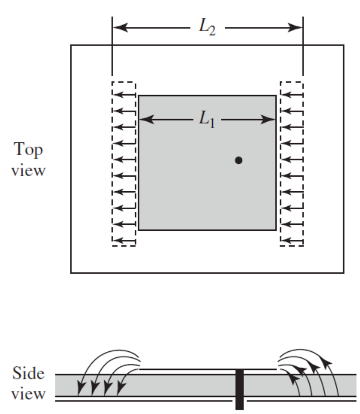

Figure 3-13: Primary fringing fields of a rectangular patch [21].

This increased bandwidth can also be explained by the antenna quality factor (Q), which is inversely proportional to the cavity thickness (h).

$$Q = \frac{C\sqrt{\varepsilon_e}}{4 f_r h} \tag{3.6}$$

Q : *Antenna quality factor*
C : *The speed of light*
f_r : *Resonance frequency*
h : *The cavity thickness*

And the bandwidth (BW) increases as Q reduces.

$$BW \approx \frac{f_r}{Q} \approx \frac{4 f_r^2 h}{C\sqrt{\varepsilon_e}} \tag{3.7}$$

From the (3.6), and (3.7) a larger bandwidth for a microstrip antenna is possible by increasing the substrate thickness and lowering the dielectric constant value. However, by enlarging the thickness, the feed line or feed probe will face an impedance matching issue. Indeed, a more significant reactance (inductance) is introduced by the feed. In the case of a feed probe, one can use a capacitive feed to cancel this excessive inductance, as discussed in 3.2.4.2. In the case of microstrip line feed, an impedance-matching circuit can be used to decrease this large reactance.

As the substrate becomes thinner, the current on the patch element is placed in very close proximity to its negative image caused by the presence of the ground plane, and it substantially cancels radiated fields. This provides additional information on the increase in the bandwidth when increasing substrate thickness. Accordingly, a relatively large amount of energy is stored below the patch. Figure 3-12 illustrates that the bandwidth improves by increasing the substrate thickness and decreasing the substrate's permittivity. On the other hand, a thin substrate with a high dielectric constant operates best for microstrip transmission lines and microwave circuits. Therefore, a tradeoff between high antenna performance and good circuit performance should be taken into account in order to combine a microstrip antenna with a feed network and circuitry on the same substrate. A limitation to increasing the substrate thickness is the loss caused by surface wave excitation. Generally, losses in the microstrip antenna result in three ways: conductor loss, dielectric loss, and surface wave excitation. Conductor and dielectric loss are small, and they cause a few percent loss in radiation efficiency except for extremely thin substrates. The surface wave which can be excited by the antenna are bound to the dielectric substrate, and it does not contribute to the primary radiation pattern of the antenna; surface wave power is considered a loss mechanism in general. However, surface wave power can also diffract from discontinuities, the same as substrate edges, and may degrade the antenna radiation pattern or polarization characteristics. In a single element, surface wave power increases with substrate thickness and dielectric constant. This is another reason why a substrate with a low dielectric constant is preferable. In large arrays of microstrip antennas, destructive interference of surface wave power causes the raising of radiation efficiency. However, constructive interference may be possible in a phased array microstrip antenna at certain scan angles. This behavior leads to a scan blindness effect. Besides the mentioned inherent antenna element losses, the impact of losses due to feed lines and related feed circuitry can be considered as well, which can be the dominating loss contribution in a large array [20].

It should be considered that there is a limitation to increasing the bandwidth by enlarging the substrate thickness. The maximum feasible bandwidth is around 15% with a thickness of 0.15 free space wavelength. In other words, the field will not cohere efficiently between the patch and the ground plane with increased substrate thickness. However, one can use different techniques to improve the bandwidth [21]. Techniques to increase the bandwidth take one of two routes typically

[28]: either adding a matching element, such as matching stubs in the microstrip antenna feed line [29]-[30], or increasing the number of resonating elements, such as parasitic elements or slots, like U-shaped slots, in the radiating patch, which has close resonant frequencies [22], [31], [11], [29].

A U-shaped slot may significantly increase an antenna's bandwidth by increasing the number of resonant frequencies. As a result, broadband, multi-band, and band-notch operations have made substantial use of the probe feed U-slot microstrip antenna [28]. Considerable experimental and simulation results on the U-slot patch are presented in [22],[32]. According to [22], the U-slot patch on a foam substrate of about 0.08 λ thickness can be designed to attain 20-30% gain in bandwidth. The general geometry of a probe-feed U-slot microstrip antenna is shown in Figure 3-14.

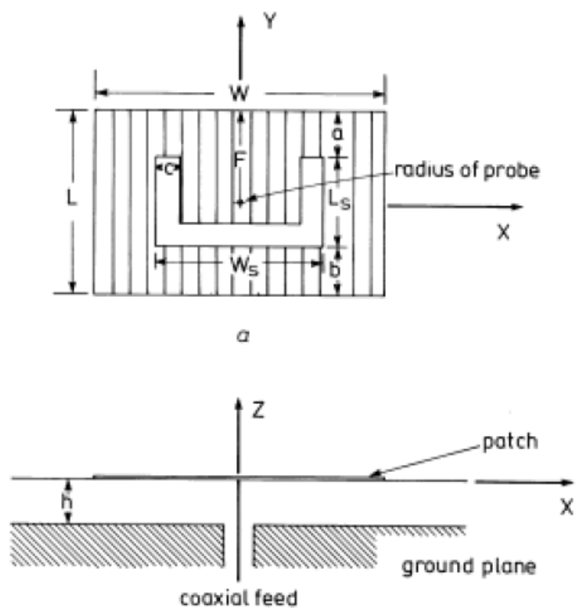

Figure 3-14: Geometry of coaxially fed rectangular patch with a U-shaped slot [22]

In [28], a probe-feed microstrip antenna on a foam substrate uses a single U-shaped slot to achieve 32.7% bandwidth. In this case, two different but close resonant frequencies in a single patch give a wideband operation. The microstrip patch generates the first, and the second is by the U-shaped slot. It should be taken into account that although the U-slot enhances bandwidth and gain, the cross-polarization (X-pole) level also rises, and the antenna's primary beam somewhat deviates due to structural asymmetry. Thus, to widen the bandwidth, some broadband techniques can be combined to develop a more efficient method [28]. The U-shaped slot and various stubs on Rogers duroid 5880 substrates were utilized by a 16 by 16-element antenna array in [29] to increase the bandwidth to 17% in the Ku band. The embedded microstrip feed layer feeds the U-slotted antennas by proximity coupling.

Reference [11] introduces a compact LTCC patch antenna, shown in Figure 3-15, that uses stacked parasitic strips (SPSs). The LTCC substrate is Ferro A6-M ($\varepsilon_r = 5.7, \tan\delta = 0.003$), and this configuration can both produce a wide bandwidth by employing adjacent resonance and yield a high gain owing to its director effect. In brief, the purpose of the parasitic elements is to modify the radiation pattern emitted by the driven elements, directing them in one direction and increasing the antenna's gain. Indeed, a parasitic element acts as a passive resonator. It absorbs the radio wave from the nearby driven element and re-radiates them with various phases again. The waves from the different antenna elements interfere coherently, strengthening the antenna radiation in the desired direction as well as canceling out the wave in an undesired direction. Directors in a Yagi antenna and a parasitic microstrip patch antenna are well-known examples of parasitic elements. For short, the main effect of a parasitic microstrip patch antenna is to increase the impedance bandwidth of the antenna significantly.

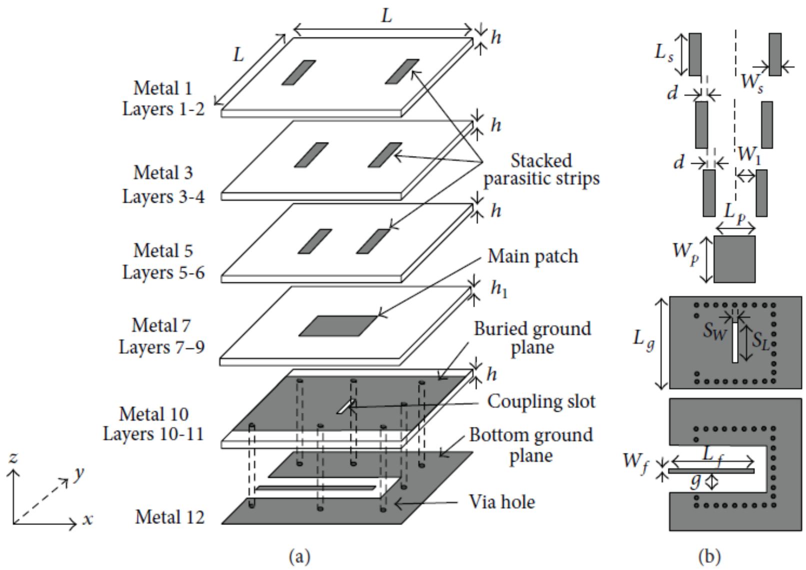

Figure 3-15: Configuration of the proposed antenna. (a) Expanded view. (b) Metal layer details [11]

The design of a broadband U-slot patch antenna fed by a new proximity-coupled double π-shaped feed line is presented in [33]. This technique is an improvement upon a π-shaped feed line. A large array element spacing is required for proximity coupling and slotted patches with a U-shaped feed line to design a broadband proximity coupled U-slot patch antenna, which results in undesirable grating lobes. In [33], by modifying the π-shaped feed line to a double π-shaped feed line, compact array spacing was achieved with maintaining a broad bandwidth (21.5% around 9.5 GHz) and low profile. The antenna substrates are comprised of Duroid 5880 ($h = 31\ mils, \varepsilon_r = 2.2$), separated by foam with a thickness of 1.5 mm. The U-slot patch with a π-shaped feed structure is shown in Figure 3-16(a), and the U-slot patch with doubled π-shaped feed for a single element is illustrated Figure 3-16 (b-e).

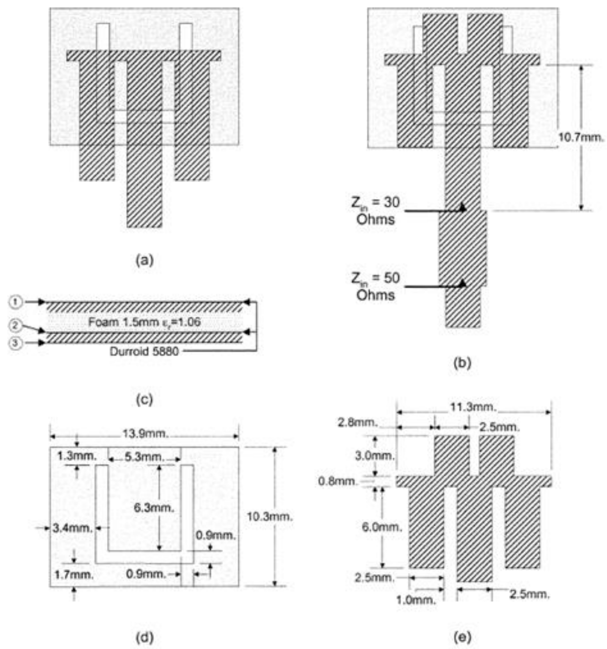

Figure 3-16: (a) U-slot patch with ∏-shaped feed structure. (b) U-slot patch with doubled ∏-shaped feed structure. (c) substrate layout for antennas with single and doubled ∏ feeds (d) U-slot patch dimensions (e) doubled ∏-shaped feed dimensions [33].

Reference [34] describes a microstrip antenna that increases bandwidth by using a resonant aperture and stacked patches. The geometry of this aperture-stacked patch (ASP) microstrip antenna is shown in Figure 3-17. This ASP microstrip antenna has a larger aperture and thicker substrates than a typical aperture-coupled stacked patch. The main reason behind this structure is using the aperture as a resonator, not as a mechanism for coupling the patches to the microstrip feed line. By this method, bandwidth from 50 to 70% has been realized. [34] has compared this ASP microstrip antenna with two other aperture-coupled microstrip antennas. In all three examples, the antenna substrates were made of foam ($\varepsilon_r = 1.07$). The first is an aperture-coupled microstrip antenna with a thick foam substrate and a near-resonant aperture. A 1.5:1 VSWR bandwidth of 21% is achieved, and because of using one patch, it has a simple structure, the level of back radiation that results from using a large aperture is low, and the front-to-back ratio is better than 12 dB over the band. The second is a typical aperture-coupled stacked patch design with 20% bandwidth. The front-to-back ratio is increased to more than 18 dB over the band.

As previously mentioned, the main design comprises a resonant aperture with stack patches resulting in a 1.5:1 VSWR bandwidth of 44%. But because of the increase in substrate thickness and aperture size, it has produced higher back radiation levels with a front-to-back ratio of better than 10 dB over the band. It should be taken into account; this type of wideband performance is generally much more difficult to obtain if using a substrate with higher permittivity. Because the aperture is used as a radiator in the aperture-stacked patch microstrip antenna, its size cannot be changed to independently control the coupling to the microstrip feedline.

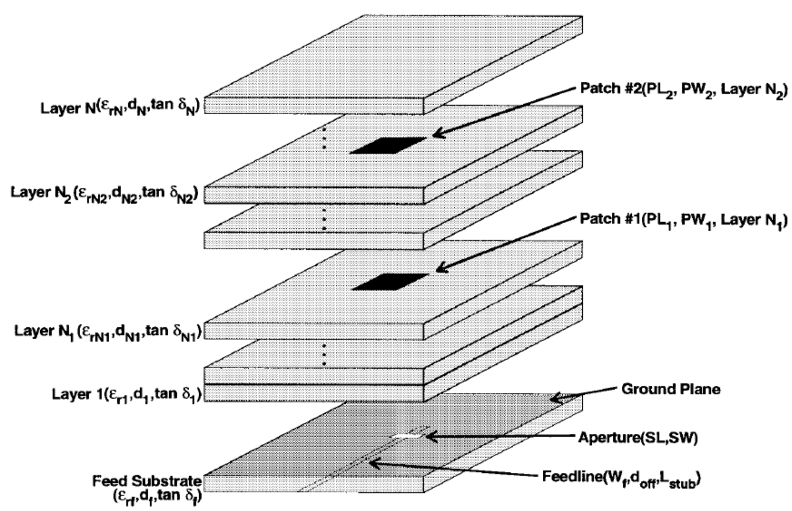

Figure 3-17: geometry of multilayered ASP antenna [34].

In [12] also has been presented three designs on the "zero shrinkage" type of LTCC foil ESL Electro Science 41110-T ($\varepsilon_r = 4.05, \tan\delta = 0.0015$) to achieve a wideband antenna. The first design is a one-layer rectangular patch radiator with a microstrip feed line connected to the wide side. Because of low substrate thickness, the bandwidth is limited to 4.9% around 120 GHz and 8 dBi gain. The substrate thickness has been increased in the second design to enlarge the bandwidth. However, a dielectric-filled cavity was used to avoid substrate thickness more than 0.1λ and surface wave excitation, as shown in Figure 3-18. The cavity is terminated at the bottom with metal layer 1 and at all sides with lines of vias located $100\mu m$ from the opening perimeter of the cavity. This design has improved the bandwidth from 4.9% to 10% with a maximum gain of 8dBi. In this design, because part of the microstrip feed line lies over the cavity, that part's characteristic impedance is increased by 77Ω, and this simple feeding line geometry antenna can only be matched in a limited frequency range. Therefore, to enhance the bandwidth, the feeding circuit's geometry must be improved. A two-step transition from $140\mu m$-microstrip feed line to $314\mu m$-microstrip feed line, shown in Figure 3-19, has been chosen, leading to bandwidth improvement from 10% to 12.5%.

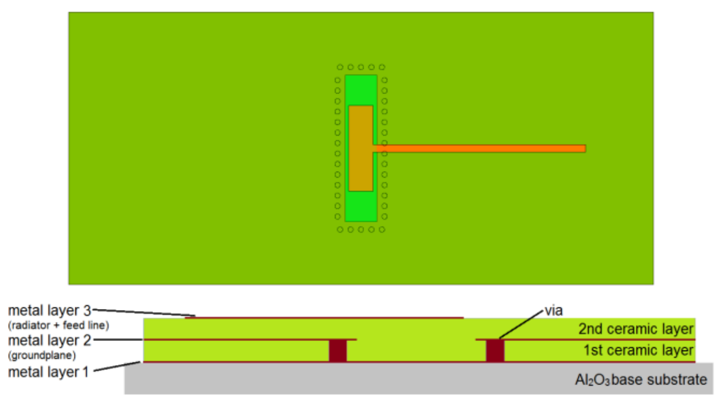

Figure 3-18: Two substrate layer patch antenna (top view and longitudinal section) [12]

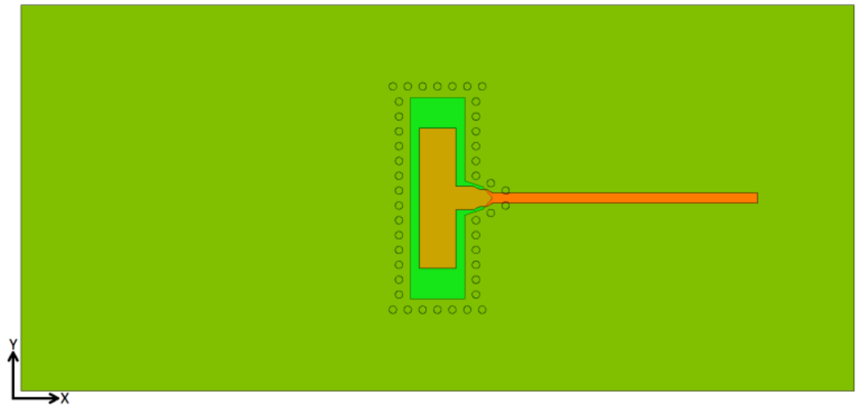

Figure 3-19: Two substrate layer patch antenna with improved microstrip transition [12].

An inverted feeding arrangement in [35], which presents for supporting both Personal Communication Service and International Mobile Telecommunications, has 19.84% and 28.25% bandwidth at each port. This antenna has a ground plane with a cross slot between the upper and lower feeding line and was extended to a 2x4 array, shown in Figure 3-20, for both applications. According to [36], two orthogonal modes can be excited by a cross-shaped slot feed by two symmetric feed lines. As shown in Figure 3-20, one inverted feeding line is over the ground plane, and the other is under the ground plane. The slotted ground plane blocks the coupling between the two feeding lines and has caused appropriate isolation. Furthermore, to enhance the bandwidth. A 15mm air gap between the patch and the upper feeding line, as shown in Figure 3-21, was used. The permittivity of other substrates is 2.5 as well. Port1 has a bandwidth of 390 MHz around 1.85 GHz (19.84%), and port two has a bandwidth of 550 MHz around 1.95 GHz (28.23%), and the gain of the designed 2×4 array antenna is measured as 16.5dB.

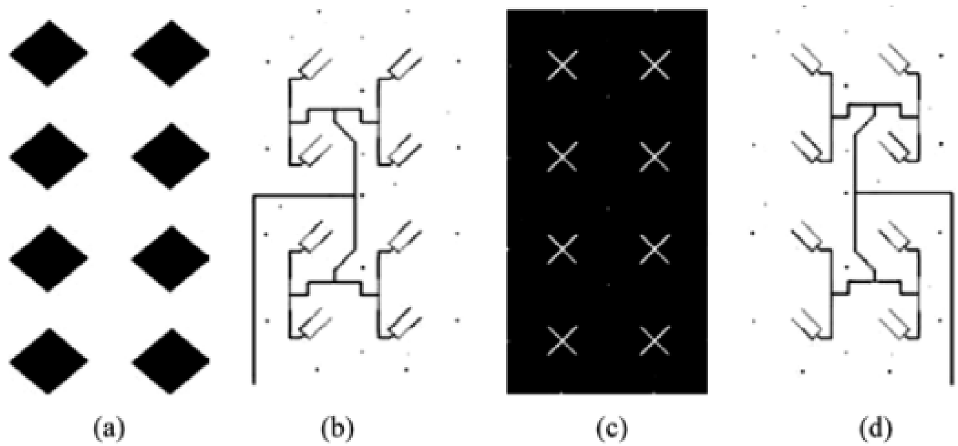

Figure 3-20: Layout of the designed antenna. (a) Patch, (b) inverted feeding line. (c) crossed slot, (d) normal feeding line [35].

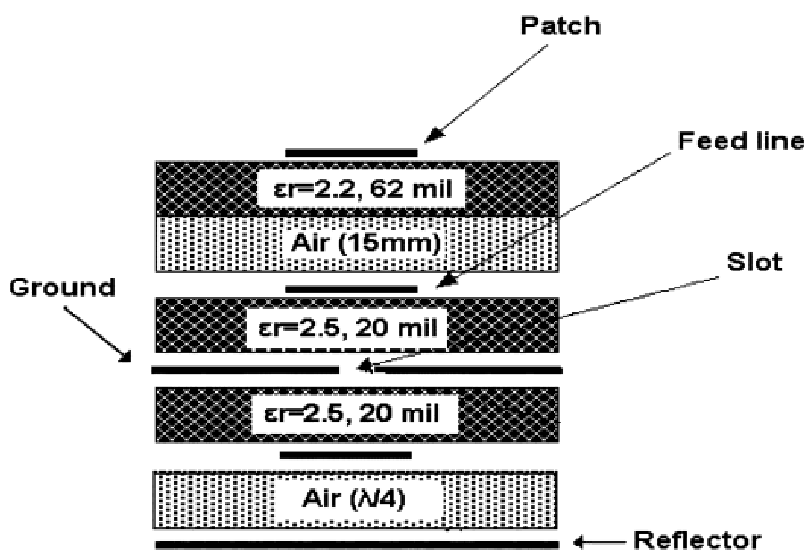

Figure 3-21: Side view of the designed antenna [35].

3.2.6 Cavity Backed Patch Antenna

Due to the high dielectric constant, ε_r, of some substrates like LTCC substrate, a standard patch antenna would be a very narrow band. Although a stacked patch antenna can improve the bandwidth, this bandwidth is still limited by the substrate dielectric constant. If an embedded air cavity was created between the parasitic patch and the main patch to reduce the effective dielectric constant, a higher bandwidth could be attained [37].

Furthermore, at mm-wave frequencies (30-300 GHz), surface waves are excited along the substrate because the substrate is usually electrically thick and comparable to the wavelength. According to section 2.11, the surface wave power is proportional to permittivity and substrate thickness, and the radiation pattern becomes distorted as it radiates from the borders of the finite ground plane. The radiation efficiency and gain also decrease as the surface wave power increases. Low permittivity substrates are preferred to increase the radiation efficiency, gain, and bandwidth. In this regard, processing an air cavity inside the substrate leads to decreasing the effective dielectric constant of the substrate, suppressing the surface waves and mutual coupling inside the dielectric substrate. According to [38], a cavity acts as a heatsink in a high-powered large transmit array. Moreover, air cavities, by reducing the mutual coupling and improving matching over wider scan angles, can prevent scan blindness in a phased array antenna. The optimum air cavity size compromises between building a cavity large enough to not electrically affect the antenna performance and building the smallest cavity to prevent sagging problems[39].

In [37], an embedded air cavity in the LTCC substrate is used to achieve a wideband in a stacked patch antenna. This design achieves a gain of better than 5 dBi over an 18% bandwidth. A 2×2 element array of stacked patch antenna with a maximum gain of 11.1 dBi and 3-dB gain bandwidth from 25 to 30 GHz is also realized in [37]; see Figure 3-22.

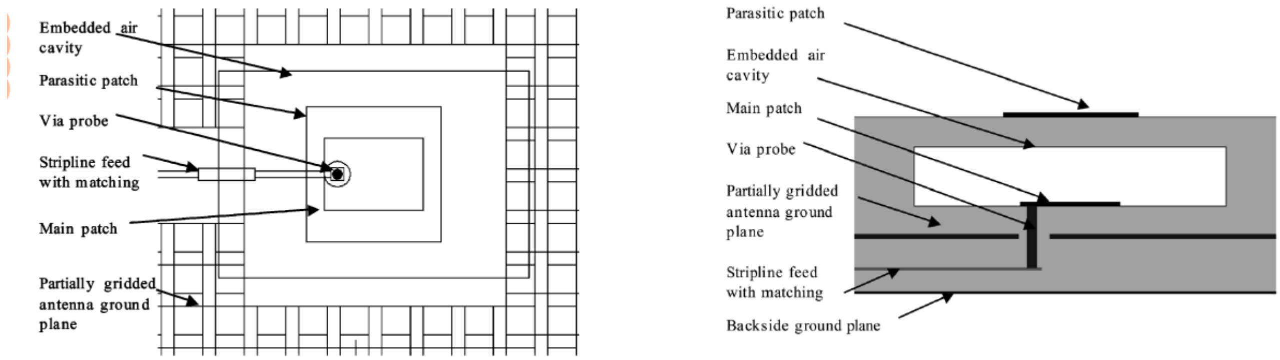

(a) *(b)*

Figure 3-22: (a): Top view of a single LTCC stacked patch antenna showing an embedded air cavity. (b): Side view of a single LTCC stacked patch antenna showing an embedded air cavity [37]

Reference [38] presented an ACMPA and its 4×4 planar array on LTCC in the 60-GHz frequency band. In this design, an air cavity processed inside the LTCC substrate was used to enhance the gain and bandwidth of the antenna. The measured S-parameters show 3.7% impedance bandwidth improvement and 2.5 dBi gain improvement compared to the ACMP without an embedded air cavity with 5.8% impedance bandwidth and 15.7dBi gain. For implementing the array, because, at 60 GHz, separate cavities cannot be processed for each array element separately, one large cavity was used in the array. This design was processed using the Ferro A6-S LTCC tape system with the dielectric constant and loss tangent of $\varepsilon_r = 5.99$ and $\tan\delta = 0.0015$, respectively. The single optimized ACMP with a cavity is shown in Figure 3-23. The $200-\mu m$ thick superstrate above the radiator focuses the electromagnetic field upward.

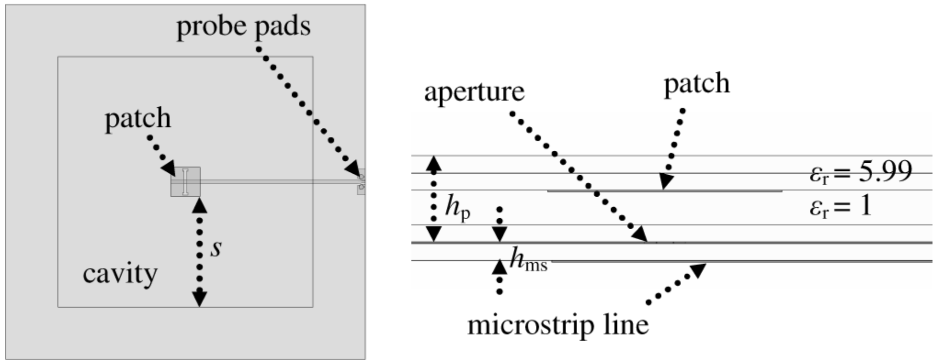

Figure 3-23: ACMP antenna with cavity [38].

Reference [40] introduced an aperture microstrip antenna for 10 GHz on an LTCC system with an embedded air cavity, as shown in Figure 3-24. In this design, an air cavity with a height of 0.5 mm was processed at the bottom of the upper substrate. The results of the fabricated antenna with an embedded air cavity were compared with a similar antenna without an air cavity. The measured bandwidth for the antenna with and without cavity was 6.8% and 3.2%, respectively. As well as the measured gain at the center frequency of the cavity and non-cavity antenna was 5.4 dBi and 3.2 dBi.

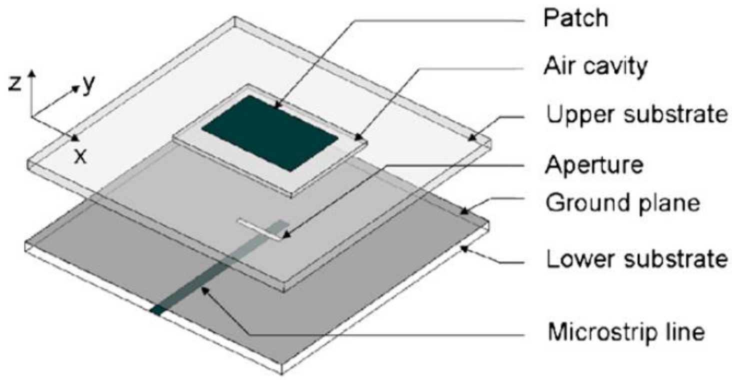

Figure 3-24: Aperture coupled microstrip with an embedded air cavity [40].

3.2.7 LTCC Patch Antennas

The antennas encounter difficulties in terms of material choice, manufacturing tolerance, and measuring methods at high working frequencies, including mm-wave bands. In particular, the losses caused by materials, fabrication tolerance, connection, and so on become much more critical than the designs at lower microwave bands [19].

The conventional PCB process is inadequate for the manufacture of mm-wave antennas due to increased dielectric loss and reduced fabrication tolerance. Therefore, the interest in fabricating mm-wave antennas using the LTCC system is rising. The LTCC process, in addition to lower substrate loss and higher fabrication tolerance, also enjoys flexibility in realizing an arbitrary number of layers and ease of integration with circuit components through stacked vias and cavity-buried components, as mentioned in previous parts. Furthermore, the reliable and flexible fabrication process offers much more design freedom, especially implementing cross-layer vias and open and embedded cavities in mm-wave antenna and circuit design compared to the conventional PCB process. Numerous mm-wave antenna designs have been created using LTCC during the 2000s, especially at operating frequencies around and over 60 GHz. Although almost any type of antenna, including slot antennas, Yagi antennas, and linear tapered slot antennas, may be made using LTCC technology [19], planar antennas like microstrip patches are an excellent option since the conductor layers in LTCC are screen-printed. In what follows, I will explore a literature review on microstrip patch antennas in the LTCC system.

Reference [41] compared apertures coupled microstrip antenna on LTCC Dupont 9V7K and Rogers 5880 at 60 GHz, the design on LTCC has shown better performance. The 4×4 array antenna realized in LTCC has achieved a maximum gain of 16.3 dBi and impedance bandwidth of 9%. In comparison, the Rogers substrate array has achieved a bandwidth of 4% with a gain of 14.5 dBi. The geometry of the single-element LTCC and Rogers multilayer antenna is presented in Figure 3-25.

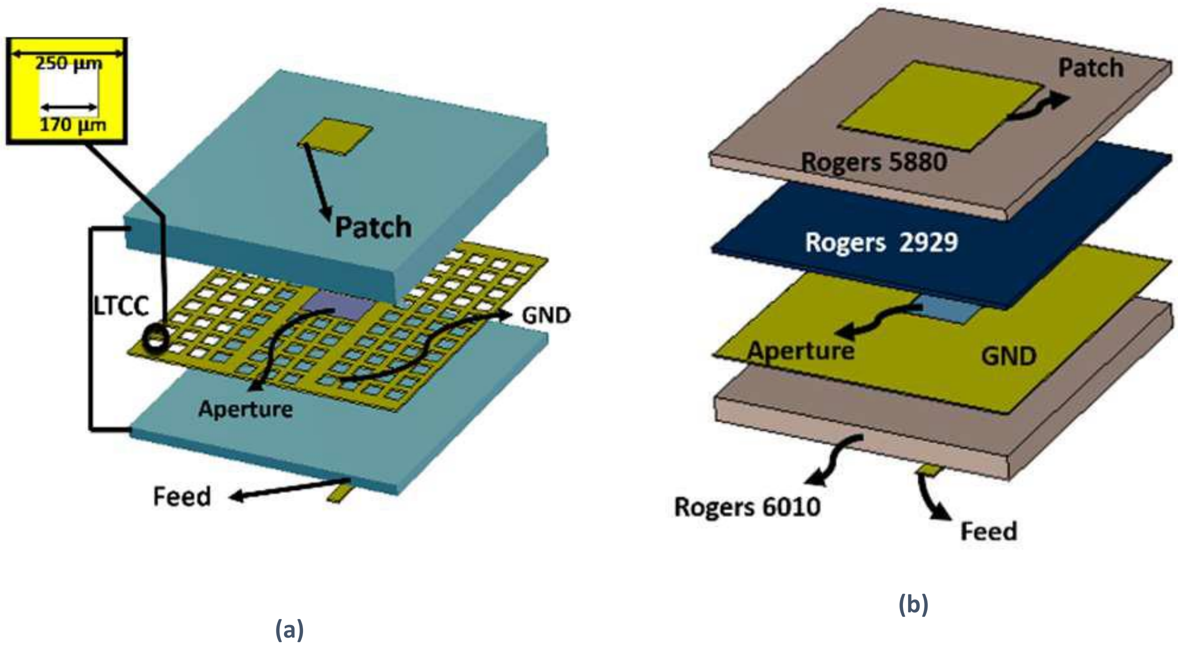

Figure 3-25: (a) Geometry of the proposed LTCC multi-layer antenna. (b) Geometry of the proposed Rogers multi-layer antenna [41].

In [42], an LTCC-based stacked and meshed patch antenna for space application has been proposed, as shown in Figure 3-26. Twelve Dupont Green Tape 9K7 LTCC substrate layers with a dielectric constant of $\varepsilon_r = 7.1$ and loss tangent of $\tan\delta = 0.0010$ have been used for the design. This reference studied different mesh configurations of stacked meshed patch antennas and different types of patches. Various types of patches were made by adding circular and rectangular slots or corner chamfer in meshed patches. Its simulation results confirmed that the stacked mesh performance, considering the resonant frequency, gain, return loss, and radiation efficiency, can be comparable to that of a typical, continuous metal stacked design, and the measurement results showed that it has a 1.5% impedance bandwidth with a maximum gain of -0.12 dBi and cross-polarization of 10 dB at boresight.

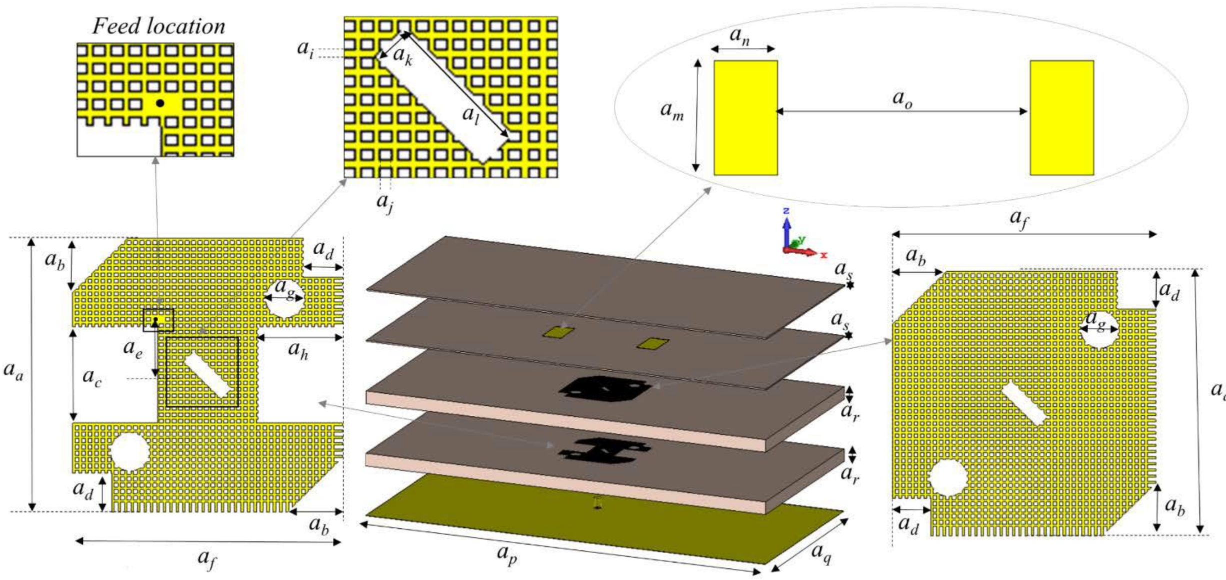

Figure 3-26: Meshed stacked LTCC antenna configuration [42]

In [37], an embedded air cavity in LTCC is used to achieve a wideband response with a stacked patch antenna, shown in Figure 3-22. In this design a gain of better than 5 dBi over an 18% bandwidth with a good impedance match is achieved. A 2×2 element array of stacked patch antenna with a maximum gain of 11.1 dBi and a 3-dB gain bandwidth from 25 to 30 GHz is also realized in [37]. Reference [11] introduces a compact LTCC patch antenna, shown in Figure 3-15, that make use of stacked parasitic strips (SPSs). The LTCC substrate is Ferro A6-M ($\varepsilon_r = 5.7, \tan\delta = 0.003$), and this configuration can produce a wide bandwidth by employing adjacent resonance and yield a high gain owing to its director effects.

In [12] also has been presented three designs on the “zero shrinkage” type of LTCC foil ESL Electro Science 41110-T ($\varepsilon_r = 4.05, \tan\delta = 0.0015$) to achieve a wideband antenna. The first design is a one-layer rectangular patch radiator, with a microstrip feed line connected to the wide side. Because of using a low substrate thickness, the bandwidth is limited to 4.9%, around 120 GHz and 8 dBi gain. The substrate thickness has been increased in the second design to enlarge the bandwidth. However, to avoid substrate thickness more than 0.1λ and surface wave excitation, the dielectric-filled cavity was used as shown in Figure 3-18. The cavity is terminated at the bottom with metal layer one and all sides with lines of vias located from the opening perimeter of the cavity. This design has improved the bandwidth from 4.9% to 10% with a maximum gain 8 dBi. In this design, due to fact that the microstrip feed line lies over the cavity, its characteristic impedance is increased to about 77Ω, consequently, this simple feeding line geometry antenna can only be matched in a limited frequency range. Therefore, to enhance the bandwidth, the geometry of the feeding circuit has to be improved. A two-step transition from $140\mu m$-microstrip feed line to $314\mu m$-microstrip feed line, shown in Figure 3-19, has been chosen, leading to bandwidth improvement from 10% to 12.5%.

3.3 Transition in LTCC System

The low-loss properties and relatively large dielectric constant of LTCC materials have made it a suitable choice for integrating antennas and other millimeter-wave circuits on multilayer substrate's structure. This ceramic technology is made of stacked layers of thin, flexible ceramic tapes to which metalized vias and conductive traces can be applied one layer at a time with a moderate-cost screen-printing technique before staking, dicing, and co-firing the final circuit [12]. Within the multilayer LTCC planar structure, stripline (SL) represent a favorable choice of buried transmission lines because of the good electromagnetic (EM) isolation they provide between adjacent layers [43], [44]. However, for the connection between the inner layers and the output terminals, standard coaxial connectors are usually preferred. Thus, developing special transitions to route the signal from the inner stripline layers to the outer layers using stacked vertical via holes is required. There are various types of transmission-line transitions in LTCC structures, transferring the signal from stripline to outer layers. A broadband LTCC transition from edge-launched coaxial connector to stripline is presented in [45]. It, as shown in Figure 3-27, it uses a complex structure, including a cavity fabricated using 8- layers of Dupont 9K7 LTCC tape; it demonstrated good performance up to 67 GHz.

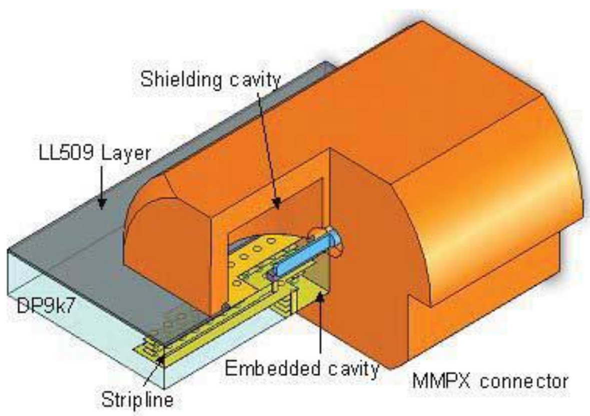

Figure 3-27: Cross section of transition from coaxial connector to stripline [45].

The work in [44] provides a stripline-to-microstrip transition with Dupont 951 LTCC tape, as illustrated in Figure 3-28. Simulation results showed a return loss of better than 17 dB up to 70 GHz.

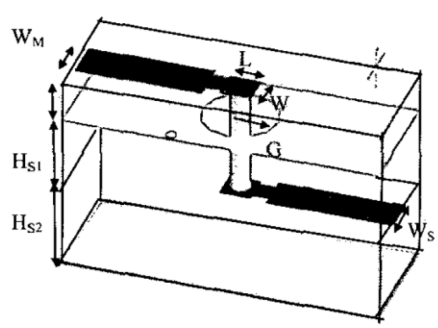

Figure 3-28: The geometry of transition from microstrip to stripline [44]

Reference [46] presents a GCPW-to-stripline vertical transition for K-band applications illustrated in Figure 3-29. It was designed and fabricated on a 12-layers LTCC substrate Ferro A6M tape system, and its measurement results showed a return loss better than 10 dB and an insertion loss less than 2 dB from 6 GHz to 28.4 GHz for a total length of 12mm.

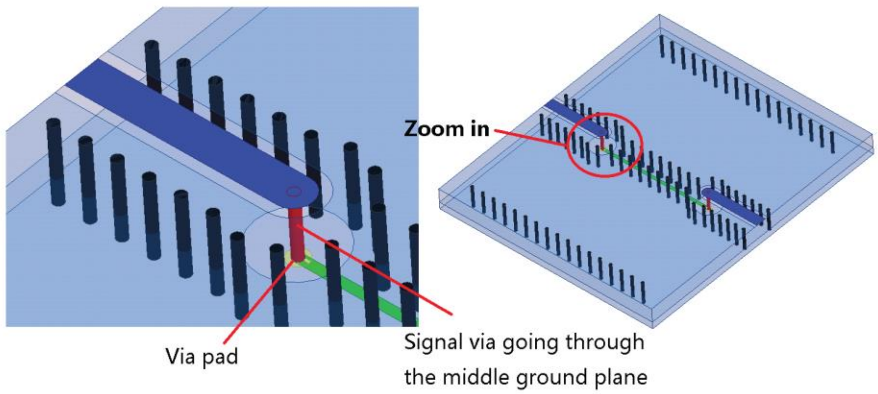

Figure 3-29: Configuration of a GCPW to Stripline vertical transition [46].

Reference [47] proposed two CPW-to-stripline vertical transition structures with an additional ground plane for GCPW, as shown in Figure 3-30. Authors in [47] used a method to reduce the inductive effect of the vertical transition at high frequencies. The structure was designed on an LTCC substrate of Ferro A6M, consisting of 6 tapes, and its measured return loss was above 10 dB from 5 GHz to 45 GHz.

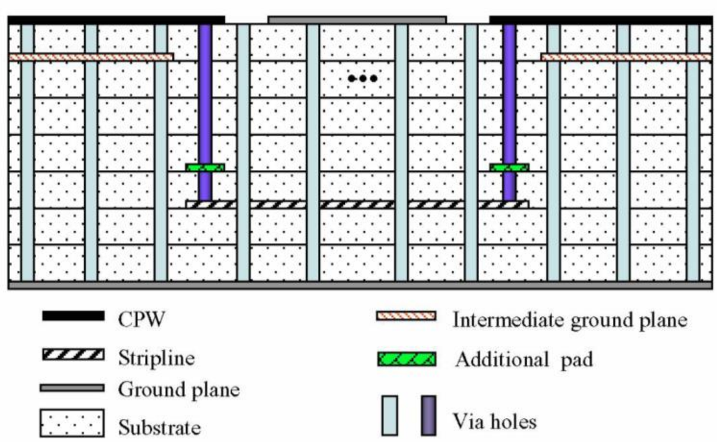

Figure 3-30: Configuration of a CPW to stripline vertical transition [47].

A novel transition between differential stripline (DSL) and differential grounded coplanar (DGCPW) is presented in [48], see Figure 3-31. This proposed structure was designed on the LTCC, showing low insertion loss and reflection up to 60 GHz by full-wave simulation.

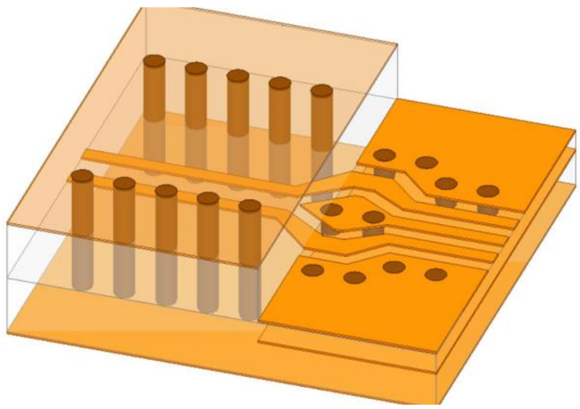

Figure 3-31: DSL-to-DGCPW transition [48].

3.4 Conclusion

This chapter presents a comprehensive review of the works in the area of wideband cavity-backed patch antennas in LTCC technology. First, the characteristics of MSP antennas, their design methodology, and various feed methods in MSP antennas are discussed. Then, different techniques to broaden the bandwidth in MSP antennas are reviewed. Cavity-backed and LTCC patch antennas are then briefly reviewed in the literatures. Finally, different transitions in LTCC technology are reviewed.

Chapter Four: SMPM coaxial connector to LTCC Stripline transition

4.1 Introduction

The low-loss properties and relatively large dielectric constant of Low-Temperature Co-fired Ceramic (LTCC) materials have made it a suitable choice for integrating antennas and other millimeter-wave circuits on single substrates. This ceramic technology is made of stacked layers of thin, flexible ceramic tapes to which metalized vias and conductive traces can be applied one layer at a time with a moderate-cost screen-printing technique before staking, dicing, and co-firing the final circuit [12].

Within the multilayer LTCC planar structure, stripline (SL) represent a favorable choice of buried transmission lines because of the good electromagnetic (EM) isolation they provide between adjacent layers [43],[44]. However, for the connection between the inner layers and the output terminals, standard coaxial connectors are usually preferred. Thus, developing special transitions to route the signal from the inner stripline layers to the outer layers using stacked vertical via holes is required.

This chapter presents the study and design of a mini-SMP (SMPM) connector-to-stripline transition for a multi-layer active phased array antenna for 5G applications. The connector is a Surface-Mount Device (SMD) and is suitable for system-on-package (SOP) applications. Because of the specific structure of the chosen SMPM connector, particular patterns in the top and middle ground layers were created to keep the approximate impedance of the transmission line close to 50 Ω. This work is the first to propose a wideband transition from coaxial to stripline with a SMPM connector in literature. The transition structure was designed and fabricated with 5-layer LTCC Dupont 9K7 tape and demonstrated good performance from 8 GHz to 34 GHz.

4.2 Design of The Transition

The SMPM coaxial connector to LTCC stripline transition investigated in this chapter is designed and implemented with DuPont's 9K7 LTCC technology. Gold metallization, with thickness of $8\mu m$ is used with two post-firing tape thicknesses of $112\mu m$, and $224\mu m$.

Figure 4-1(a) shows the proposed coaxial-to-stripline transition. It consists of two parts: the coaxial-to-coplanar waveguide (CPW) transition and the CPW-to-stripline transition. It is realized by an SMD connector (Figure 4-1(b)) and manufactured with five layers of Dupont 9K7 tape (4 tapes of $224\mu m$, and one tape of $112\mu m$) for multi-layer active phased array antenna for 5G applications. Apertures matching the SMPM structure are opened on the two top ground layers below the connector, and two catch pads in the vertical transition are used to adjust the capacitive and inductive characteristics of the transmission line to have a 50 Ω at the stripline end. The stripline is designed on three bottom layers of the LTCC substrate. The distances from the strip to the upper and lower stripline ground layers are $448\mu m$ and $112\mu m$, respectively, and the stripline length is 4.04mm, and the total length of the proposed transition is 10.3mm.

Moreover, gold filled via fencing by shorting all ground layers give rise to field confinement in the stripline structure, and it prevents higher order modes and resonance between the four ground planes [45], [49]. According to the fabrication process design rule check (DRC), the post-fired diameter of each via hole is fixed and equal to $136\mu m$. Figure 4-2(a) shows the expanded view of the proposed transition. For brevity, vias are not depicted, and their locations and heights can be realized from the holes shown on each layer. The details of each metal layer are depicted in Figure

4-2(b). The final optimized dimensions of the proposed transition are presented in Table 4-1 and all the descriptions of the design parameters in Table 4-1 are labeled in Figure 4-2(a), and Figure 4-2(b) accordingly.

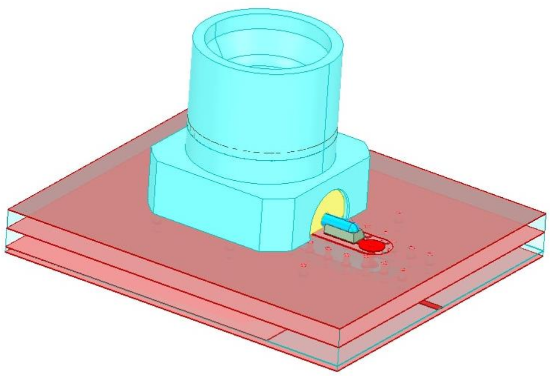

(a)

(b)

Figure 4-1: Transition structure (a) SMPM coaxial connector to LTCC stripline transition. (b) SMPM connector bottom view.

The Sub-Miniature-Push on Micro (SMPM) connectors have micro-miniature interfaces with a frequency range of DC to 65 GHz. These connectors are usually used in miniaturized mm-wave band circuits. Compared to other connector types in the mm-wave band, like 2.92mm (SMK) and 2.4mm, SMPM connectors have a smaller package size and have push-on and Snap-on mating styles suitable for quick installation. These connectors can also be used in a board-to-board interconnection using a floating bullet adapter. The floating bullet provides a link between mated pairs compensating for both radial and axial misalignment.

Considering the internal structure of the SMPM connector, shown in Figure 4-1(b), air and Teflon are used as dielectric in the SMPM connector. For the section in which air is the dielectric, the large permittivity difference between air and substrate (Dupont 9K7) causes a large capacitive discontinuity. Hence by creating an aperture on the uppermost metal layer (Top ground), almost the same as the existing aperture on the floor of the SMPM connector, shown in Figure 4-1(b), the distance from the connector's pin to the ground increases, and accordingly the capacitive discontinuity decreases. In the last section of the connector structure, Teflon is used as a dielectric. Because the dielectric constant in this part in comparison to the previous one has increased, hence by opening a rectangular aperture in the second ground below the connector (buried ground #1), the distance between the connector's pin and ground increased much more than the previous part. According to Equation 4.1, the characteristic impedance decreases to 50Ω at the stripline end. Therefore, the buried ground #1 and #2 are intermediate ground planes to improve the impedance matching in the transition structure.

$$Z_0 = \sqrt{\frac{L}{C}} \qquad (4.1)$$

L : Inductance of a transmission line per meter.

C : Capacitance of a transmission line per meter.

Z_0 : Characteristic impedance of a transmission line.

Furthermore, the space between the strip and the via fencing and the size of the circular openings in ground planes are optimized to improve the impedance matching by adjusting the capacitive characteristic of the transmission line. Additionally, according to [47], the vertical transition shows an inductive effect at higher frequencies; hence, to improve the RF performance of the proposed transition, the inductive effect is controlled via the addition of a capacitive counterpart. Thus, by placing additional catch pads in Top ground and buried ground#1 this compensation is achieved.

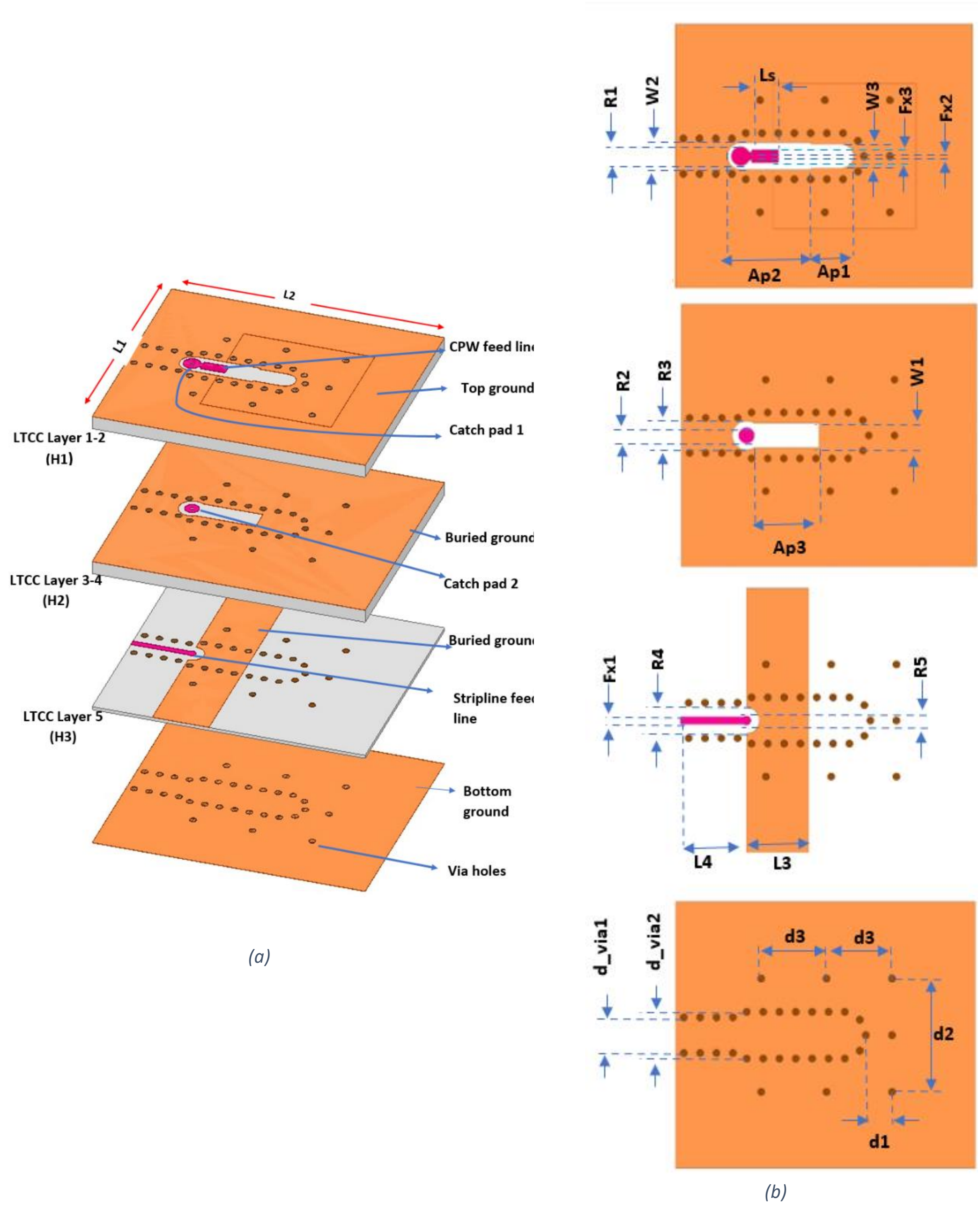

Figure 4-2: (a) Expanded view of the proposed coaxial-to-stripline transition (b) Metal layers details of the proposed transition.

Table 4-1: The final optimized dimensions of the proposed coaxial to stripline transition

Parameter	d_via1	d_via2	L1	L2	L3	L4	d1	d2	d3
Dimension (mm)	1.07	1.4	8	9.16	1.9	2.02	0.8	3.4	2
Parameter	Fx1	Fx2	R2	R3	R4	R5	w1	w2	w3
Dimension (μm)	214	223	475	890	796	270	746	846	726
Parameter	Fx3	R1	Ap1	Ap2	Ap3	H1	H2	H3	Ls
Dimension (mm)	0.4	0.569	1.32	2.56	2	0.448	0.448	0.112	0.825

4.3 Simulation Results

The SMPM coaxial connector to LTCC stripline transition was modeled, simulated, and optimized by Ansys Electromagnetic Suite 2022 R2. The simulation results for the proposed transition between 22 GHz to 34 GHz as shown in Figure 4-3, are almost less than -20 dB for reflection coefficients and around -0.3 dB for transmission coefficient.

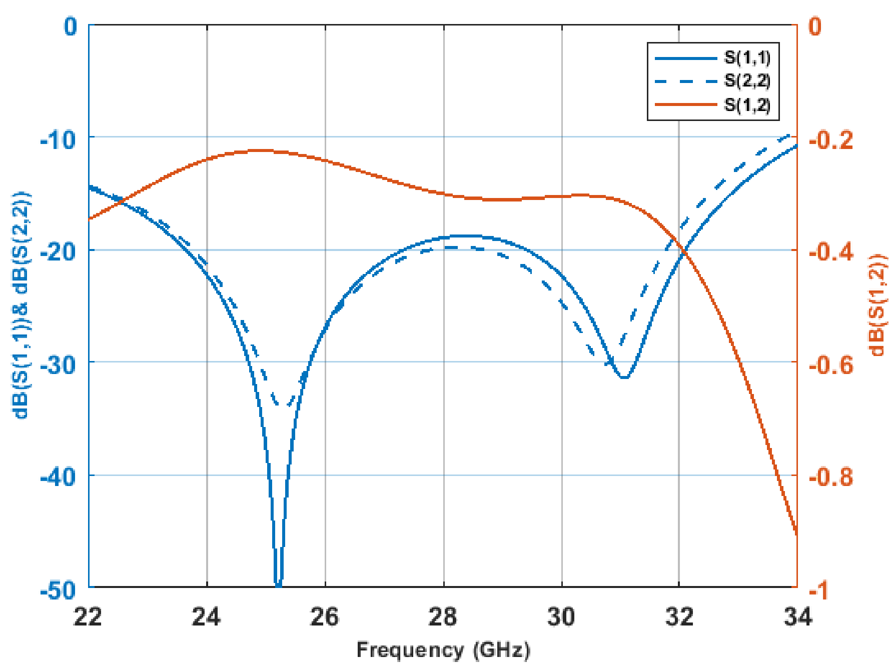

Figure 4-3: The S parameters of the transition between coaxial and strip line.

The back-to-back configuration was simulated to validate the design, as shown in Figure 4-4

Ground planes are partially gridded to prevent camber issues as well as delamination issues (i.e., the layers do not adhere correctly due to an excessive presence of conductive surface). The ground planes are solid along the CPW/Strip line feed, as well as directly below the connector, to better approximate a perfect ground plane. The rest of the ground plane area is made up of a 125 μm grid.

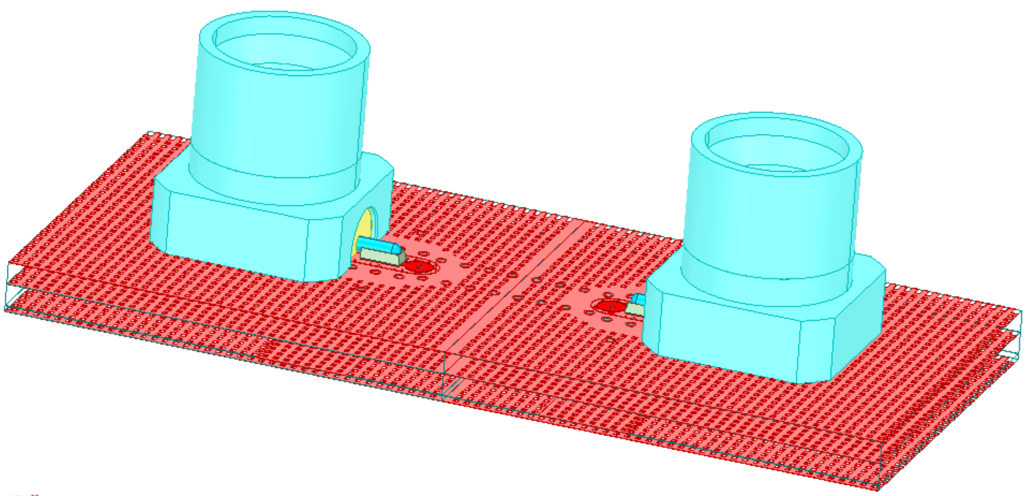

Figure 4-4: The geometry of the back-to-back configuration

Simulation results show that the return loss is better than 10 dB between 8-32 GHz and the insertion loss is around 1 dB from 9 GHz to 31 GHz. The simulated insertion loss of a simple stripline, as shown in Figure 4-5, with the same length and substrate parameters as the proposed transition but excluding vertical transitions and connectors, is found to be about 0.4 dB, as presented in Figure 4-6(b). In contrast, the proposed coaxial-to-stripline, including a vertical transition and SMPM connector, has a measured insertion loss of around 1 dB. This slight difference between a simple stripline and the proposed transition confirms the excellent performance of the proposed structure in mm-waves.

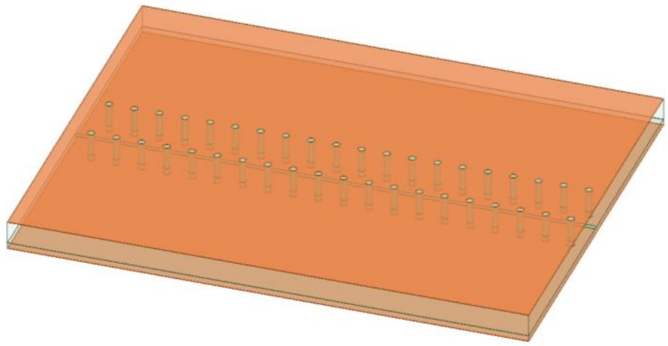

Figure 4-5: The geometry of a simple stripline

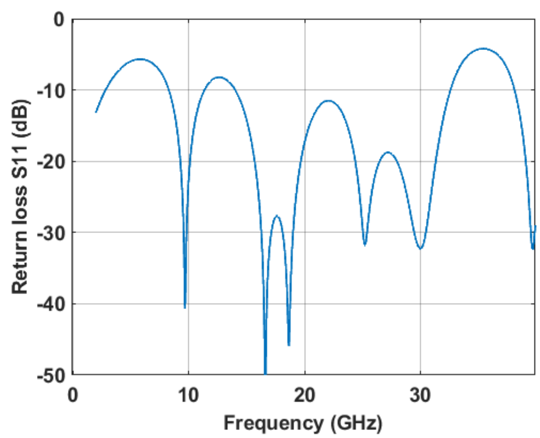

(a)

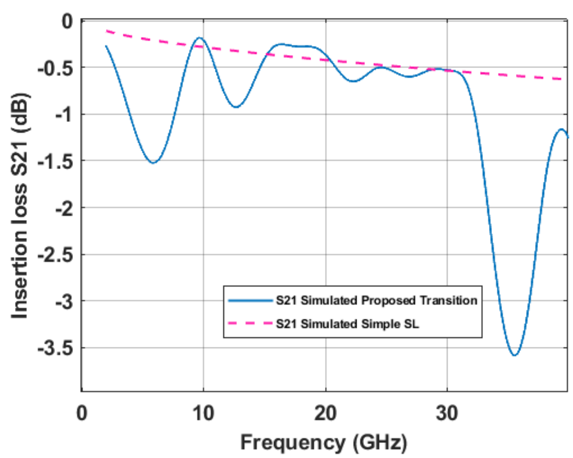

(b)

Figure 4-6: Simulated results of the back-to-back configuration (a) Return loss (b) Insertion loss

4.4 Conclusions

An SMPM coaxial connector to LTCC stripline transition is investigated in this chapter. Techniques used to enhance the bandwidth are elaborated, and then simulation results of the proposed transition are presented. Finally, a back-to-back configuration was also simulated and prototyped to validate the design, and its results are illustrated in detail.

Chapter Five: Design of Ka Band Patch Antenna in LTCC Technology

5.1 Introduction

With the exponential growth of mobile data demand, the fifth generation (5G) mobile network has emerged in recent years. Through the use of a large unlicensed frequency spectrum, 5G has improved communication capacity. The vast amount of unused spectrum in the mm-wave can support the higher data rates required in future mobile broadband access networks. For such significant data rates, a wide band system is required, and an aperture-coupled patch antenna offering large bandwidth, good cross-polarization, and efficiency as compared to conventional microstrip is an appropriate choice in this regard.

The features offered by the ACMPA are beneficial for the mm-Wave phased array [25]. At these frequencies, traditional feeding methods like microstrip line feed (edge feed) have several drawbacks, including performance degradation of the antenna due to the feed line being comparable to the patch size and a lack of adequate space for the feed network and related equipment. These considerations are much more critical in wideband applications, which requires a thicker substrate [50].

In mm-wave bands, the losses caused by materials, fabrication tolerance, measurement methodology of the antenna, become much more critical compared with the design at lower microwave bands. Accordingly, the interest in fabricating mm-wave antennas using LTCC is increasing. In addition to lower substrate loss and higher fabrication tolerance, the LTCC process also benefits from flexibility in realizing any number of layers and ease of integration with circuit components through stacked vias and cavity-buried components. Additionally, LTCC technology offers significantly more design freedom in mm-wave antenna and circuit design when compared to conventional PCB processes, especially when implementing cross-layer vias and open and embedded cavities.

5.2 Proposed Antenna Geometry

In this chapter, a new aperture-coupled patch antenna with high bandwidth mm-wave and stable radiation patterns at 28 GHz for 5G applications has been designed and implemented with Dupont's 9k7 LTCC technology, with a dielectric constant of 7.1. Gold metallization, with a thickness of $8\mu m$ is used with two post-firing tape thicknesses of $112\mu m$, and $224\mu m$.

The proposed wideband LTCC ACMPA was designed in 3 steps. At first, a single element was designed and simulated in the k and ka bands. Second, a transition between the SMPM Rosenberger connector to the LTCC strip line for these frequency ranges was designed (described in chapter 4). Finally, by connecting this designed transition to the single element in step one, the single element fed by the SMPM connector was ready. The antenna was modeled and optimized using HFSS.

5.2.1 Single Element

The proposed single-element antenna geometry without any connector is shown in Figure 5-1. Eight Dupont Green Tape 9K7 LTCC substrate layers with a dielectric constant of $\varepsilon_r = 7.1$ and loss tangent of $\tan\delta = 0.0010$ have been used for the design. The overall size of the single element antenna is 8×8×1.64 mm^3. Figure 5-2(a) shows the expanded view of the proposed antenna. Vias are not shown since it would be too wordy; instead, the via holes and catch pads can be used to determine where and how tall the vias are. The details for each metal layer are shown in Figure 5-2(b). The initial parameters can be obtained by using formulas presented in 3.2.3, along with the explanations about designing an aperture-coupled patch antenna in 3.2.4.5. The final optimized dimensions of the proposed antenna are presented in Table 5-1, and all the descriptions of the design parameters in Table 5-1 are labeled in Figure 5-2 accordingly.

The combination of several resonators, including stacked patches, embedded air cavity, and large size slot (near resonance), improved the bandwidth in such an LTCC structure with a high dielectric constant of 7.1.A stacked parasitic patch increases the impedance bandwidth by adding one adjacent resonance to the main resonance deduced from the main patch. Moreover, the parasitic patch, due to its director effect, improves the antenna's gain. In the proposed antenna, because the slot has a slightly different size from the parasitic patch, it acts like a resonator and increases the bandwidth. In fact, a slot length greater than half the patch width is necessary to attain sufficient coupling when thick antenna substrates are used for wide bandwidths, and using stripline feed, to some extent, can compensate a high back radiation resulting from the aperture. This should be taken into account because the aperture is used as a radiator in the proposed antenna; its size cannot be changed independently to control the coupling to the microstrip feed line. Furthermore, an embedded air cavity has been used for gain enhancement and for reducing the losses caused by the surface wave at mm-wave frequencies as results of decreasing the effective dielectric constant of the substrate underneath the patch antenna.

Stripline feed is used to feed the antenna, and vias connect its two ground planes to create a cavity effect for suppressing spurious parallel plate modes [11]. In the stripline feed with metallic vias connecting the two ground layers, parallel plate modes and parasitic modes resulting from the back radiation from the slot are suppressed. On the other hand, these vias create a cage around the strip and make it similar to a primary coaxial line.

In a conventional ACMP antenna, the currents, which return through the ground layer, create an excitation field in the slot. These currents in the stripline ACMP antenna are distributed over the two ground layers. According to [51] in the proposed antenna, by increasing the height of the lower substrate of the stripline (H5), as shown in Figure 5-2, currents become more concentrated on the upper ground layer, which improves the excitation field in the slot, and the structure tends toward that of the microstrip line.

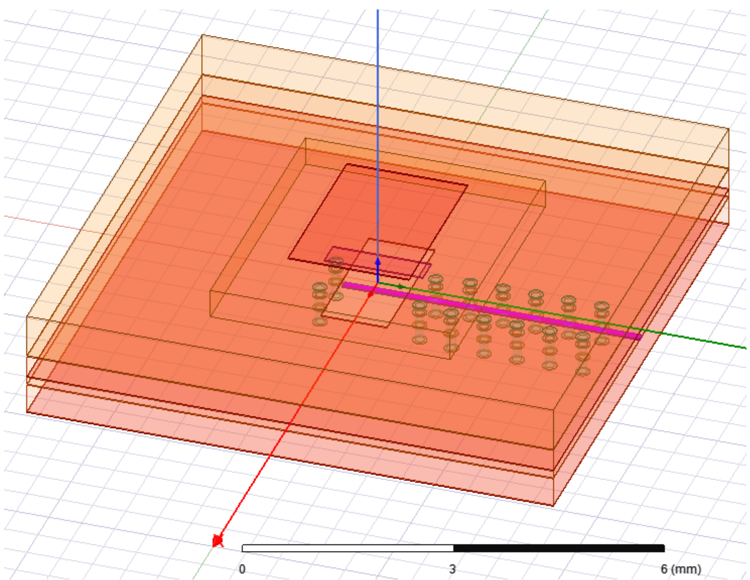

Figure 5-1: Simulated single element antenna

Table 5-1: The final optimized dimensions of the proposed Single antenna

Parameter	Y1	L	X2	Y2	L_slot	w_slot	X_cav	Y_cav	d_via1	Lf	Fx	d_v
Size (mm)	1.498	8	2.68	1.84	2.19	1	4.33	3.64	0.7314	0.523	0.125	0.5
Parameter	X1	M_w	ddd2	r_via	H1	H2	H3	H4	H5	th		
Size (µm)	386.2	186	333.97	68.175	224.03	2×224.03	112.01+ 224.03	112.01	2× 224.03	8		

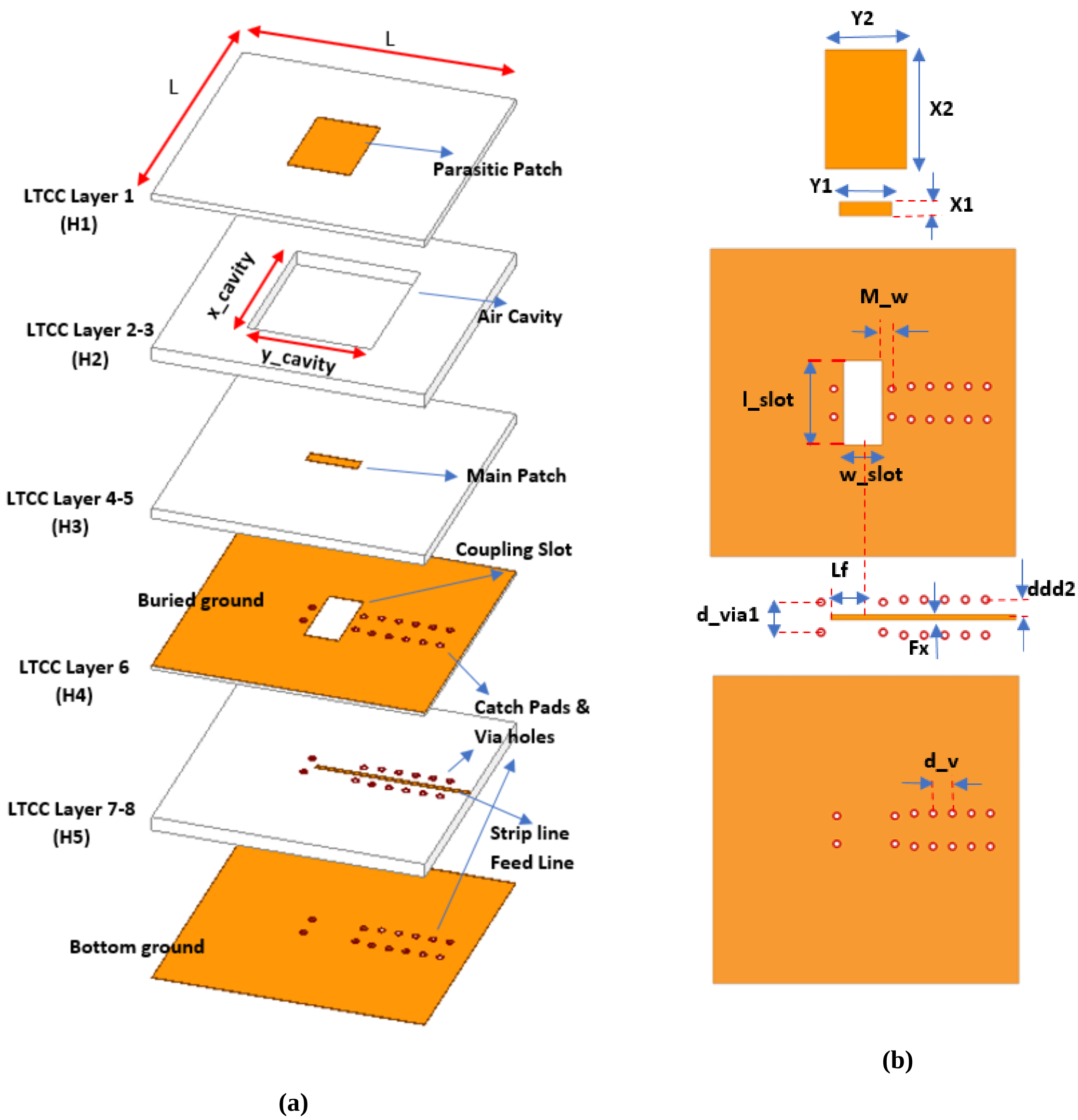

Figure 5-2: Configuration of the single element antenna. (a) Expanded view. (b) Metal layer details

The simulated return loss is shown in Figure 5-3, the 3D simulated radiation pattern for 28 GHz is depicted in Figure 5-4 as well as realized gain pattern for cut φ=0° and φ=90° for 25 to 32 GHz are shown inFigure 5-5. According to Figure 5-3, the single element antenna has 35.7% impedance bandwidth, and 6.05 dB realized gain at 28 GHz. According to Figure 5-5, maximum realized gain changes from 5.56 dB to 7.76 dB in 25 to 32 GHz.

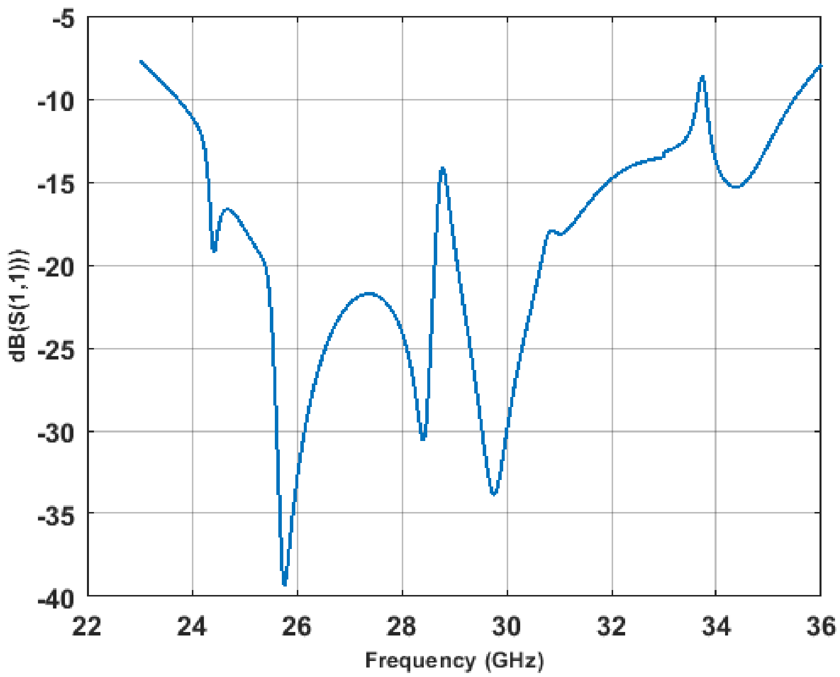

Figure 5-3: Simulated return loss of the proposed single element antenna.

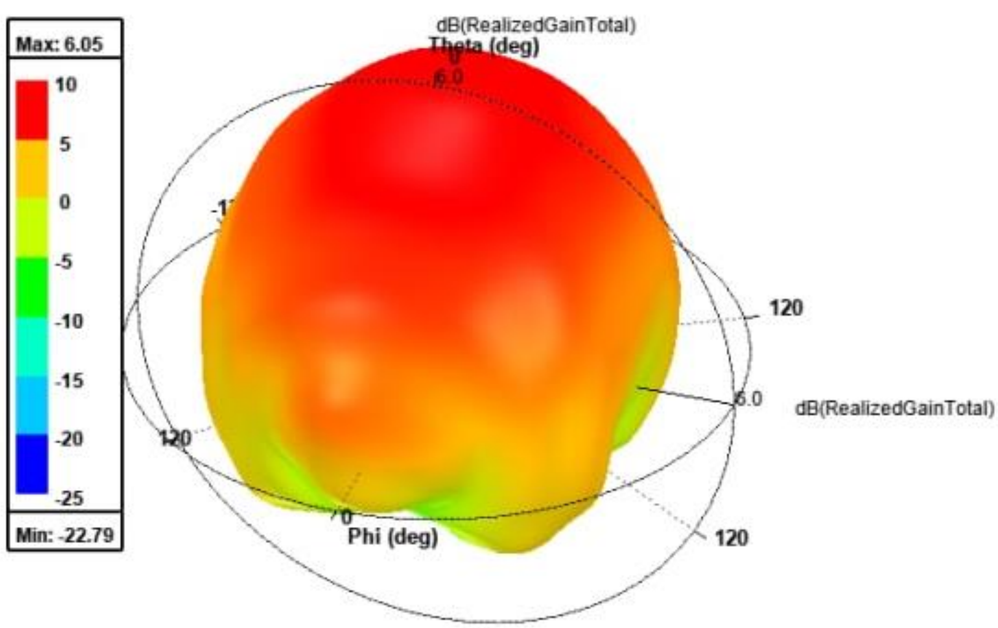

Figure 5-4: 3D realized gain pattern for the proposed single element antenna @ 28GHz

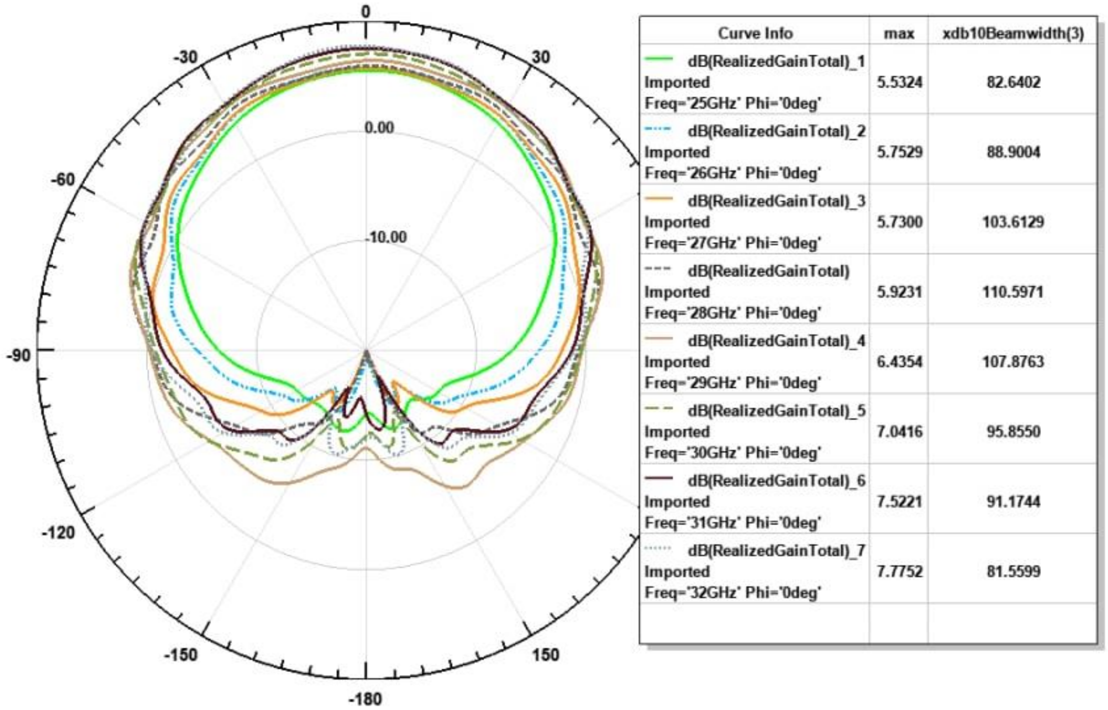

(a)

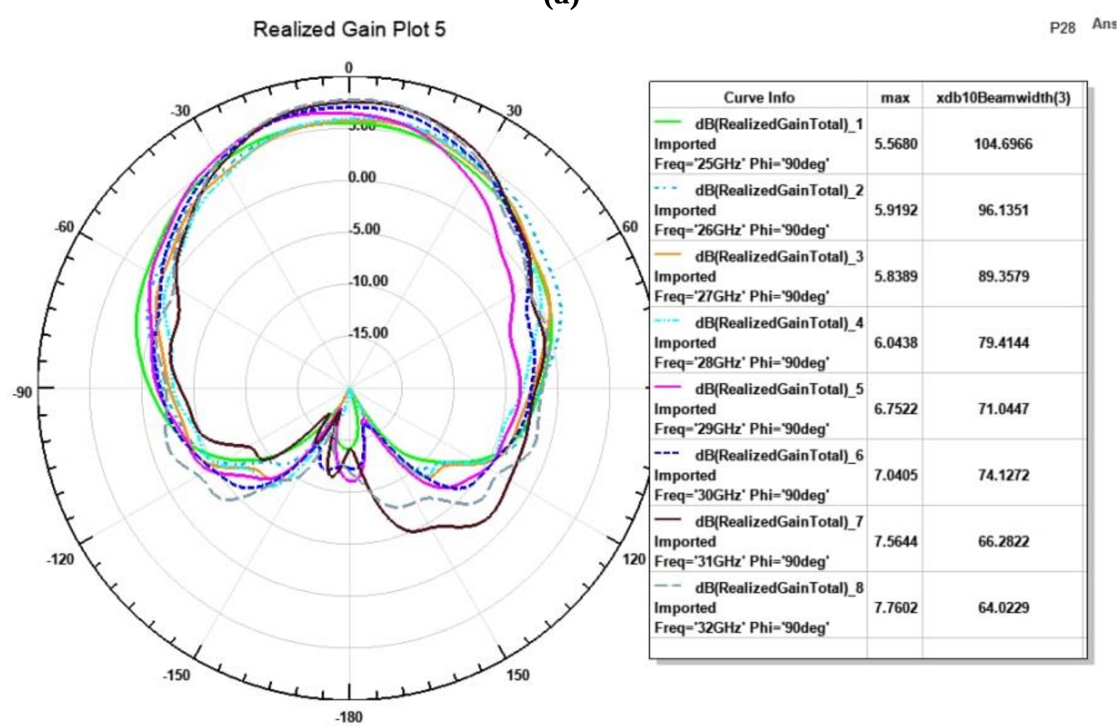

(b)

Figure 5-5: Single element realized gain radiation pattern for 25-32GHz (a): cut φ=0° (b): cut φ=90° element antenna

Figure 5-6 shows the realized gain as a function of frequency. This graph depicts the proposed single-element antenna's 3dB bandwidth is 6.62 GHz.

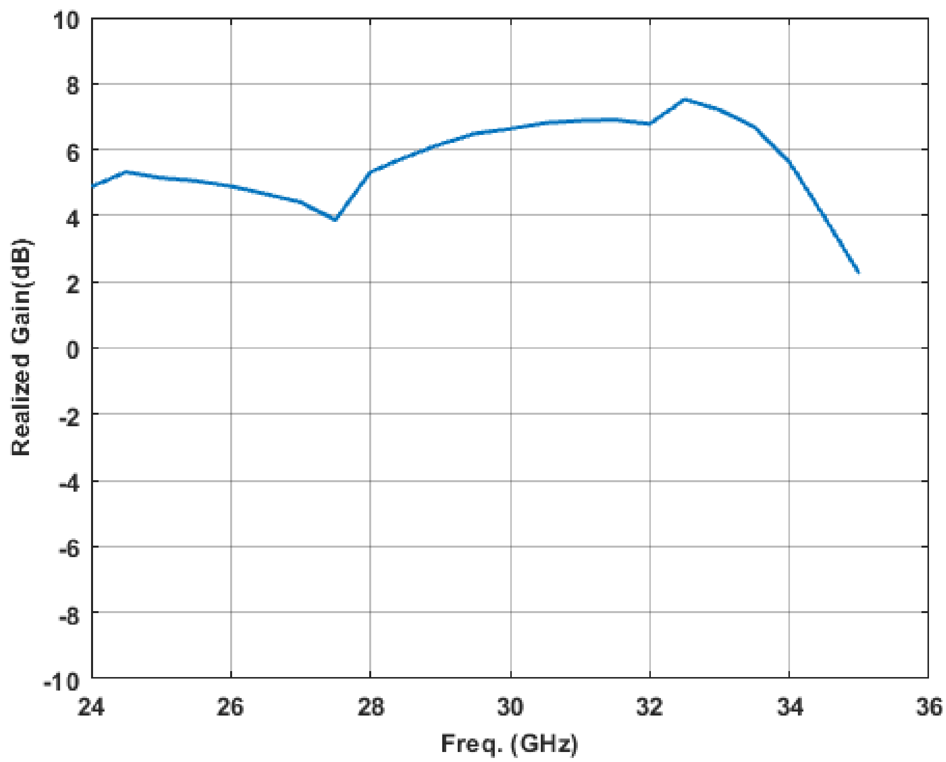

Figure 5-6: The realized gain of the proposed single-element antenna as a function of frequency.

5.2.2 Single Element antenna with SMPM connector

Because of the small mm-wave wavelength and high dielectric constant of Dupont 9K7, i.e., 7.1, the simulation should take the connector's exact model into account. In this regard, an appropriate transition between an SMPM connector and an LTCC stripline was designed in 4.2. Figure 5-7 depicts the suggested single-element antenna connected to the proposed transition. Ten Dupont Green Tape 9K7 LTCC substrate layers with a dielectric constant of $\varepsilon_r = 7.1$ and loss tangent of $\tan\delta = 0.0010$ have been used for the design. The overall size of the single-element antenna is 8×20×2.06 mm^3. Figure 5-8 shows the expanded view of the proposed antenna. The portion of the structure marked with dotted lines in Figure 5-7 that lacks any distinctive characteristic has been removed from Figure 5-8 and Figure 5-9 to improve the clarity of the features in each layer. The details for each metal layer are shown in Figure 5-9. Vias connect the four ground planes to create a cavity effect for suppressing spurious parallel plate modes [11]. Vias are not shown since it would be too wordy; instead, the via holes and catch pads can be used to determine where and how tall the vias are. All vias in a single element do not have the same height, because when creating an array, the connector corresponding to each element is positioned beneath the side element. The solder paste that will be used to assemble the antenna is also taken into account in simulations, as seen in Figure 5-7(b). The green dashed line in Figure 5-8 shows the signal path from the strip line feed to the CPW feed in the bottom layer.

The final optimized dimensions of the proposed antenna are presented in Table 5-2 and all the descriptions of the design parameters in Table 5-2 are labeled in Figure 5-8 and Figure 5-9 accordingly. It should be added that the dimensions of the main and parasitic patches, air cavity, coupling slot, the thickness of metal layers (th), the distance between vias, and substrate thicknesses, including H1, H2, H3, H4, and H5 are the same as the single element antenna shown in Figure 5-2 . As it is explained previously, to avoid camber problems, ground planes are partially gridded. Although, meshing the ground plane would result in higher back radiation and degrade the antenna gain performance, which is undesirable.

The simulated return loss for the single element antenna with SMPM connector is shown in Figure 5-10, the 3D simulated radiation pattern for 28 GHz is depicted in Figure 5-11, as well as realized gain pattern for cut $\varphi=0°$ and $\varphi=90°$ for 24 to 32 GHz are shown in Figure 5-12 (a-b).

Table 5-2: The final optimized dimensions of the proposed Single antenna with an SMPM connector

Parameter	Fx1	Fx4	d_via1	d_via2	d_via3	L2	L4	Lf	d1	d2	d3	L_solder
Value (mm)	0.125	0.4	0.731	1.073	1.4	1	1.9	0.523	0.8	3.4	2	4.4
Parameter	Fx2	Fx3	R1	R2	R3	R4	R5	w1	w2	w3	H6	
Value (µm)	213.7	222.8	569	474.6	889.6	795.6	269.8	745.8	845.8	725.8	448.06	

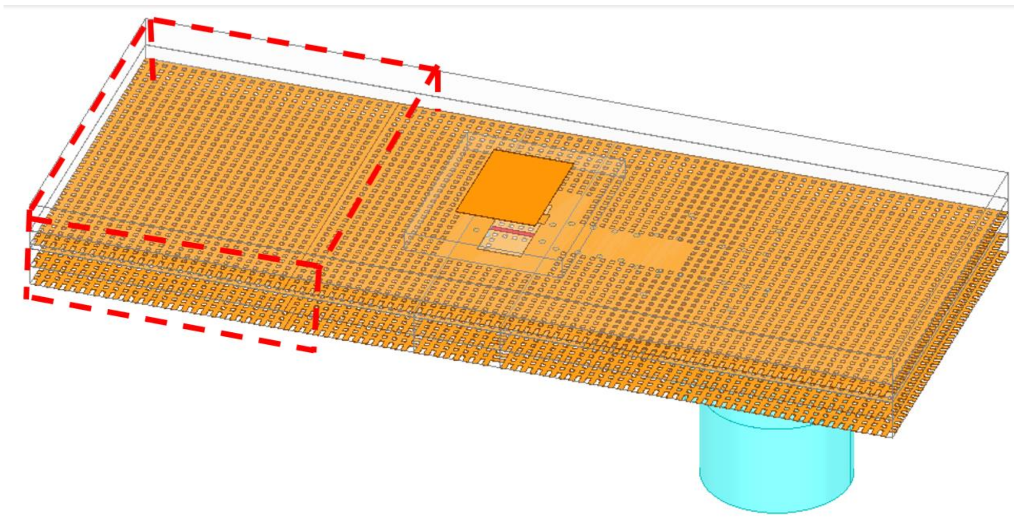

(a)

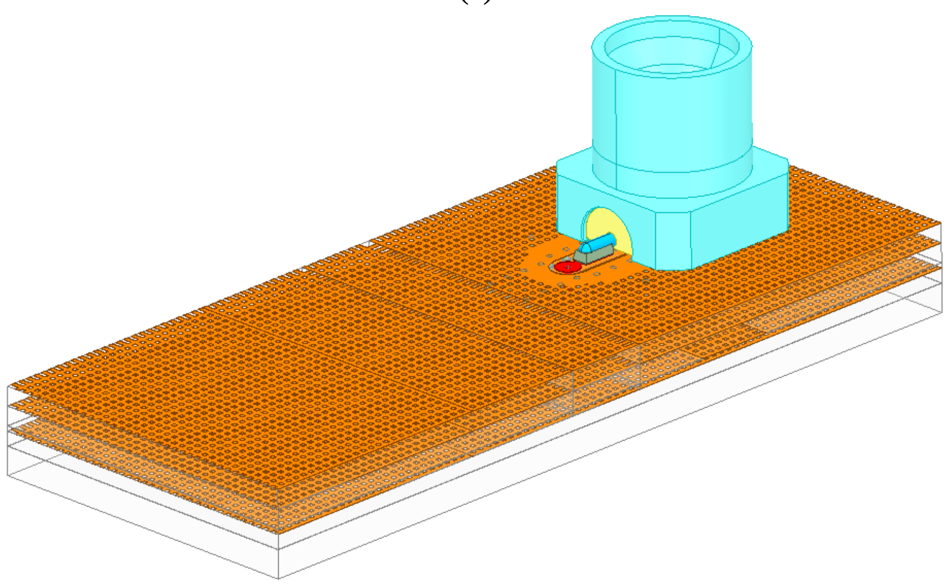

(b)

Figure 5-7: The geometry of the proposed single element antenna connecting to SMPM Rosenberger connector. (a): Top view (b): bottom view

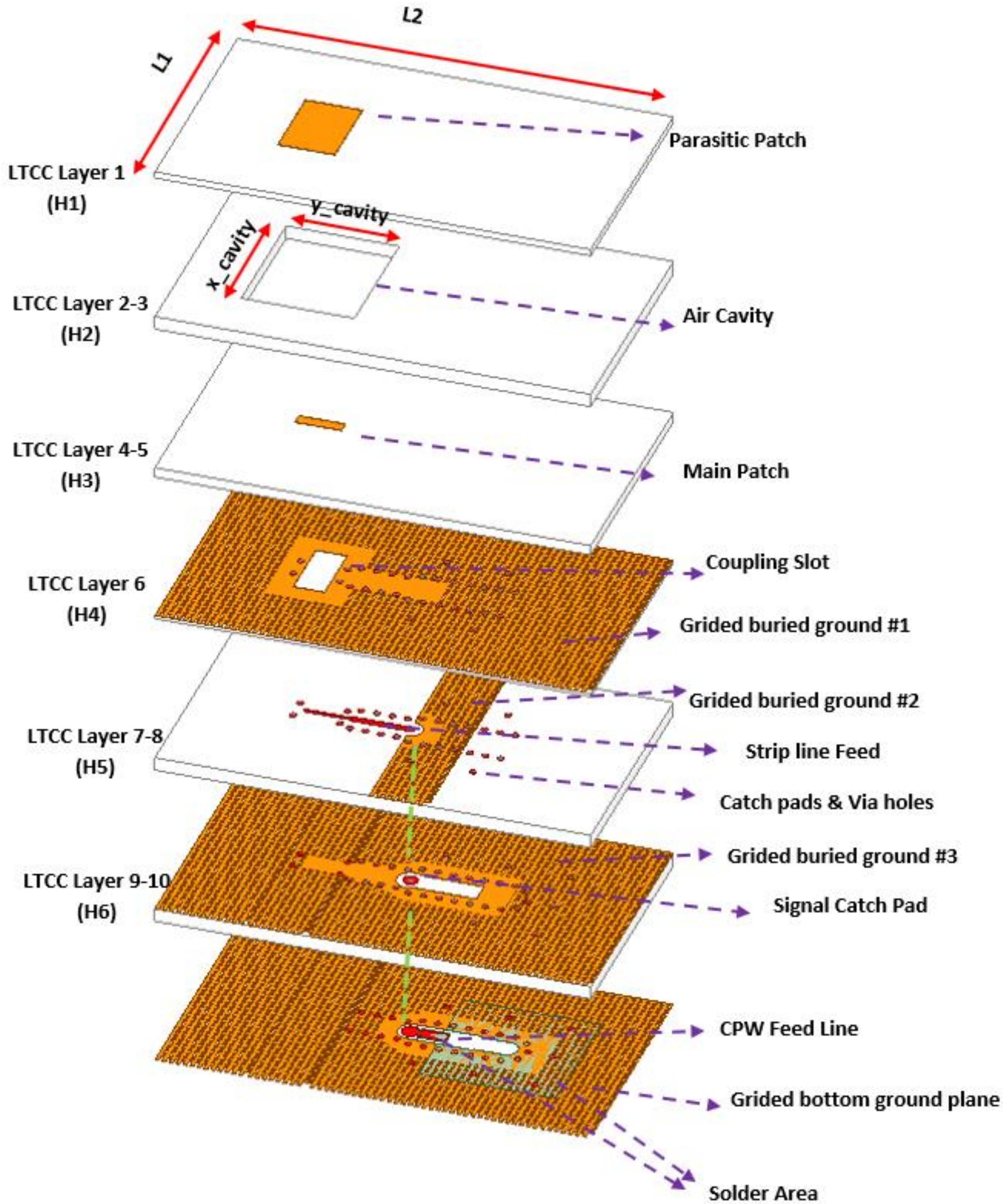

Figure 5-8: Expanded view of the single element antenna with an SMPM connector.

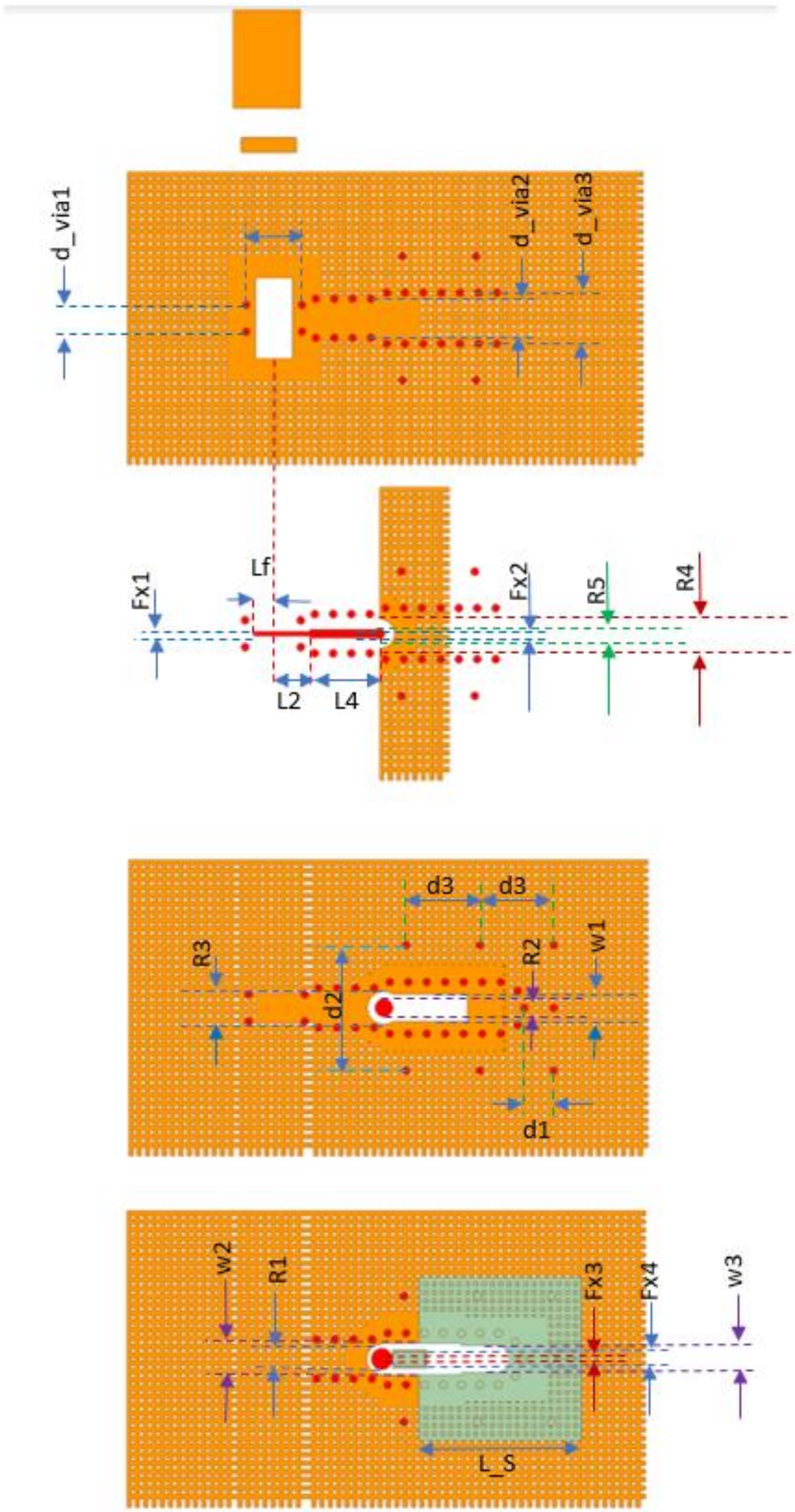

Figure 5-9: Metal layer details of the single element antenna with an SMPM connector.

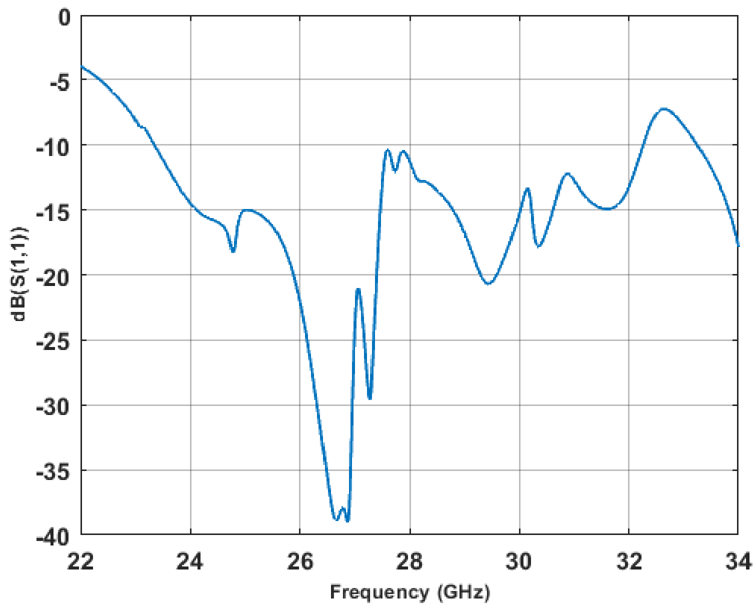

Figure 5-10: Simulated return loss of a single element antenna with a SMP connector

According to Figure 5-10, the single element antenna has 31.8% impedance bandwidth from 23.34 GHz to 32.26 GHz, and 9.1dB realized gain at 28 GHz. According to Figure 5-12, the maximum realized gain changes from 6.2 dB to 9.9 dB in 26 to 31 GHz.

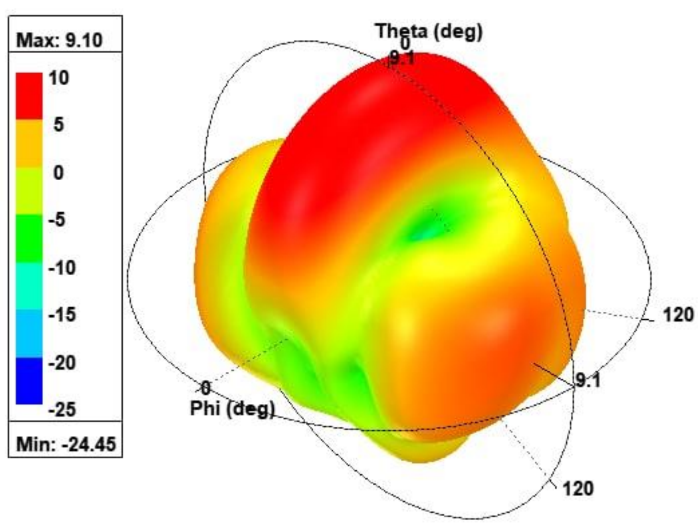

Figure 5-11: 3D realized gain pattern for the proposed single element antenna with a SMPM connector.

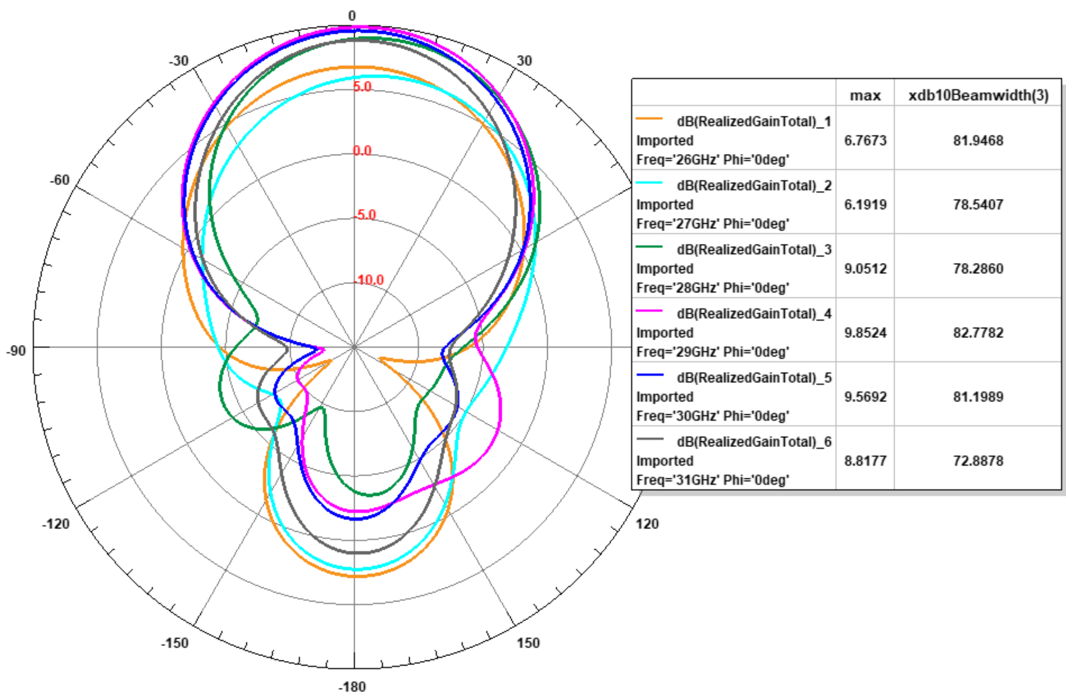

(a)

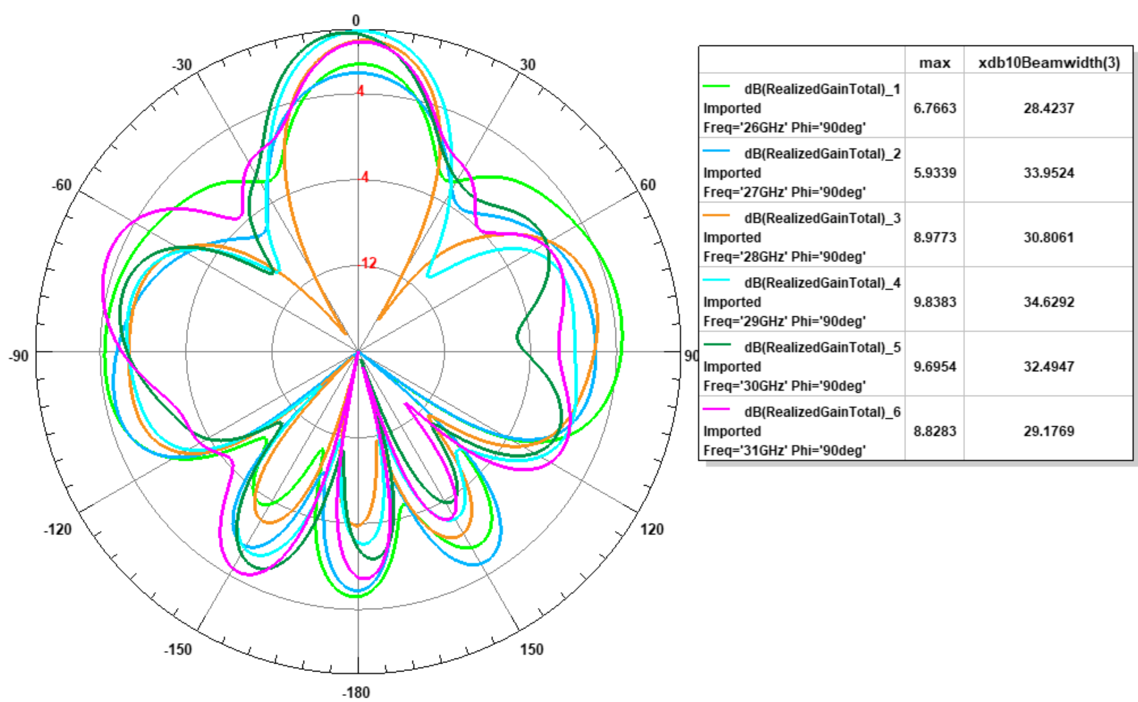

(b)

Figure 5-12: realized gain radiation pattern of single element Antenna connecting to SMPM connector for 25-32GHz (a): cut φ=0° (b): cut φ=90°.

Figure 5-13 shows the realized gain as a function of frequency. This graph depicts the proposed single-element antenna attached to connector has a 3dB bandwidth of 4.5GHz.

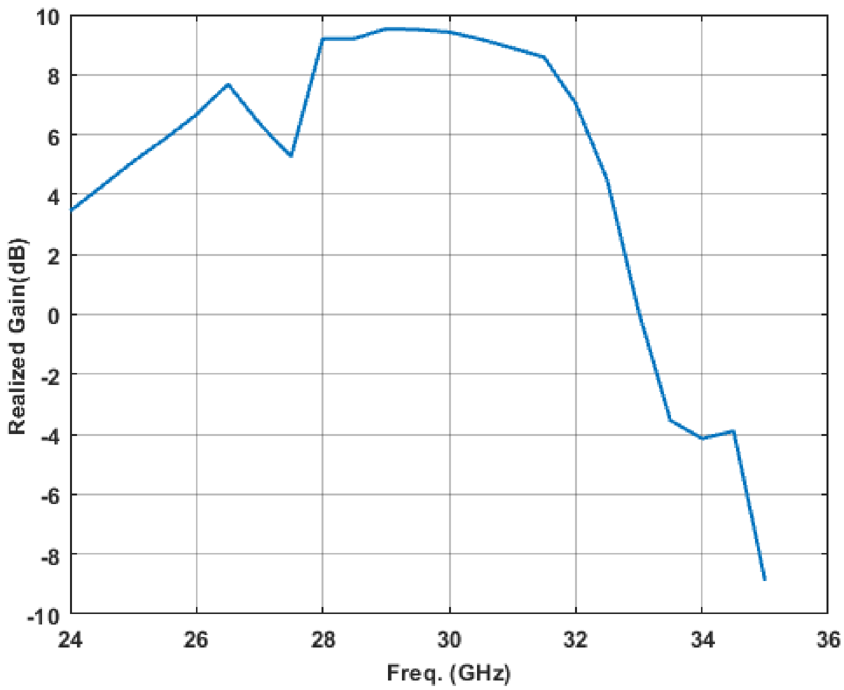

Figure 5-13: The realized gain of the proposed single-element antenna attached to SMPM connector.

5.3 Conclusion

This chapter proposes a broadband cavity-backed patch antenna in LTCC technology for 5G applications. First, the proposed single-element antenna, excited by stripline feed, was designed and simulated in the K and Ka frequency bands. Then, by connecting the proposed transition, described in chapter four, to the single-element antenna, a single-element fed by an SMPM connector was simulated, and its results were presented in detail. In this chapter, the simulation results show an impedance bandwidth of 31.8% and 35.7% for the proposed antenna with and without an SMPM connector, respectively.

Chapter Six: Fabrication and measurement results

6.1 Introduction

The single element proposed ACMPA and the back-to-back configuration for SMPM coaxial connector to LTCC stripline transition were implemented at École de technologies supérieure in Professor Kouki’s LTCC laboratory. this chapter presents the antenna assembly process and the measurement results.

6.2 Assembling of SMPM connectors on the antenna board

In this stage, Rosenberger Mini SMP connectors had to be assembled on the antenna boards. However, due to the type of gold used in the manufacturing process, I faced a challenge in choosing the right solder paste for connecting SMPM connectors to the fabricated antenna board.

Figure 6-1 shows the footprint of the connector on the board and the bottom side of the connector. The LTCC board has two pads, a large pad to attach the connector’s body and the other small one to connect the connector's pin.

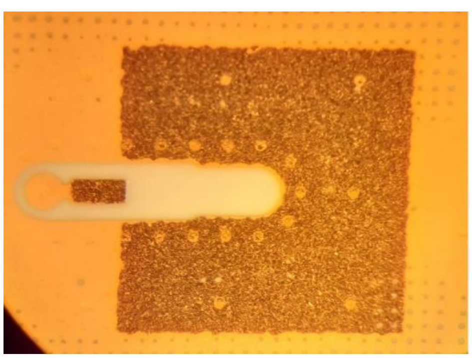

(a)

(b)

Figure 6-1: (a): the footprint of the connector on the board (b): The bottom side of the connector

Connectors were soldered on the board by a reflow oven using two types of solder paste, i.e., lead paste (SMD291AX10 from CHIPQUIK company with Sn63/Pb37) and unleaded paste (TS391SNL50 from CHIPQUIK company with: Sn96.5/Ag3.0/Cu0.5). We precisely followed the instructions on the solder paste datasheet for each case to set the reflow process's thermal profile. On the LTCC board, all connectors failed to connect properly while using the unleaded paste, and roughly 20% of connections failed using the lead paste. Figure 6-2 (a) illustrates the failure pattern for the leaded paste, which was the dissolution of the small pad on the LTCC board underneath the connector's pin, and Figure 6-2(b) illustrates the failure pattern for the unleaded paste, which was the dissolution of both the large pad and small pad.

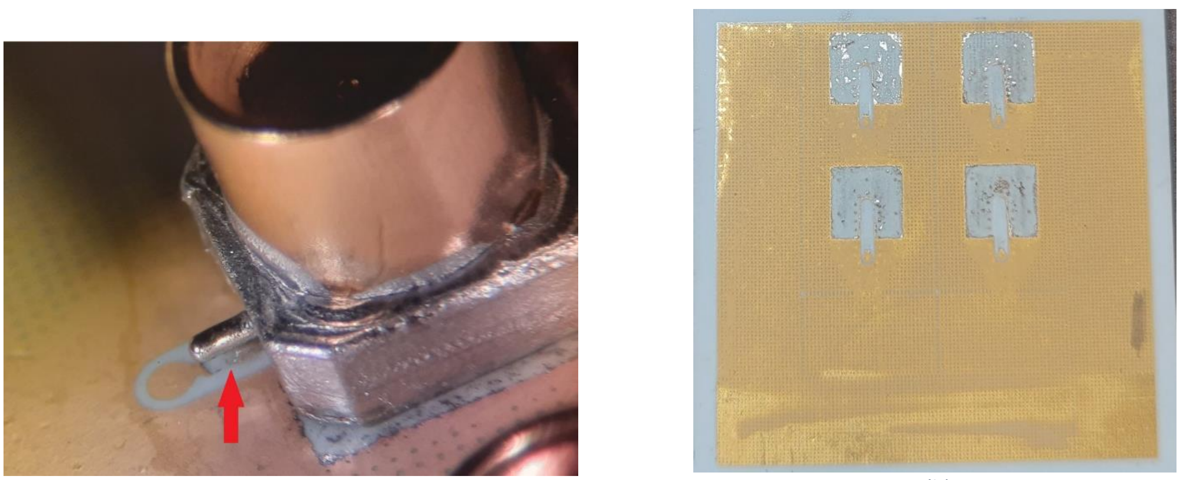

(a) (b)

Figure 6-2: The failure pattern for: (a): the leaded paste (b): the unleaded paste

The unleaded solder paste had a substantially greater failure rate because it required a higher temperature reflow thermal profile (250 °C max) than the leaded paste (215 °C max). Accordingly, we decided to use 8330S-21G epoxy for the next round, which has a much less temperature reflow thermal profile. However, it lacked mechanical robustness, and connectors were detached easily.

With more search on the web, according to [52], we realized the Tin content of the solder paste was dissolving the gold microstrip lines over the antenna board.

Finally, we made a choice to apply TS391LT50 solder paste (Bi57.6/Sn42/Ag0.4), a low-temperature solder paste that is also Tin free. Despite finding the solution, we lost the two-by-two array throughout these trials. Figure 6-3 shows the Single element antenna array and the proposed transition, in which connectors are properly and firmly connected with TS391LT50 solder paste.

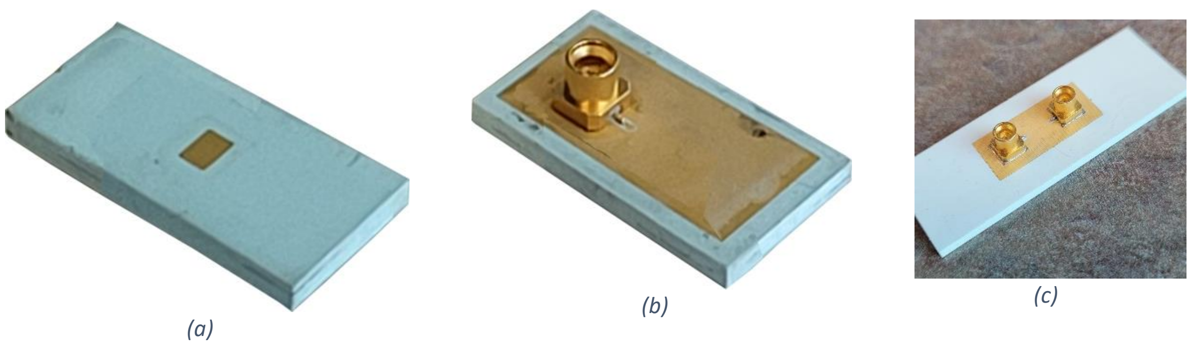

Figure 6-3: (a) Top view of the proposed single element antenna (b)Bottom View of the proposed single element antenna (c) Fabricated coaxial SMPM-to-LTCC Stripline transition

6.3 Measurement Results

For the proposed single-element antenna and SMPM coaxial connector to LTCC transition, the same measurement setups were used for S-parameter measurements, as shown in Figure 6-4. Because of the lack of an SMPM calibration kit in our lab, a 2.4mm calibration kit was used.

6.3.1 SMPM coaxial connector to LTCC stripline transition

The SMPM coaxial connector to LTCC stripline transition was modeled, simulated, and optimized by Ansys Electromagnetic Suite 2022 R2. As shown in Figure 6-3(c), the back-to-back configuration was fabricated and measured to validate the design. Experimental results show that

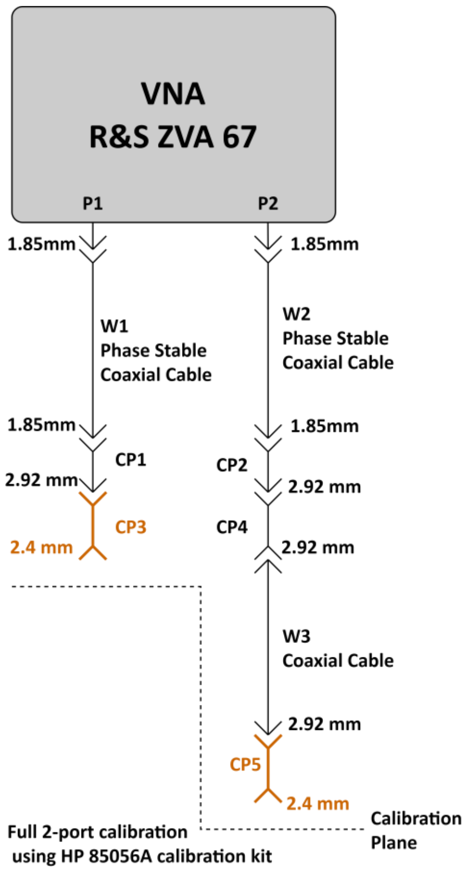

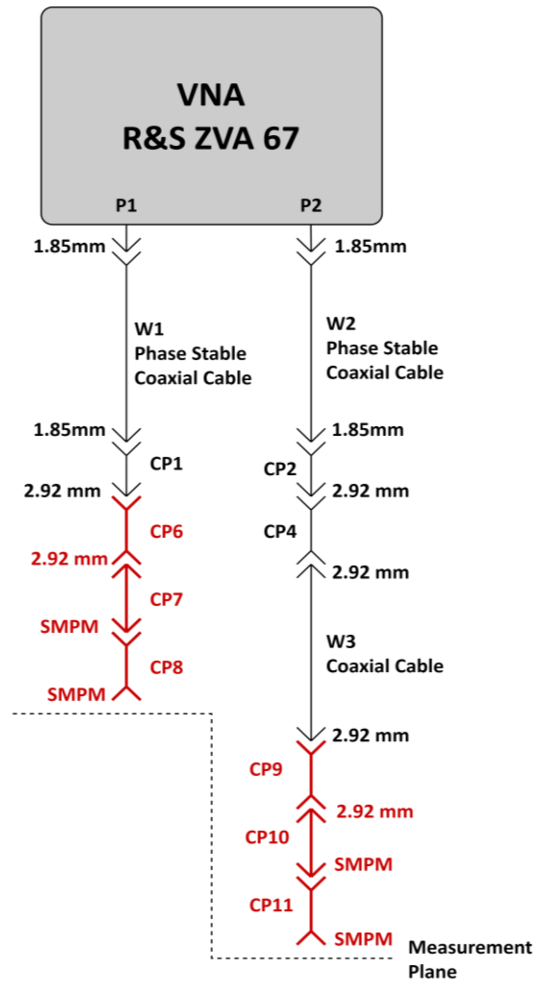

Figure 6-4: Measurement setup block diagram for the proposed antenna and transition.

the return loss is better than 10 dB between 8-32 GHz and the insertion loss is around 1dB from 9 GHz to 31 GHz, see Figure 6-5. The simulated insertion loss of a simple stripline, with the same length and substrate parameters as the proposed transition but excluding vertical transitions and connectors, is found to be about 0.4 dB away from simulated results, as presented in Figure 6-5 (b). In contrast, the proposed coaxial-to-stripline, including a vertical transition and SMPM connector, has a measured insertion loss of around 1 dB. This slight difference between a simple stripline and the proposed transition confirms the excellent performance of the proposed structure.

According to Figure 6-5, a reasonable agreement between simulation and measurement results is achieved. The difference between results in simulation and measurement can be caused by mechanical misalignment in the LTCC fabrication process and the soldering process to mount the coaxial SMPM connector on the LTCC substrate.

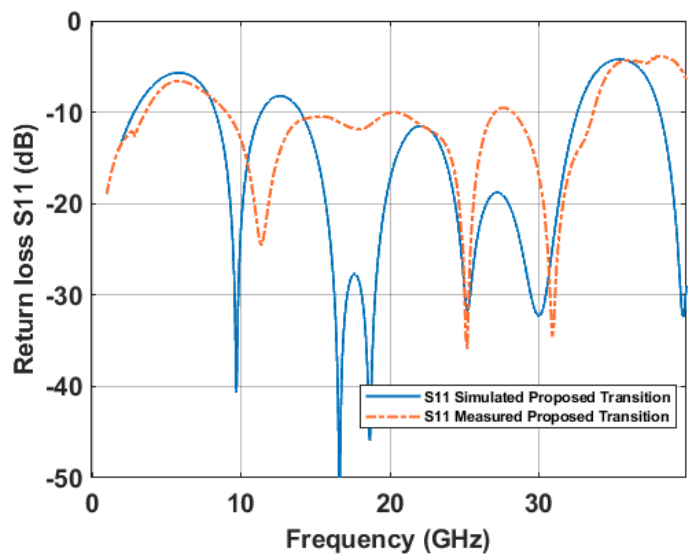

(a)

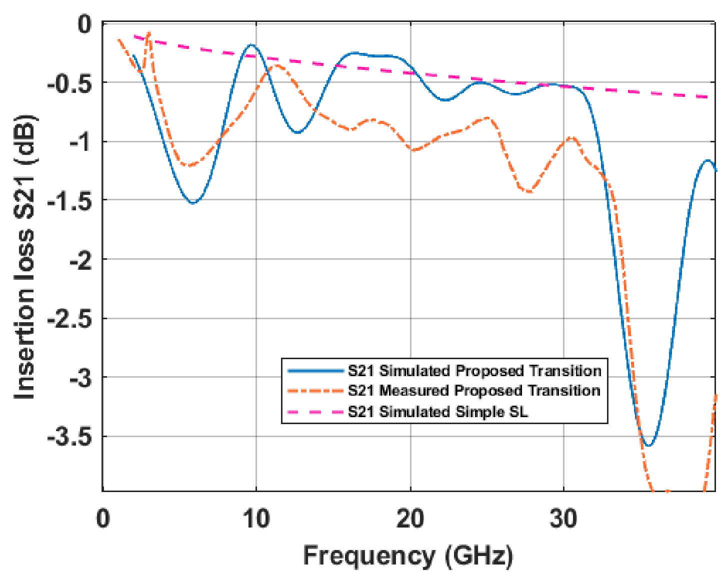

(b)

Figure 6-5: Measured and simulated results of the back-to-back configuration (a) Return loss (b) insertion loss.

6.3.2 Wideband LTCC aperture coupled Patch antenna

The return loss of the proposed single-element antenna was measured by Rohde & Schwarz ZVA67 VNA and is presented in Figure 6-6.

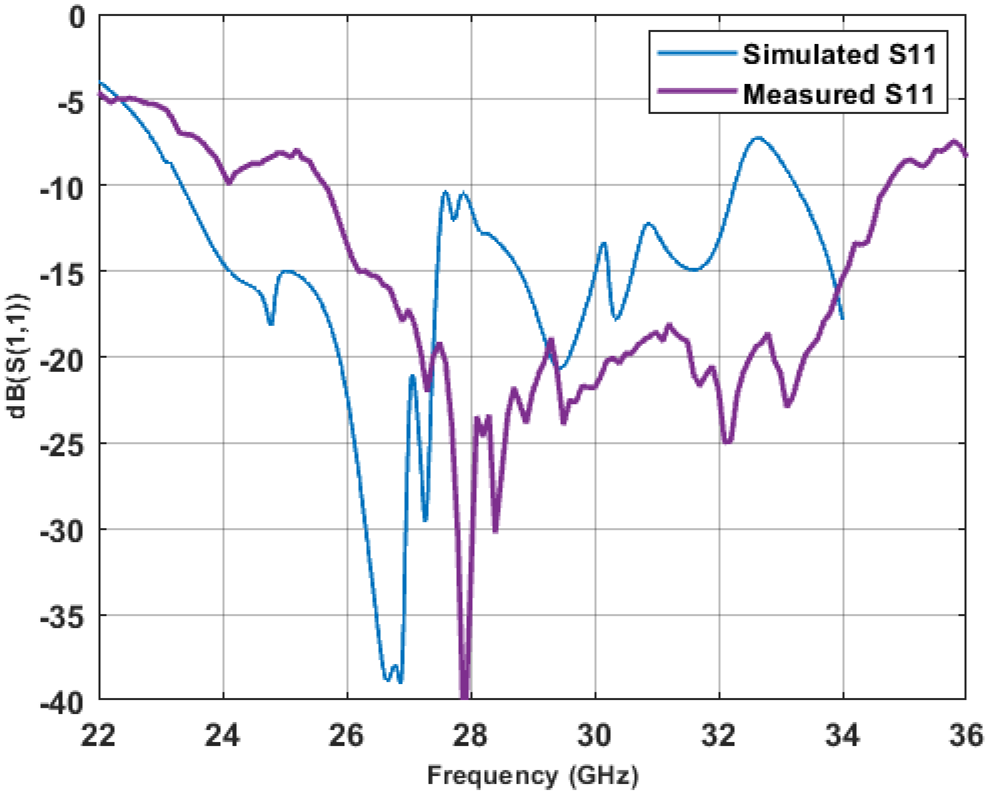

Figure 6-6: Measured and simulated return loss of proposed single element antenna.

According to Figure 6-6, a reasonable agreement between simulation and measurement results is achieved. The measured return loss of the proposed antenna showed a 6% upward frequency shift. The shift was probably caused by the somewhat cambered cavity roof on the electrically measured samples or also caused by mechanical misalignment in the LTCC fabrication process and the soldering process to mount the coaxial SMPM connector on the LTCC substrate. In both simulation and measurement results, there is a 32.14% impedance bandwidth.

6.3.3 Radiation Pattern for the Proposed single element antenna with and without connector

In Table 6-1 and Figure 6-7 radiation characteristics of the proposed single-element antenna are compared in the ideal scenario without taking an actual model of an SMPM connector into account and considering the accurate SMPM model into simulations. When using an exact model of an SMPM connector and its related transition, we can observe that the suggested single-element antenna has a realized gain that is 3 dB higher than the other one. The size of the single-element antenna connected to the SMPM connector can be linked to this enhancement; see Figure 5-1 and Figure 5-7. The proposed transition caused an 11.9 mm increase in the antenna's size in the y direction. To investigate this increased gain, the proposed single element antenna without connector with a similar size to the single element with connector was simulated. According to Figure 6-8 and Figure 6-9, by increasing the length of the single element fed by SL, its gain has improved around 2.5dB, without adding more ground layers, which was used for the proposed transition. The remaining 0.5dB increase can be also attributed to the proposed transition structure in Figure 4-2. In fact, the proposed transition by adding two more ground layers and many vias has helped decrease the surface wave and increase the gain. It should be considered that the inter-element spacing wouldn't be as high, inferring from Figure 5-7, for an array configuration since each element's connector would be positioned beneath the adjacent element. In both cases, the cross-polarization in cut =0° is excellent and nearly identical. The cross-polarization level for cut φ=90° has dropped for the case with an SMPM connector, even if it is still adequate in both cases. This degradation may be caused by the TM_{02} mode being excited within the structure or by surface wave modes being excited in added LTCC layers and radiating from the edges of the structure.

The bandwidth (BW) and sidelobe level (SLL), back lobe level (BLL), and cross-polarization for the case with an SMPM connector are all worsened, and this discrepancy between the two cases confirms the importance of considering a real model of any connector and its appropriate transition in the antenna design in mm-Wave band.

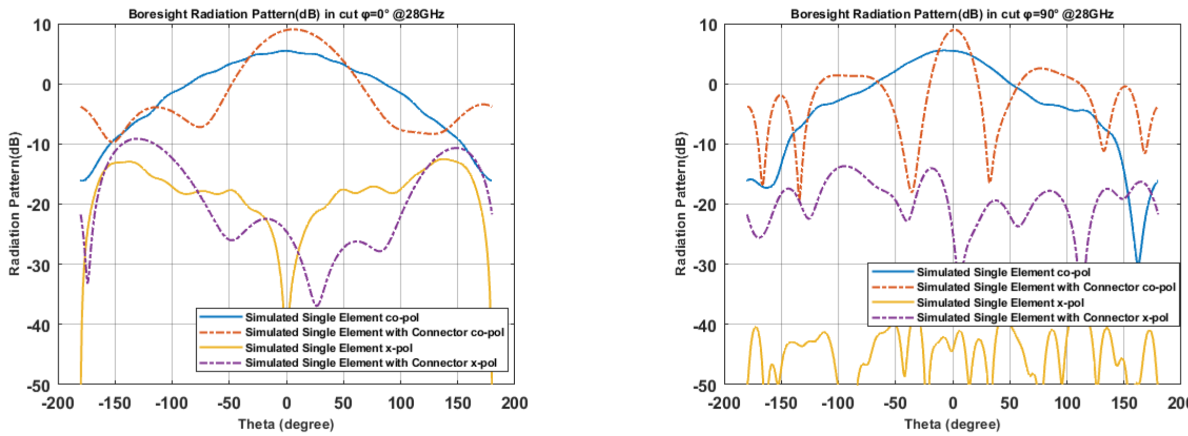

(a) (b)

Figure 6-7:Boresight radiation pattern for the proposed antenna with and without an SMPM connector (a) cut φ=0° (b) cut φ=90°.

Table 6-1: Radiation Properties of the Proposed Antenna with and without an SMPM Connector.

Radiation Properties	Single Element (without an SMPM connector)	Single Element (with an SMPM connector)
Realized Gain	5.48 dBi	9.05 dBi
Bandwidth	35.7 %	31.8 %
HPBW (cut φ=0°)	113.96°	63.5°
HPBW (cut φ=90°)	80.96°	25.45°
SLL (cut φ=0°)	-	12.48 dB
SLL (cut φ=90°)	21.6 dB	6.42 dB
BLL (cut φ=0°)	21.62 dB	12.86 dB
BLL (cut φ=90°)	21.6 dB	12.86 dB
η_r (Radiation Efficiency)	0.97	0.9
Size	8×8×1.6 mm^3	8×19.9×2 mm^3

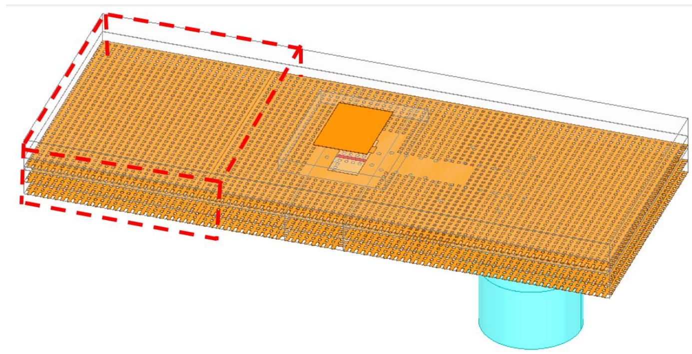

(a)

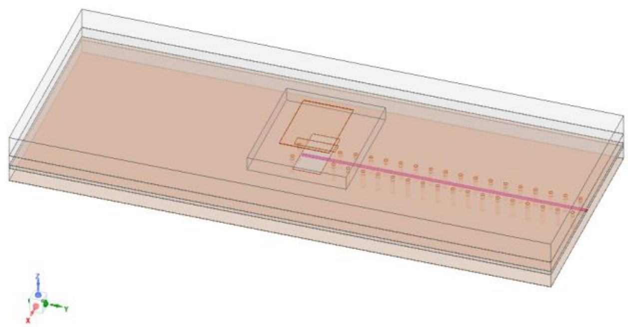

(b)

Figure 6-8: Two variants of the proposed single-element antenna with same ground plane sizes (a) with and (b) without SMPM connector.

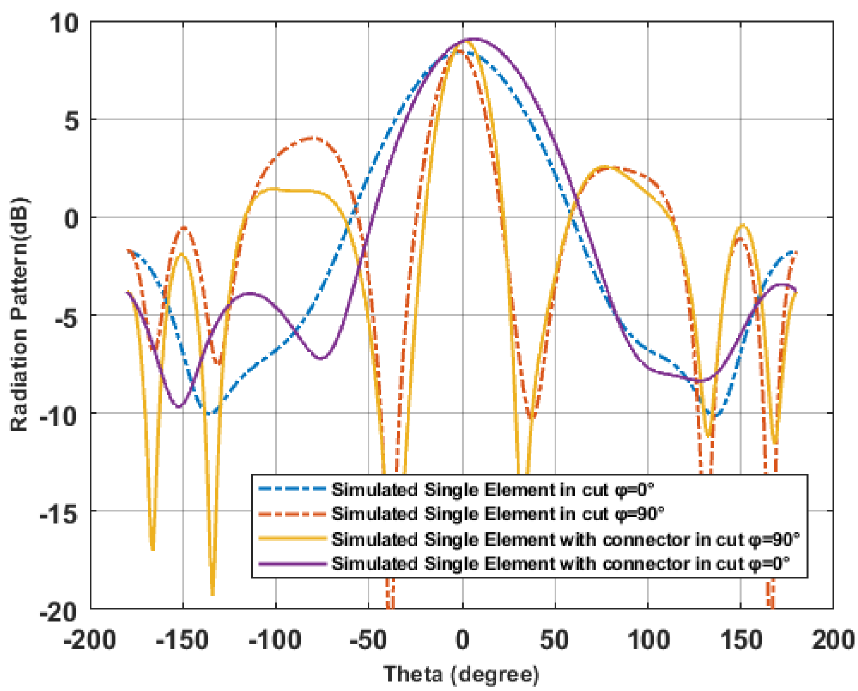

Figure 6-9: The realized gain radiation patterns of the single element antennas with and without the SMPM connector

6.4 Comparison between previous works and the proposed single element antenna

The proposed antenna in this work is compared to various other research studies in Table 6-2. The suggested antenna, as demonstrated, has a wide bandwidth and high gain in the mm-Wave band despite having a high dielectric constant of the substrate. This comparison confirms the effectiveness and suitability of the proposed design in the mm-wave band for 5G applications.

Table 6-2: Comparison between previous works and the proposed wideband LTCC patch antenna

Ref.	Substrate	ε_r	Element	Height (mm)	BW (%)	f_c (GHz)	Ant. Gain (dBi)
[29]	RT/duroid® 5880	2.2	16×16	2.98	17	16.7	20
[11]	LTCC A6M	5.7	1	1.1	16	35	8
[33]	RT/duroid® 5880	2.2	1	3.05	21.5	9.5	9
[12]	LTCC foil ESL	4.05	1	0.14	12.5	120	8
[37]	LTCC A6S	5.9	1	1.18	18	27	5
[38]	LTCC A6S	5.99	4×4	0.6	9.5	60	18.2
[40]	LTCC DuPont 951	7.8	1	2	6.8	10	5.4
[41]	LTCC DuPont 9V7K	7.1	4×4	0.448	9	60	16.3
This work	LTCC DuPont 9K7	7.1	1	1.64	34.5	29	6.05

6.5 Conclusion

This chapter presents the fabrication and measurement results of the proposed SMPM coaxial connector to LTCC stripline transition and the proposed broadband cavity-backed patch antenna. First, challenges to choosing the appropriate paste to connect connectors to the LTCC board are discussed. Then, the measurement results for the back-to-back configuration of the proposed transition are presented. Next, the measurement result for the proposed single-element antenna is presented. For both cases, measurement results show reasonable agreement with K and Ka frequency band simulations. Finally, the results have been compared with previous results obtained by other researchers to show its performance.

Chapter Seven: Conclusions and Future Works

7.1 Research summary

An mm-wave wideband LTCC cavity-backed ACMPA with stable radiation patterns at 28 GHz was designed and implemented with Dupont's 9k7 LTCC technology, with a dielectric constant of 7.1. The purpose is to design an antenna element to b e used in an active phase array antenna array for 5G applications. A stacked patch, embedded air cavity, and large aperture were employed to increase the bandwidth. In the mm-wave band, the embedded air cavity increases gain and decreases losses brought on by surface waves.

The proposed configuration was designed and simulated using the HFSS (High-Frequency Structure Simulator), which is based on the finite element method. First, a single-element antenna fed by a stripline was designed and simulated and encouraging results were obtained including a maximum gain of 6 dB at 28 GHz and a 35.7% impedance bandwidth. Then, a broadband SMPM coaxial connector to LTCC stripline transition was also designed in order to feed and test the antenna. A back-to-back configuration was designed, fabricated, and measured as well to confirm the design. Experimental results showed a return loss of better than 10 dB between 8 to 32 GHz and an insertion loss of around 1 dB from 9 GHz to 31 GHz and a good agreement with the simulations.

Finally, by attaching the proposed transition to the proposed single-element at the first step, the proposed single-element antenna fed by SMPM connector was simulated and fabricated in the LTCC lab in École de technologies supérieure in Montreal. A reasonable agreement between simulation and measurement results was achieved. The measured return loss of the proposed antenna showed a 6% upward frequency shift. The shift was probably caused by the somewhat cambered cavity roof on the electrically measured samples or also can be caused by mechanical misalignment in the LTCC fabrication process and the soldering process to mount the coaxial SMPM connector on the LTCC substrate. In both simulation and measurement results, 32.14% impedance bandwidth was achieved.

7.2 Future Works

The features of multilayered implementation, low dielectric loss, and excellent packaging properties ensure a compact and high-efficiency single-element antenna appropriate for phased array design, applicable for 5th-generation mobile networks. All these characteristics qualify this design as an antenna-in-packaging (AiP) design. In this regard, the suggestions for further improvements of this research are as follows:

- Design and simulation a four-by-four phased array based on the designed antenna element and adjust the phase at each element to steer the pattern in angular space for all frequencies included in the bandwidth (22-32 GHz)
- fabrication of the four-by-four phased array based on the designed antenna element and testing its performance using an off-the-shelf beam former.
- Design and fabricate an active phased array by integrating the off-the-shelf beamformer ICs such as ADMV4801 on the back side of the antenna array board.

7.3 Publication

One accepted paper for the 2023 EUCAP conference, and one additional paper is under preparation, for submittal to IEEE Antenna and propagation. A detailed list of these publications is given below.

“A Broadband Coaxial to Stripline Transition for Millimeter-wave LTCC Circuit Applications”, accepted in Dec. 2022 for EuCAP 2023.

‘’A Broadband LTCC Millimeter-wave Phased Array antenna for 5G Applications” to be submitted in Jan. 2023 to IEEE transaction on Antennas and Propagation.

References

[1] M. Giordani, M. Mezzavilla, and M. Zorzi, “Initial Access in 5G mmWave Cellular Networks,” *IEEE Commun. Mag.*, vol. 54, no. 11, pp. 40–47, Nov. 2016, doi: 10.1109/MCOM.2016.1600193CM.

[2] R. T. Prabu, M. Benisha, V. T. Bai, and V. Yokesh, “Millimeter wave for 5G mobile communication application,” in *2016 2nd International Conference on Advances in Electrical, Electronics, Information, Communication and Bio-Informatics (AEEICB)*, Feb. 2016, pp. 236–240. doi: 10.1109/AEEICB.2016.7538280.

[3] C. Seker, M. T. Güneser, and T. Ozturk, “A Review of Millimeter Wave Communication for 5G,” in *2018 2nd International Symposium on Multidisciplinary Studies and Innovative Technologies (ISMSIT)*, Oct. 2018, pp. 1–5. doi: 10.1109/ISMSIT.2018.8567053.

[4] Y. Niu, Y. Li, D. Jin, L. Su, and A. V. Vasilakos, “A survey of millimeter wave communications (mmWave) for 5G: opportunities and challenges,” *Wirel. Netw.*, vol. 21, no. 8, pp. 2657–2676, Nov. 2015, doi: 10.1007/s11276-015-0942-z.

[5] Y. Niu, Y. Li, D. Jin, L. Su, and A. V. Vasilakos, “A survey of millimeter wave communications (mmWave) for 5G: opportunities and challenges,” *Wirel. Netw.*, vol. 21, no. 8, pp. 2657–2676, Nov. 2015, doi: 10.1007/s11276-015-0942-z.

[6] Junyi Wang *et al.*, “Beam codebook based beamforming protocol for multi-Gbps millimeter-wave WPAN systems,” *IEEE J. Sel. Areas Commun.*, vol. 27, no. 8, pp. 1390–1399, Oct. 2009, doi: 10.1109/JSAC.2009.091009.

[7] Y. M. Tsang, A. S. Y. Poon, and S. Addepalli, “Coding the Beams: Improving Beamforming Training in mmWave Communication System,” in *2011 IEEE Global Telecommunications Conference - GLOBECOM 2011*, Dec. 2011, pp. 1–6. doi: 10.1109/GLOCOM.2011.6134486.

[8] J. Qiao, X. Shen, J. W. Mark, and Y. He, “MAC-layer concurrent beamforming protocol for indoor millimeter-wave networks,” *IEEE Trans. Veh. Technol.*, vol. 64, no. 1, pp. 327–338, Jan. 2015, doi: 10.1109/TVT.2014.2320830.

[9] M. Maggi *et al.*, “Millimeter-Wave Phased Arrays and Over-the-Air Characterization for 5G and Beyond: Overview on 5G mm-Wave Phased Arrays and OTA Characterization,” *IEEE Microw. Mag.*, vol. 23, no. 5, pp. 67–83, May 2022, doi: 10.1109/MMM.2022.3148328.

[10] K. K. Samanta, “Cost-Effective Technologies for Next-Generation System on Package: Multilayer Transmission Lines and Interconnects for 5G and Millimeter-Wave,” *IEEE Microw. Mag.*, vol. 23, no. 8, pp. 50–65, Aug. 2022, doi: 10.1109/MMM.2022.3173467.

[11] L. Li, Y. Zhang, J. Wang, W. Zhao, S. Liu, and R. Xu, “Bandwidth and Gain Enhancement of Patch Antenna with Stacked Parasitic Strips Based on LTCC Technology,” *Int. J. Antennas Propag.*, vol. 2014, p. 461423, Jul. 2014, doi: 10.1155/2014/461423.

[12] J. Sobolewski and P. R. Bajurko, “Design of LTCC patch antenna for increased bandwidth and reduced susceptibility to fabrication process inaccuracies,” in *2018 22nd International Microwave and Radar Conference (MIKON)*, May 2018, pp. 218–221. doi: 10.23919/MIKON.2018.8405182.

[13] A.B. Kouki, “LTCC at ETS.” https://en.etsmtl.ca/unites-de-recherche/ltcc/accueil (accessed Nov. 20, 2022).

[14] X. Sun, J. -M. Fernández-González, and M. Sierra-Pérez, “Development of aperture-coupled patch array antennas at 60 GHz for 5G applications,” in *2018 IEEE International Symposium*

on Antennas and Propagation & USNC/URSI National Radio Science Meeting, Jul. 2018, pp. 1695–1696. doi: 10.1109/APUSNCURSINRSM.2018.8609190.

[15] C. A. Balanis, *Antenna theory*, 4th ed. Standards Information Network, 2015.

[16] R. Garg, Ed., *Microstrip antenna design handbook*. Boston, MA: Artech House, 2001.

[17] W. L. Stutzman and G. A. Thiele, *Antenna Theory and Design*, 3rd ed. Chichester, England: John Wiley & Sons, 2012.

[18] C. A. Balanis, *Advanced engineering electromagnetics*, 2nd ed. Hoboken, N.J: John Wiley & Sons, 2012.

[19] Zhi Ning Chen and Xianming Qing, "Gain Enhancement of LTCC Microstrip Patch Antenna by Suppressing Surface Waves," in *Substrate-Integrated Millimeter-Wave Antennas for Next-Generation Communication and Radar Systems*, IEEE, 2021, pp. 197–209. doi: 10.1002/9781119611165.ch8.

[20] D. M. Pozar, "Microstrip antennas," *Proc. IEEE*, vol. 80, no. 1, pp. 79–91, Jan. 1992, doi: 10.1109/5.119568.

[21] J. Huang, "Microstrip Antennas: Analysis, Design, and Application," in *Modern Antenna Handbook*, 2008, pp. 157–200. doi: 10.1002/9780470294154.ch4.

[22] K. F. Lee, K. M. Luk, K. F. Tong, S. M. Shum, T. Huynh, and R. Q. Lee, "Experimental and simulation studies of the coaxially fed U-slot rectangular patch antenna," *IEE Proc. - Microw. Antennas Propag.*, vol. 144, no. 5, pp. 354-358(4), Oct. 1997.

[23] C. A. Balanis, *Modern Antenna Handbook*. Somerset: Wiley, 2011.

[24] S. D. Targonski and D. M. Pozar, "Design of wideband circularly polarized aperture-coupled microstrip antennas," *IEEE Trans. Antennas Propag.*, vol. 41, no. 2, pp. 214–220, Feb. 1993, doi: 10.1109/8.214613.

[25] M. Singh, A. Basu, and S. K. Koul, "Design of Aperture Coupled Fed Micro-Strip Patch Antenna for Wireless Communication," in *2006 Annual IEEE India Conference*, Sep. 2006, pp. 1–5. doi: 10.1109/INDCON.2006.302848.

[26] A. E. I. Lamminen, J. Säily, and A. R. Vimpari, "Design and Processing of 60 GHz Antennas on Low Temperature Co-fired Ceramic (LTCC) Substrates," 2005.

[27] D. M. Pozar, "A Review of Aperture Coupled Microstrip Antennas: History, Operation, Development, and Applications," 1996.

[28] M. Nasirian, F. Zaker Hossein, M. Maddah-Ali, and G. R. Askari, "Design guidelines for proximity coupled U-slot microstrip antennas," *mdrsjrns*, vol. 14, no. 2, pp. 1–9, Aug. 2014.

[29] B. Strassner, "Lightweight, wideband, amplitude-tapered, linearly-polarized, dual-axis monopulse, ku-band patch antenna array for SAR," in *2007 IEEE Antennas and Propagation Society International Symposium*, Jun. 2007, pp. 4409–4412. doi: 10.1109/APS.2007.4396520.

[30] I. Fitri and T. Al Amin Akbar, "A new gridded parasitic patch stacked microstrip antenna for enhanced wide bandwidth in 60 GHz Band," in *2017 International Conference on Broadband Communication, Wireless Sensors and Powering (BCWSP)*, Nov. 2017, pp. 1–4. doi: 10.1109/BCWSP.2017.8272571.

[31] R. Bhalla and L. Shafai, "Resonance behavior of single U-slot and dual U-slot antenna," in *IEEE Antennas and Propagation Society International Symposium. 2001 Digest. Held in conjunction with: USNC/URSI National Radio Science Meeting (Cat. No.01CH37229)*, Jul. 2001, vol. 2, pp. 700–703 vol.2. doi: 10.1109/APS.2001.959820.

[32] Y. L. Chow, Z. N. Chen, K. F. Lee, and K. M. Luk, "A design theory on broadband patch antennas with slot," in *IEEE Antennas and Propagation Society International Symposium. 1998 Digest. Antennas: Gateways to the Global Network. Held in conjunction with: USNC/URSI National Radio Science Meeting (Cat. No.98CH36*, Jun. 1998, vol. 2, pp. 1124–1127 vol.2. doi: 10.1109/APS.1998.702148.

[33] T. Jayanthy, M. Sugadev, J. M. Ismaeel, and G. Jegan, "Design and simulation of Microstrip M-patch antenna with double layer," in *2008 International Conference on Recent Advances in Microwave Theory and Applications*, Nov. 2008, pp. 230–232. doi: 10.1109/AMTA.2008.4763102.

[34] T. Jayanthy, M. Sugadev, J. M. Ismaeel, and G. Jegan, "Design and simulation of Microstrip M-patch antenna with double layer," in *2008 International Conference on Recent Advances in Microwave Theory and Applications*, Nov. 2008, pp. 230–232. doi: 10.1109/AMTA.2008.4763102.

[35] Wansuk Yun and Young-Joong Yoon, "A wide-band aperture coupled microstrip array antenna using inverted feeding structures," *IEEE Trans. Antennas Propag.*, vol. 53, no. 2, pp. 861–862, Feb. 2005, doi: 10.1109/TAP.2004.841283.

[36] M. Yamazaki, E. T. Rahardjo, and M. Haneishi, "Construction of a slot-coupled planar antenna for dual polarisation," *Electron. Lett.*, vol. 30, no. 22, pp. 1814–1815, Oct. 1994, doi: 10.1049/el:19941261.

[37] A. Panther, A. Petosa, M. G. Stubbs, and K. Kautio, "A wideband array of stacked patch antennas using embedded air cavities in LTCC," *IEEE Microw. Wirel. Compon. Lett.*, vol. 15, no. 12, pp. 916–918, Dec. 2005, doi: 10.1109/LMWC.2005.859944.

[38] A. E. I. Lamminen, J. Saily, and A. R. Vimpari, "60-GHz Patch Antennas and Arrays on LTCC With Embedded-Cavity Substrates," *IEEE Trans. Antennas Propag.*, vol. 56, no. 9, pp. 2865–2874, Sep. 2008, doi: 10.1109/TAP.2008.927560.

[39] N. C. Karmakar, "Investigations into a cavity-backed circular-patch antenna," *IEEE Trans. Antennas Propag.*, vol. 50, no. 12, pp. 1706–1715, Dec. 2002, doi: 10.1109/TAP.2002.807427.

[40] M. Komulainen *et al.*, "Embedded air cavity backed microstrip antenna on an LTCC substrate," *Pap. Present. Fourth Int. Conf. Microw. Mater. Their Appl. - MMA2006 Oulu Finl.*, vol. 27, no. 8, pp. 2881–2885, Jan. 2007, doi: 10.1016/j.jeurceramsoc.2006.11.012.

[41] X. Sun, J. -M. Fernández-González, and M. Sierra-Pérez, "Development of aperture-coupled patch array antennas at 60 GHz for 5G applications," in *2018 IEEE International Symposium on Antennas and Propagation & USNC/URSI National Radio Science Meeting*, Jul. 2018, pp. 1695–1696. doi: 10.1109/APUSNCURSINRSM.2018.8609190.

[42] M. A. Ahmad and L. J. A. Olule, "Meshed Stacked LTCC Antenna for Space Application," *IEEE Access*, vol. 10, pp. 29473–29481, 2022, doi: 10.1109/ACCESS.2022.3158679.

[43] T. Maleszka and G. Jaworski, "Broadband stripline to microstrip transition with constant impedance field matching section for applications in multilayer planar technologies," in *18-th INTERNATIONAL CONFERENCE ON MICROWAVES, RADAR AND WIRELESS COMMUNICATIONS*, Jun. 2010, pp. 1–4.

[44] Huei-Han Jhuang and Tian-Wei Huang, "Design for electrical performance of wideband multilayer LTCC microstrip-to-stripline transition," in *Proceedings of 6th Electronics Packaging Technology Conference (EPTC 2004) (IEEE Cat. No.04EX971)*, Dec. 2004, pp. 506–509. doi: 10.1109/EPTC.2004.1396661.

[45] L. Xia and Ruimin Xu, “Broadband LTCC transition from coaxial connector to stripline for 60GHz application,” in *2012 International Conference on Computational Problem-Solving (ICCP)*, Oct. 2012, pp. 52–54. doi: 10.1109/ICCPS.2012.6384277.

[46] D. Li, J. Xu, B. Zhang, W. Liu, and L. Du, “GCPW to stripline vertical transition for K-band applications in LTCC,” in *2015 Asia-Pacific Microwave Conference (APMC)*, Dec. 2015, vol. 3, pp. 1–3. doi: 10.1109/APMC.2015.7413526.

[47] Shou Lei, Y. X. Guo, and L. C. Ong, “Investigation into CPW to stripline vertical transitions for millimeter-wave applications in LTCC,” in *2005 IEEE International Wkshp on Radio-Frequency Integration Technology: Integrated Circuits for Wideband Comm & Wireless Sensor Networks*, Dec. 2005, pp. 147–149. doi: 10.1109/RFIT.2005.1598896.

[48] H. Zhang, X. Li, and J. Mao, “A New Structure for Broadband Transition Between Differential Stripline and Differential GCPW,” in *2020 International Conference on Microwave and Millimeter Wave Technology (ICMMT)*, Sep. 2020, pp. 1–3. doi: 10.1109/ICMMT49418.2020.9386938.

[49] R. E. Amaya, M. Li, K. Hettak, and C. J. Verver, “A broadband 3D vertical Microstrip to Stripline transition in LTCC using a quasi-coaxial structure for millimetre-wave SOP applications,” in *The 40th European Microwave Conference*, Sep. 2010, pp. 109–112. doi: 10.23919/EUMC.2010.5617161.

[50] F. Croq and D. M. Pozar, “Millimeter-wave design of wide-band aperture-coupled stacked microstrip antennas,” *IEEE Trans. Antennas Propag.*, vol. 39, no. 12, pp. 1770–1776, Dec. 1991, doi: 10.1109/8.121599.

[51] P. Brachat and J. M. Baracco, “Dual-polarization slot-coupled printed antennas fed by stripline,” *IEEE Trans. Antennas Propag.*, vol. 43, no. 7, pp. 738–742, Jul. 1995, doi: 10.1109/8.391150.

[52] “Soldering to Gold | | Indium Corporation Blogs | Indium Corporation.” https://www.indium.com/blog/soldering-to-gold-1.php (accessed Nov. 21, 2022).